Master of Science Thesis

Noise Prediction of a NACA 0015 Airfoil with Gurney Flap

A study based on Time-Resolved Particle Image Velocimetry

Xueqing Zhang

December 22, 2015

Aerodynamics

Faculty of Aerospace Engineering

TU Delft

Delft University of Technology

Noise Prediction of a NACA 0015 Airfoil with Gurney Flap

A study based on Time-Resolved Particle Image Velocimetry

Master of Science Thesis

For obtaining the degree of Master of Science in Aerospace Engineering at Delft University of Technology

Xueqing Zhang

December 22, 2015

Faculty of Aerospace Engineering · Delft University of Technology

Delft University of Technology

DELFT UNIVERSITY OF TECHNOLOGY
DEPARTMENT OF AERODYNAMICS

The undersigned hereby certify that they have read and recommend to the Faculty of Aerospace Engineering for acceptance the thesis entitled **"Noise Prediction of a NACA 0015 Airfoil with Gurney Flap"** by **Xueqing Zhang** in fulfillment of the requirements for the degree of **Master of Science**.

Dated: December 22, 2015

Supervisors:

Dr. ir. Andrea Sciacchitano

Prof. dr.-Ing. Fulvio Scarano

Dr. ir. Daniele Ragni

Dr. ir. Bas W. van Oudheusden

Preface

This thesis is dedicated to my family, whose unconditional love is never absent to back me up, and whose own sedulous pursuits of professional excellence always encourage me to move on. In memory of my grandfather, who set the paragon of a qualified aerospace engineer for me to follow. I am grateful to Teng Wang, for his help in digital signal processing and for every moment we have spent together.

Many gratitudes to Dr.Andrea Sciacchitano, for offering me the opportunity to work on aeroacoustics and for being an excellent mentor throughout the process. It has been an honour to work under his supervision. Si me lo permite, quisiera darle mis más sinceras felicitaciones y mis mejores deseos para esta nueva etapa en su vida, ¡un bébé!

Furthermore, I would like to thank Dr.Stefan Pröbsting, for the patient guidance and discussions in aeroacoustics, as well as for sharing the perceptions he harbours for this world that offered me a viewpoint I could otherwise ignore with my eastern cultural background. I would also like to thank all the technicians in the aerodynamics department for their friendly help and icecreams.

To all who shared this journey, thank you! Special mentions are due to Ilke and Zhenni, without whom my journey at TU Delft would never have begun; to Alberto, Ananth, Bo, Bowei, Jiale, Jiggar, Koen, Linfeng, Mudit, Remco, Shengling, Shruthi, Teng, Yifei, Ziyuan and many others with whom I had the pleasure of crossing our paths; to Xin Liao and Xing Meng, who are far away but always near.

Xueqing Zhang (Caddie)

张 雪晴

Delft, December 2015

People who design machines and airplanes, no matter how much they believe that what they do is good, the winds of time eventually turn them into tools of industrial civilization. They're cursed dreams. Beautiful yet cursed dreams.

— Hayao Miyazaki

"设计飞机和机械的人，无论他们的意图是多么善良，时代之风会把它转化为机械文明的工具，从来都不是无害的，都是被诅咒的梦想。"

— 宫崎 骏

Abstract

Air traffic noise, especially during the aircraft take-off and landing, has been universally acknowledged as a nuisance, for which reason, the International Civil Aviation Organization(ICAO) has ratified articles and established specifications aiming at the attenuation of air traffic noise, such as the Annex 16. The implementation of large bypass ratio turbo-fan engines on civil aircrafts and the application of designs such as engine nacelle and chevron nozzle have shifted the attention of noise control to the deployment of high-lift devices during take-off and landing. Source control is proved to be effective in the reduction of aeronautical noise. Traditional aeroacoustic assessments rely mainly on microphone (array) measurements and instantaneous flow fields obtained from CFD. However, the former fails in providing the mechanism of sound generation and the latter becomes prohibitive in the operating Reynolds number range of real aircrafts.

Previous investigations have validated the causality between the unsteady transverse velocity in the wake of the high-lift devices and the far-field pressure fluctuation. This thesis is a continuation of the previous study, focusing on investigating the feasibility of noise prediction of high-lift devices based on experimental data obtained by time-resolved PIV . A model of NACA 0015 airfoil with Gurney flap of the height of 6% the chord length has been investigated by means of 2D time-resolved PIV in combination with simultaneous microphone measurements. The Gurney flap is a simplified model of the high-lift devices with more complex structure in real application. The experimental parameters were selected such that the source of sound can be treated as compact and consequentially guaranteed the

applicability of both the distributed and the lumped formulation of the Curle's aeroacoustic analogy.

In the first step, the time evolving pressure field was deduced from the velocity field measured by 2D TR-PIV, by the Poisson-based solver for quasi-2D incompressible flows. Pressure on the surfaces of the airfoil then constitutes the source terms of the distributed formulation of Curle's analogy and the corresponding far-field noise was evaluated. In the second step, the aerodynamic loads of the airfoil were evaluated from the velocity field by means of momentum balance, which were then used in the lumped formulation for noise prediction. The spanwise coherence length evaluated from the cross-plane flow visualizations was applied for the correction of 3D effect.

Both formulations of the Curle's analogy yield noise evaluation of fair agreement with the simultaneous microphone measurements. All the calculated far-field noise power spectra reproduce the peak at Kármán vortex shedding frequency, which agrees well with the microphone measurements. The pressure fluctuations yielded by distributed formulation of the Curle's analogy are somehow damped due to the Gaussian smoothing applied to the velocity fields in the process of pressure reconstruction for the elimination of spurious spatial derivatives. Such damping effect can be circumvented by the lumped formulation, since the pressure is only evaluated on control volume boundaries in the locating in the far-wake, where 3D motions are weaker than in the region in direct proximity of the airfoil trailing edge. The high frequency components in the computed acoustic spectra are the most affected by the experimental and numerical errors. The coherence length correction reduce the over-estimation of the predicted noise levels with respect to the microphone measured ones. However, there still exists room for improvement in the procedure of coherence length correction.

Concludingly, this thesis proved TR-PIV an effective approach in the noise prediction of airfoil with Gurney flap and stepped out the first step in PIV-based aeroacousitic investigations of the high-lift devices. Application of the approach on high-lift devices with more complex configurations would be a prospective continuation of the current study.

Abstract (in Chinese)

基于时间解析粒子图像测速技术(PIV)的NACA0015翼型Gurney襟翼噪声预测

摘　要

航空噪声，尤其是在飞机起飞着陆阶段的近场噪声，随着民用飞机数量的剧增，日益引起世界范围的关注。为此，在国际民用航空组织（ICAO）制定了一系列飞机噪声适航条例，《国际民用航空公约》附件16便是其中之一。由于大涵道比涡扇发动机在民航客机中的广泛使用以及消声短舱、V-型花瓣喷嘴等结构上的改进大大地降低了发动机噪声，机体噪声飞机噪声中所占比例日益增大，其中飞机起降阶段增升装置噪声是机体噪声的重要组成部分。飞机降噪通常采用声源控制的方法主动降噪，此方法需要根据噪声产生机理改进增升装置结构，然而，传统的麦克风及阵列测量无法解释发声机理，而对于飞机设计雷诺数范围的瞬时流场计算目前仍是数值模拟无法企及的。

前人研究中已经证实了增升装置尾流中横向速度波动与远场压力扰动的因果关系。本文基于这一结论，对基于时间分辨PIV速度测量数据进行增升装置噪声预测的可行性进行了分析。本文使用Gurney襟翼作为增升装置的简化模型，对安装有高度为6%弦长的Gurney襟翼的NACA0015翼型同时进行二维PIV和远场麦克风测试。通过调整麦克风安装位置使得模型可以被看作致密声源，从而远场噪声既可以通过对机翼表面偶极子源进行积分直接求解（下称：分布式Curle声类比），也可以由速度场导出的气动载荷间接获得（下称：集总

式Curle声类比）。

本文首先运用针对准二维不可压流的泊松方程由二维PIV测量的速度场导出流场压力分布。进而由机翼表面压力波动通过分布式Curle声类比导出远场噪声。除此之外，本文还通过动量方程解出机翼在每个瞬时的气动载荷，并由此运用集总式Curle声类比求解远场噪声。本文通过将两种形式的声类比导出的远场压力扰动与麦克风测试结果对比，对两种情况的适用性进行了评估。此外，通过三维立体PIV在Gurney襟翼下游展向平面上的速度测量，可以导出展向相关长度，从而对二维PIV的噪声预测结果进行修正。

在导出的压力场中可以观察到压力极小值点与涡量场中涡核位置相对应。在实验过程中，可以清晰地听到音调噪音，且这一音调噪音所对应的频率峰值可以在所有由速度场导出的噪声频谱中观察到，而这一峰值频率恰好对应卡门涡街的漩涡脱落频率。两种形式的Curle声类比预测的远场噪声都与相应位置的麦克风测试有较好的吻合，所有由PIV预测出的噪声功率谱都再现了卡门旋涡脱落频率位置的峰值。为了避免流场测量误差对压力梯度带来的杂散，在求解压力场之前首先需要对PIV测得的速度场进行高斯平滑处理，而这一过程使得近场波动幅值衰减，从而导致分布式Curle声类比预测的远场压力扰动幅值下降。相比之下，由于导出气动载荷的控制体边界远离三维流动效应显著的区域，集总式Curle声类比求解过程中避免了平滑处理的过程。由本文中PIV导出的噪声频谱观察到，噪声中高于音调噪音频率的高频组分受试验及数值的影响较其他组分大。相关长度修正减少了基于二维的噪声预测与麦克风测试之间的偏差，但本文的校正过程仍有改进空间。

综上所述，本文验证了时间解析PIV在Gurney襟翼噪声预测上的可行性，迈出了基于PIV的增升装置噪声研究的第一步，此方法在增升装置的噪声预测中将具有可观的应用前景。

Table of Contents

List of Figures

List of Tables

Chapter 1

Introduction

Coughing, sputtering, roaring, plume of engine washing downwards and wings splitting the stream of the air, and there lifting off a Leviathan, these probably are what pop instantly into people's mind when talking about aviation. The cacophony played a symphony as it marked the opening of the golden era of aviation, and it continued to roar through the 20th century, casting enchantment that rouses awe towards the mighty metallic machine. Even nowadays, the throaty roar across the sky can still capture the attention like nothing else can. However, while the world is enjoying the amenity brought about by the proliferation of air traffic, the concomitant issues, such as the noise from the operation of aircraft, are not equally as romantic as the legend of aviation.

Early in the 1960s, the noise and disturbance caused by civil aviation has roused serious concern with the introduction of jet aircraft as a public transport and introduced heated social discussions. Based on the recommendations made in series of conferences, the International Civil Aviation Organization (ICAO) called for an international conference in Buenos Aires, September 1968, to consider the problem of aircraft noise in the vicinity of airports and sought to establish international specifications and guidance material relating to aircraft noise. The new standards regarding aircraft noise eventually became effective in 1971, which

is known as the first SARPS of Annex 16 - Aircraft Noise.[45] Contemporarily, articles on environmental impacts, noise emission included, were added to the airworthiness and certification process of aircraft by the Noise Control Act of 1972 and by a 1973 amendment to the Clean Air Act [7]. In deference of these regulations, designers and manufacturer of aviation industry nowadays are responsible for the environmental consequences of the aviation operations and are actively seeking for approaches of noise abatement. And thus, a fundamental understanding of the mechanism behind the emittance of aeronautical noise is critical for tackling the challenge.

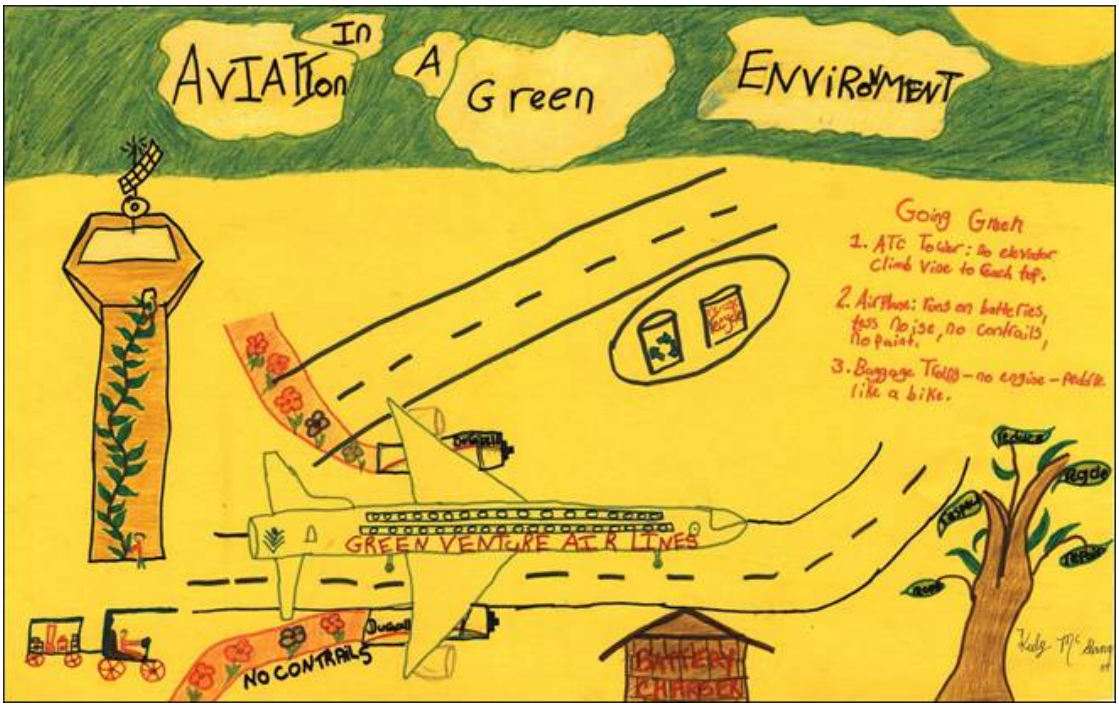

Figure 1.1: Drawing by Keely McGann, winning artist of the 2009 drawing contest organized by ICAO on the theme: Aviation in a Green Environment.

1.1 Noise and noise control

Noise is often referred to as unwanted sound, from the quiet but annoying sort such as the barking of dog, to the loud and harmful ones, such as jet engine in close quarter. The physics of the noise is the same as that of any other sound: in the case of fluid (gas, plasma or liquid), the sound source creates vibration that propagates longitudinally in the surrounding medium as sound waves. Sound waves are weak perturbations that cause the local pressure in the medium to deviate from the equilibrium one. This deviation is referred to as sound pressure, noted as p'.
Loudness, commonly used to refer the auditory sensation, is a subjective measure resulting from psychological factor and physical strength of the sound.[32] The physical strength of the sound is often measured by sound pressure level, which is a logarithmic measure of the sound pressure with respect to a reference value. Denoted by SPL and measured in decibel dB, the sound pressure level is defined as:

$$SPL = 20log_{10}\left(\frac{P}{P_0}\right) \tag{1.1}$$

where P is the root mean square of the local sound pressure, P_0 is the reference sound pressure. In air, $P_0 = 20\mu Pa$, which is the threshold of human hearing.[21] Figure 1.2 illustrates the decibel of a variety of sources, and the uneasiness and damage caused to human hearing.
In free space, the sound pressure of a spherical sound wave decreases with the inverse of the distance travelled, and thus the sound intensity decreases with the inverse square, known as the "inverse square law". The propagation of noise is also influenced by the convection of the medium, the obstacle presented on the path, and the absorption effect due to viscosity. Approaches of noise abatement therefore fall into two categories: acoustic insulation and source control. Since the efficacy of acoustic insulation, with the installation of sound absorbing materials, is relatively low and is often confined to small scale (such as room-acoustic), source control is more effective and practical in the case of aviation operations. The source control is fulfilled by adjusting the geometric or kinetic parameters such as to altering the noise generating flow features, and thus the understanding of the

mechanism of noise generation in specific flow fields is indispensable.

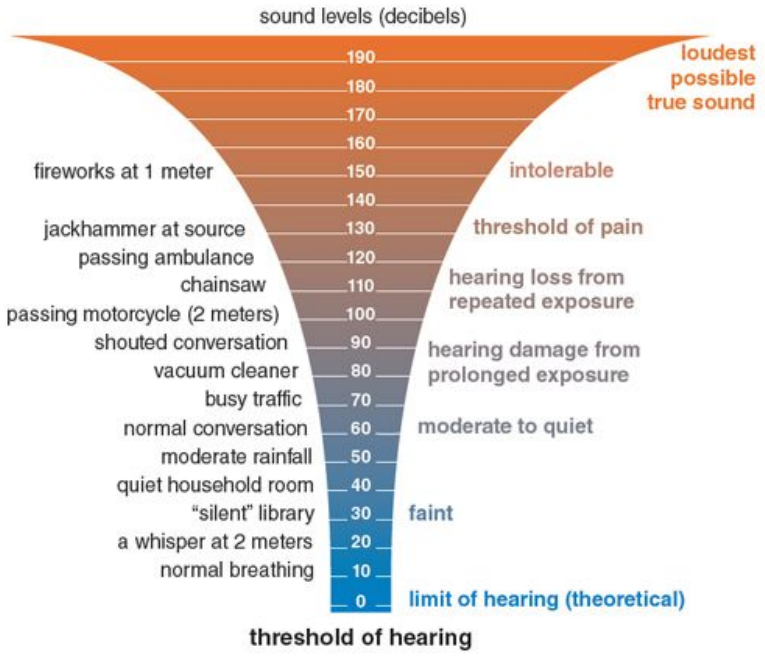

Figure 1.2: Decibel - Loudness Comparison Chart [46]

1.2 Aeronautical noise

Fixed-wing aircraft powered by jet engine is prototyped for airlines at the moment. Two major noise sources are identified for this configuration of aircraft: the jet engine and the airframe. Early generation of turbo-jets were major source of aeronautical noise, because of the increasing power generated for takeoff. The noise from the engine is positively related to exhaust velocity, the relation of which is described by the eighth power law (Lighthill,1952). With the development and implementation of the large by-pass ratio turbo-fan engines on the civil aircrafts, the exhaust velocity of the engine is lowered. Additional designs such as engine nacelles with acoustic liner and chevron nozzle further contribute to the engine

noise attenuation. Nowadays, the engine noise has been markedly reduced to the level comparable or even lower than the level of airframe noise. To reduce the overall noise level of the aircraft, attention should be shifted to the noise generated by airframe. The main noise generating airframe elements are:[62]

1. turbulent flow over a gap
2. flow past an airfoil with a flap
3. flow past an airfoil with a slat
4. flow past landing gear

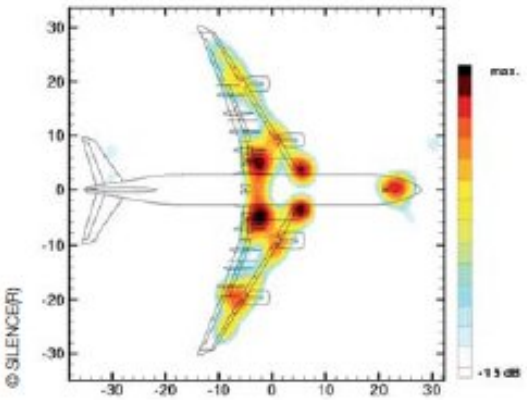

Figure 1.3: Example of AFN source localizations of a landing A340 with high-lift device and landing gears (from flight test campaign)[62]

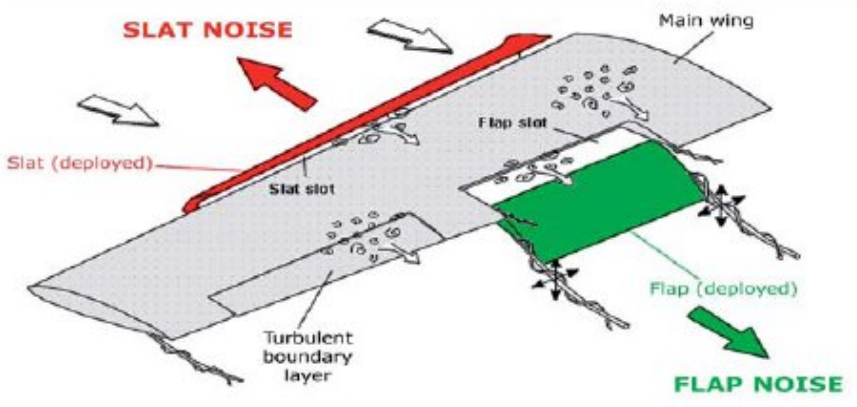

Figure 1.4: Source of noise on a typical wing[62]

1.3 Research objectives

Since the broadband noise generated by the deployment of high-lift devices (slat and flap) of the aircraft during takeoff and landing consists the main components of the airframe noise of aviation [58] and is universally considered as a nuisance especially to the residents in proximity to the airport, an effective way to attenuating the aeronautical noise is controlling the source of the sound, which requires an insight into the mechanism of sound generated by fluid flow, or aeroacoustics. According to the landmark paper in aeroacoustics in 1952 by M.J.Lighthill [41], the noise generation is attributed to the fluctuations in the unsteady fluid patterns.

Although there are already mature techniques in measuring the radiated sound, such as the microphone array measurement, the information about the source itself, such as the flow patterns and the pressure distribution in the source region, are still missing pieces of the puzzle and are beyond the reach of the traditional measurement techniques. With the development computers, lasers and cameras, particle image velocimetry (PIV) is capable in capturing the detail unsteady features in the flow field with high temporal and spatial resolution, and hence, can be a powerful tool in studying the source of sound.

This study aims at the development and validation of a technique which predicts the far-field noise based on the velocity field measured by the PIV system in the vicinity of the solid body immersed in the flow, based on the measurements acquired by time-resolved PIV and microphones. The outcome is a first step to the source control of the airframe noise.
A Gurney flap is a lift-enhancing device of simple configuration, typically with the shape of a small tab protruding perpendicularly into the flow. It was first implemented on race car by Daniel Gurney to enhance the turning capability and nowadays is utilized on wind turbines for lift increment [61]. In this preliminary design of the implementation of PIV in flap noise measurement, the Gurney flap serves as a simplified model of the flap on the aircraft, such as to facilitate the model manufacturing and experimental set-up.

Figure 1.5: Gurney flap on Rennspeed modified Porsche

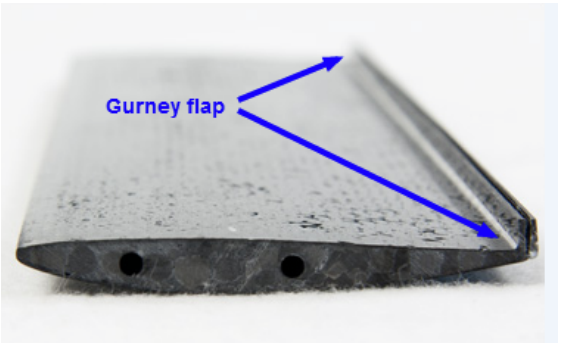

Figure 1.6: Gurney flap on F1 framework

1.4 Thesis Outline

Chapter 2 starts with an introduction of the Gurney flap aerodynamics and then gives an overview of the aeroacoustic analogies. In chapter 3, the mathematical tools applied in the data reduction procedure of this thesis work are introduced,

following which, the bridging techniques between the flow measurements and the application of acoustic analogies are presented. Chapter 4 continues with a description of the experimental techniques employed in the aerodynamic and aeroacoustic measurements in the course of the present study, before the detailed experimental set-ups are described in chapter 5. Results are presented in chapter 6 and the conclusions are reached in chapter 7.

Chapter 2

Gurney flap aerodynamics and aeroacoustics

Aerodynamics is a study of the motion of the air, particularly its interaction with the solid body submerged in the flow, which not only enables the calculation of forces or energy that can be harnessed, but also is essential in understanding the methodology behind the design and construction of airborne crafts and fluid machines.

Aeroacoustics studies the mechanism of noise generation aerodynamically, either by the turbulent motion (e.g. noise emitted by high speed air jet), or by the interaction of aerodynamic forces with the surfaces (e.g. 'singing' telephone wires). Although the scientific theory of the noise generation by aerodynamic flows has not been fully established, yet practical analysis that relates the hydrodynamic flow phenomena and the wave-like propagating disturbances has been investigated extensively for various flow conditions.

This chapter first gives an overview of the flow features and lift-enhancing mechanism of the Gurney flap in section 2.1. Thereafter, a general introduction to aeroacoustic analogies is given in section 2.2 followed by detailed information on Lighthill's analogy and Curle's analogy.

2.1 Gurney flap aerodynamics

Since the first implementation on the race car by Daniel Gurney in the 1970s, the flow properties of the Gurney flap are widely investigated in literatures. Lieback(1978) [40] was the pioneer of investigating the aerodynamic performance by experiments. His experiments on a Newman airfoil with 1.25% the chord length proved the Gurney flap to be lift-enhancing. At the same time, though counter-intuitive, the Gurney flap was found to be drag-reducing. Lieback further suggested the height of the Gurney flap should be kept between 1% to 2% of the chord length to optimize the aerodynamic benefits, while the flaps with height exceeding 2% chord length will substantially increase the drag. A more detailed study on the scaling of Gurney flap by Giguère concludes that the Gurney flap height should be less than the local boundary layer thickness to avoid the increase in drag.[52]
The efficacy of Gurney flap in improving the lift characteristics of airfoils, wings and aircraft models has been confirmed with the measurements from various studies, such as [48], [33] and [39]. Pressure and velocity measurements have helped shedding light on the mechanism responsible for the lift-enhancement. However, compared to the widely observed improvements in aerodynamic performance, the mechanism is not equally unveiled. Pressure and velocity measurements have helped shedding light on the issue. Jeffrey et al. (2000) [33] attributed the lift-enhancement for subsonic airfoils to two major causes:

1. The Gurney flap decelerates the flow upstream, and consequently the pressure difference of the lower surface and upper surface of the airfoil is increased at the trailing edge. In such a way, Gurney flap adds to the effective camber of the airfoil.

2. The long wake downstream the Gurney flap increases the trailing edge suction and thus delays the flow separation on the upper surface of the airfoil.

Either cause leads to the increase in airfoil circulation, which results in the increase in lift. Notably, Jeffrey et al. suggested in the same article that the flow structure

in the wake downstream the Gurney flap contains a pair of counter-rotating vortices, which is first observed by Lieback(1978) [40].

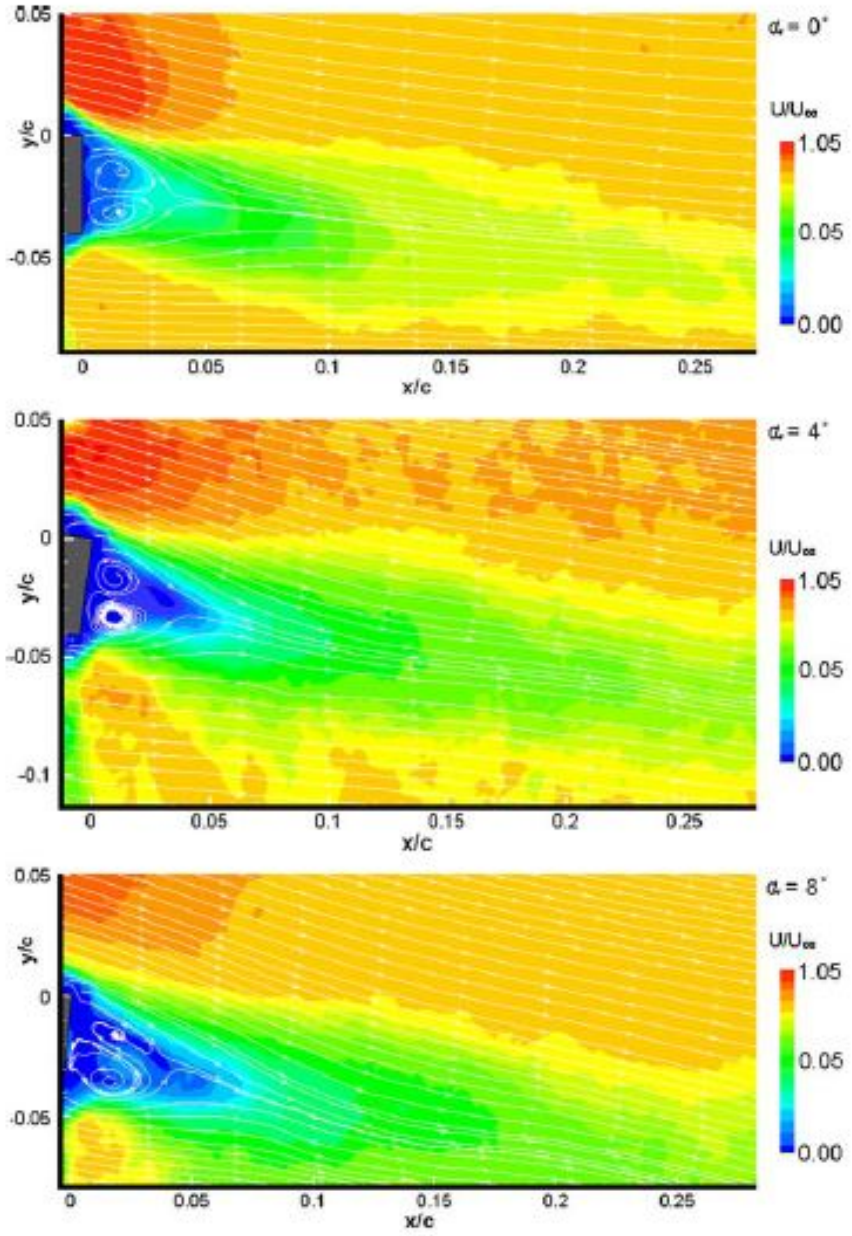

Figure 2.1: Visualization of counter-rotating vortices downstream the trailing edge for 4% Gurney flap with $\alpha = 0°$,$4°$ and $8°$ [64]

The development of time-resolved PIV (TRPIV) facilitates the detailed investigation of flow patterns. Troolin et al. (2006) [64] examined the evolving flow patterns downstream a NACA 0015 airfoil with Gurney flap with TRPIV, which also reported the counter-rotating vortices. In this article, they further proposed the existence of two distinct vortex shedding modes.

1. Dominant mode: this mode resembles the Kármán vortex shedding.
2. Second mode: this mode is the result of the intermittent ejection of the circulating fluid in the cavity formed by the Gurney flap and the airfoil.

According to Troolin et al., the second shedding mode induces negative normal velocity in the wake of the airfoil and thus contributes to the increase in circulation. However, the observation of the second shedding mode has, curiously, not been reported by other researchers until the writing of this thesis.
For further information and detailed theories about Gurney flap, one can refer to [69], which is a compendium summarizing the aerodynamic characteristics, lift-enhancing mechanism, and optimum design of Gurney flap, as well as the application of Gurney flap on airfoils, wings and aircraft models ranging from subsonic to supersonic.

2.2 Aeroacoustic analogies

Aeroacoustic analogies describe the dependence of the flow generated sound field and its causes, the fluctuations in the flow. The notion of aeroacoustic analogy (also mentioned as 'acoustic analogy') was first introduced by Sir James Lighthill in 1952, with his 'On sound generated aerodynamically' [41], which placed the noise from jet engine under the scientific scrutiny and later is acknowledged as the origin of modern aeroacoustics. [38]
In several decades, aeroacoustic analogy has burgeoned into a big family. Despite the difference in the choice of field variables, the way of interpreting source terms

and the mathematical complexity of numerical application, the analogies can be rearranged in the general form of Equation 2.1.

$$Lf = g \tag{2.1}$$

In the general form, f is the field variable used by the analogy, such as density, velocity or enthalpy. L is the wave operator that relates the field variables in such a way that the fluctuation of these variables propagates like waves. g is the source term that has to be defined *a priori*, or the equation of aeroacoustic analogy should be solved iteratively to increase the accuracy of the source term. In most cases, instead of using the true acoustic source distributions, the source term is defined by collecting from the field variable terms left over by the wave operator on the left hand side.
The aeroacoustic analogies can be sorted into three categories based on the field variables applied. The complexity of the application of the following analogies grows in the order they are presented below.[65]

1. Density-based analogies
    - Lighthill's analogy
    - Curle's analogy
    - Powell's analogy
    - The Ffowcs Williams-Hawkings analogy
2. Phi-based analogies (convected wave equation analogies)
    - Phillip's analogy
    - Lilley's analogy
3. Enthalpy-based analogies
    - Howe's analogy

- Doak's analogy

Trailing edge noise is an important topic in aeroacoustics, where sound is produced by the interaction of unsteady flow with a sharp-edged body such as a flap. The first investigation of trailing edge noise at low Mach flow was performed by Powell in 1959 on a rigid flat plate moving at zero incidence [53], following which various studies and theories were published. These theories are summarized in [30]and are roughly categorized according to the assumptions made of the way in which the fluctuating flow interacts with the sharp edge to produce sound. The theories roughly fall into two categories:

1. Theories based on Lighthill's analogy
2. Theories designed for particular model or relating the sound field to the pressure distribution model on or near the edge of the plate

Gurney flap noise is a type of trailing edge noise and falls into the realm of the first category, where the far-field radiations determined in terms of the turbulent velocity field. Examples of the theories in this category are developed by Ffowcs Williams and Hall[74], Crighton and Leppington[8] and Howe [29].
Since the present work is a first step towards the prediction of trailing edge noise of the airfoil with Gurney flap, the Curle's analogy, a special (and simpler) case of Ffowcs Williams-Hawkings analogy, is chosen to educe the far-field noise from the PIV measured velocity field for the simplicity of numerical application. Therefore for the reason of brevity, only the physical background and working equations of the Lighthill's and Curles analogy are presented. Note that the Lighthill's analogy is the antecedent of Curle's analogy. For information of other acoustic analogies and for detailed mathematical derivations, one can refer to[41], [9], [17], [27], [28] and [65].
Since both Lighthill's analogy and Curle's analogy are density-based aeroacoustic analogy, the field variable f in Equation 2.1 is substituted with ρ', the fluctuation of the density ρ. In the case of current project, it is equivalent to choose the pressure perturbation (sound pressure) p' as field variable. The argument goes as

follows.
Apart from the problems where energy is transferred by heat conduction, such as frictional dissipation of sound, highly non-linear events caused by the shock waves or sound generation by heat sources(e.g. combustion), it is sufficient to consider the flow to be homentropic.[28] Namely, the entropy s of the fluid is uniform and constant, and thus the energy equation can be substituted by:

$$s = s_0 = constant \tag{2.2}$$

For perfect gas, the speed of sound is determined by:

$$c_0 = \sqrt{\frac{\partial p}{\partial \rho}_{|_{s=s_0}}} = \sqrt{\gamma RT} \tag{2.3}$$

where R is the gas constant, $\gamma = C_p/C_v$ is the specific heats ratio and T is the absolute temperature in K.
Under the homentropic condition, local pressure and density obey the Poisson relation: $p \propto \rho^\gamma$. Combined with Equation 2.3, results in a linear relation between small fluctuation in density and pressure:

$$p' = c_0^2 \rho' \tag{2.4}$$

In the following sections, both ρ' and p' are used as field variable.

2.3 Lighthill's analogy

Lighthill's analogy establishes an analogous relation between the acoustic radiation from relatively small regions of turbulent flow embedded in an infinite homogeneous fluid, and the sound produced and propagating in an ideal , stationary medium driven by a stress distribution. This relation is described with a non-homogeneous wave equation, known as the *Lighthill's equation*. The stress distribution serves as the source term of the non-homogeneous wave equation, denoted as T_{ij}, namely, the *Lighthill's stress tensor*.

Derivation of Lighthill's equation

The Lighthill's equation is retrieved from the rearrangement of Navier-Stokes equation. The mass and momentum conservation of a compressible flow described by Navier-Stokes equations in summation convention read:

$$\frac{\partial \rho}{\partial t} + \frac{\partial \rho v_i}{\partial x_i} = 0, \tag{2.5}$$

$$\rho \frac{\partial v_i}{\partial t} + \rho v_j \frac{\partial v_i}{\partial x_j} = -\frac{\partial (p\delta_{ij} - \sigma_{ij})}{\partial x_j} \tag{2.6}$$

where σ_{ij} is the (i, j)th component of the viscous stress tensor. For a Stokesian gas, it is defined by the constitutive equation reads:

$$\sigma_{ij} = \mu \left(\frac{\partial v_i}{\partial x_j} + \frac{\partial v_j}{\partial x_i} - \frac{2}{3}\delta_{ij} \frac{\partial v_k}{\partial x_k} \right) \tag{2.7}$$

where μ is the viscosity of the fluid. Multiplying Equation 2.5, adding the result to Equation 2.6, the result of which upon adding and subtracting $c_0^2 \partial \rho / \partial x_i$, yields:

$$\frac{\partial \rho v_i}{\partial t} + c_0^2 \frac{\partial \rho}{\partial x_i} = -\frac{\partial T_{ij}}{\partial x_i} \tag{2.8}$$

where

$$T_{ij} = \rho v_i v_j + \delta_{ij}[(p - p_0) - c_0^2(\rho - \rho_0)] - \sigma_{ij} \tag{2.9}$$

is the Lighthill's stress tensor. Differentiate Equation 2.5 with respect to t, take the divergence of Equation 2.8, and then subtract the results to obtain the Lighthill's equation:

$$\left(\frac{\partial^2}{\partial t^2} - c_0^2 \nabla^2 \right) \rho' = \frac{\partial^2 T_{ij}}{\partial x_i \partial x_j} \tag{2.10}$$

The subscripts "0" used in p_0 and ρ_0 in Equation 2.9 denotes the constant reference value, which is taken the value of corresponding property at large distances from the sound generating turbulent region. The reason for this arrangement

is that, at the distance sufficiently far away from the turbulent region, the flow recovered to be homogeneous, with uniform equilibrium state: speed of sound c_0, density ρ_0 and pressure p_0.

Approximation of Lighthill's stress tensor

A first step towards solving the Lighthill's equation is determining the value of T_{ij}. However, the pressure fluctuation term in T_{ij} cannot be determined until Equation 2.10 is solved, which is equivalent of solving the Navier-Stokes equations governing the flow problem and is virtually impossible. Therefore approximation should be made according to the flow condition under investigation.

Fortunately, many cases of aeronautical interest are of high Reynolds number, which renders the contribution of viscous term σ_{ij} negligible when compared to the Reynolds stress term $\rho v_i v_j$. In addition, as stated beforehand, when heat transfer is negligible in the flow, the flow field can be considered homentropic, resulting in the elimination of $\delta_{ij}[(p - p_0) - c_0^2(\rho - \rho_0)]$.

At large distance from the turbulent region, density fluctuation should behave in the way of acoustic wave and obeys d'Alembert equation:

$$\left(\frac{\partial^2}{\partial t^2} - c_0^2 \nabla^2\right) \rho' = 0 \tag{2.11}$$

which indicates $\rho v_i v_j$ equals zero in the far-field. Furthermore, when Mach number is sufficiently low, the pressure variations in the vicinity of a localized flow are substantially uninfluenced by the compressibility, and hence $\rho = \rho_0$ can be approximated inside the flow.

At fairly low Mach number, there exists an intermediate region between the localized flow and the sound field. The treatment can be the same as in the localized flow, according to the argument given by Goldstein (1976)[17]:

...the pressure fluctuations have some of the properties of both the localized fluctuations and those in the sound field. Thus, in this region, the pressures are as weak as in the sound field, but the distances involved are small enough so that the effects of finite propagation speed, and hence of compressibility, can be neglected.

Consequently, the Lighthill's stress tensor can be approximated as:

$$T_{ij} \approx \rho_0 v_i v_j \tag{2.12}$$

Solution to Lighthill's equation for unbounded flow

When no solid boundaries are present, or the presence of the solid boundaries does not influence the sound field to an appreciable extent, the solution to Equation 2.10 is the summation of the influence of sources in the dimensions of space and time. By solving the corresponding equation expressed with Green's function G, the solution of which is the influence of a certain source at a given location and time instant.

$$\left(\frac{\partial^2}{\partial t^2} - c_0^2 \nabla^2\right) G = \delta(\mathbf{x} - \mathbf{y})\delta(t - \tau) \tag{2.13}$$

The solution to Equation 2.13 is the standard 3D Green's function:

$$G(\mathbf{x}, \mathbf{y}, t, \tau) = \frac{\delta(t - \tau - \frac{r}{c_0})}{4\pi r} \tag{2.14}$$

where $r = |\mathbf{x} - \mathbf{y}|$. Equation 2.14 indicates the influence exerted by an elementary source, positioned at $\mathbf{y}$ and at time τ on the listener, positioned at $\mathbf{x}$ and at time t. Detailed execution of the mathematical procedures in solving such PDEs by means of Green's function can be found in reference[19]. The general solution given by Lighthill to Equation 2.10 results in:

$$\rho'(\mathbf{x}, t) = \frac{1}{4\pi c_0^2} \frac{\partial^2}{\partial x_i \partial x_j} \int_{V_y} T_{ij} \left(\mathbf{y}, t - \frac{r}{c_0}\right) \frac{dV}{r} \tag{2.15}$$

With the approximations on Lighthill's stress tensor (Equation 2.12), and the relation between fluctuation in pressure and density (Equation 2.4), the solution reduces to:

$$p'(\mathbf{x}, t) = \frac{1}{4\pi} \frac{\partial^2}{\partial x_i \partial x_j} \int_{V_y} \rho_0 v_i v_j \left(\mathbf{y}, t - \frac{r}{c_0}\right) \frac{dV}{r} \tag{2.16}$$

Discussion

Lighthill's equation treats the sound sources convecting with the same speed of the flow in a way as if they were moving in the stationary medium. It incorporates

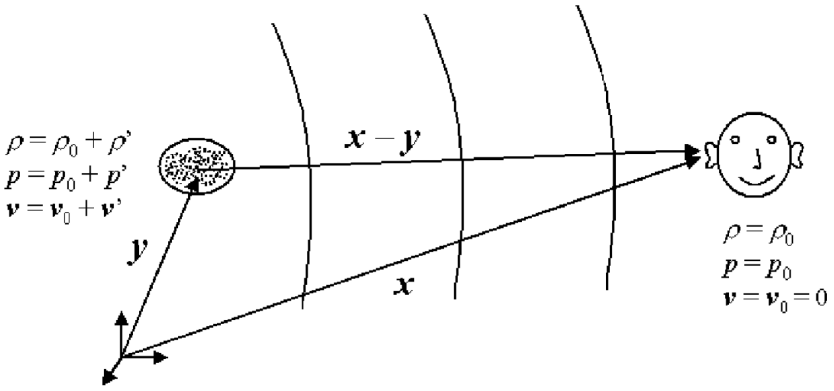

Figure 2.2: Source-listener locations standard 3D Green's function [27]

the sound generation, convection with the flow, propagation with different speed, and dissipation due to conduction and viscosity.
Under the flow conditions:

1. there are no mass, heat, force or momentum source distributions

2. the perturbation of sound propagation on the hydrodynamic parameters is small enough to be neglected

3. the spatial gradients of the speed of sound and the static hydrodynamic parameters are, at most, of the order of the perturbation

Lighthill's equation is an exact consequence of mass and momentum conservation. Approximations are only introduced after the derivation of the Lighthill's equation to make the solution plausible. The solution given by Lighthill (Equation 2.15) is applicable when no solid boundary present in the flow or the influence of solid boundary is negligible, such as subsonic cold air jet. The solution displays a quadrupole structure of the sound source, which is relatively inefficient in sound radiation, as discussed in the next section.

2.4 Curle's analogy

The solution given to Equation 2.10 by Lighthill is for unbounded flow, which does not include the influence of solid boundaries submerged in the flow, although at the time Lighthill has remarked on the importance of solid boundary in the generation of sound. In fact, in many cases of technological interest, solid boundaries play a vital role in sound generation, such as high-lift devices, propellers, helicopters, windmills and turbofans.
The presence of solid boundaries in the flow influence the sound radiation in two ways, the mechanisms of which lie respectively in theories of classical acoustics and aeroacoustics:

- The solid boundaries reflect and diffract the sound generated by the volume quadrupole sources that appear in Lighthill's solution.

- The solid boundaries support the distribution of dipole sources; in the case where the solid boundaries are in motion, monopole sources can be generated.

The limitation was overcome by N. Curle in 1955 [9]. The solution given to the Lighthill's equation by Curle takes the effect of solid boundaries into account and is later known as the Curle's equation.

Solution to Lighthill's equation with effect of solid boundaries

The classical formulation of Curle's equation is for solid boundaries which are rigid, fixed and non-permeable, and thus the interaction between fluid and structure does not involve deformation and displacement.
Integrating Equation 2.10 by means of 3D Green's function Equation 2.14, the difference between the solution given by Curle and that by Lighthill lies in the boundary condition. The general solution in the presence of solid boundaries

writes:

$$p'(\mathbf{x},t) = \int_{-\infty}^{t+}\int_{V_y}\frac{\partial^2 G}{\partial y_i \partial y_j}T_{ij}dVd\tau + \int_{-\infty}^{t+}\int_{\partial V_y}\left(\frac{\partial T_{ij}}{\partial y_j}G - T_{ij}\frac{\partial G}{\partial y_j}\right)n_i dSd\tau \\ -c_0^2\int_{-\infty}^{t+}\int_{\partial V_y}\left(\rho'\frac{\partial G}{\partial y_i} - G\frac{\partial \rho'}{\partial y_i}\right)n_i dSd\tau \tag{2.17}$$

When the surface of the solid body is rigid and stationary, the solution of far-field pressure can be written as:

$$p'(\mathbf{x},t) = \frac{1}{4\pi}\frac{\partial^2}{\partial x_i \partial x_j}\int_{V_y}\left.\frac{T_{ij}}{r}\right|_{t=t_e}dV - \frac{1}{4\pi}\frac{\partial}{\partial x_j}\int_{\delta V_y}\left.\frac{P_{ij}}{r}\right|_{t=t_e}n_i dS \tag{2.18}$$

where $P_{ij} = p'\delta_{ij} - \sigma_{ij}$ is the generalized pressure tensor formed by the combination of pressure fluctuation and viscous stress. t_e is the retarded time.

The volume integral and surface integral of Equation 2.18 (respectively the first and second term on the right hand side) are often referred to as quadrupolar and dipolar source terms.

It can be noted that the presence of solid boundaries engenders a dipole source. This phenomenon is caused by the prevention of pressure recovery by fluid acceleration due to the solid boundaries. The flow in turn exerts a fluctuating force on the solid body, in the form of time-varying surface pressure. The fluctuating force is directly related to a dipole acoustic source and causes a higher level of noise emission compared to the free turbulence.

Figure 2.3 shows the radiation patterns of monopole, dipole and quadrupole sources. It can be seen that the monopole source is the most efficient for low Mach number and is omnidirectional, while the emission of dipole and quadrupole is directional due to mutual cancellation. Take dipole as an example: a dipole is a separation of a sink and a source. The line connecting the two coupled source in dipole is called the axis of dipole. Along the axis, the direction of the dipole is defined as pointing from sink to source. The positions on the line perpendicular

to the axis of dipole do not perceive any disturbance from the source.

As mentioned previously the fluctuating of aerodynamic force is directly related to the dipole source. It can be further argued that, the strength and direction of a dipole source is equivalent to the strength and direction of the force exerted by the solid body on the external fluid. [75] It can be thus concluded that for an airfoil, the strongest noise emission can be expected on the direction perpendicular to the chord.

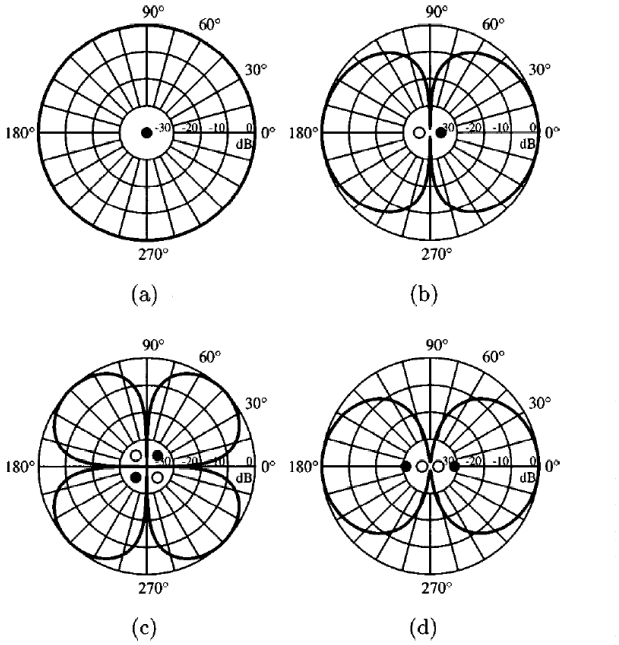

Figure 2.3: Theoretical directivity patterns for far-field sound pressure levels radiated from (a) monopole, (b) dipole, (c) lateral quadrupole, and (d) longitudinal quadrupole sound sources. [59]

Curle's analogy under compact-body assumption

Simplifications can be made under certain flow conditions, and with the introduction of compactness. When the characteristic dimension of the solid body L (for airfoil, it can be chord length)is much smaller compared to the emitted acoustic wavelength λ, the noise source is said to be acoustically compact. Since under this condition, the acoustic wave propagates much faster than the flow car-

rying the sound generating vortices. The compact relation can be written as: $L/\lambda << M << 1$, which indicates that at low Mach number, the flow induced sound source are more likely to be compact.

For low Mach number ($M < 0.05$), the compressibility effect of the flow can be neglected. Furthermore, for chord Reynolds number (10^5), though the viscosity plays an important role in the near wall region, the overall effect can still be neglected when compared to the normal stresses. Then, the contribution of viscous term σ_{ij} in the dipolar source can also be neglected [70].In addition, under such circumstances, the magnitude of the quadrupolar source is M^2 order lower than the dipolar term and therefore can be neglected [17]. Thus the solution of far-field pressure fluctuation reduces to:

$$p'(\mathbf{x},t) = -\frac{x_j}{4\pi c_0|\mathbf{x}|}\frac{\partial}{\partial t}\int_{\delta V_y}\left.\frac{p'\delta_{ij}}{r}\right|_{t=t_e} n_i dS \tag{2.19}$$

With the assumption of compact body, it is possible to further assume a uniform retarded time $t_e = t - R/c_0$ on the integral surface, and Equation 2.19 can be further simplified with the surface integral of pressure substituted by the instantaneous aerodynamic forces exerted on the airfoil section:

$$p'(\mathbf{x},t) = -\frac{R_j}{4\pi c_0 R^2}\frac{\partial F_j(t_e)}{\partial t} \tag{2.20}$$

Equation 2.20 is known as the Gutin's principle for compact and rigid body [54], where R_j is the j^{th} component of the position vector originating from the airfoil leading edge pointing to the listener and F_j is the aerodynamic force.

Discussion

Curle's analogy is the solution to the Ligthhill's equation Equation 2.10 when the effect of rigid, stationary solid boundaries is taken into consideration. The presence of solid boundaries engenders a dipolar source term in the solution, which radiates sound more efficiently than the quadrupolar source introduced by free turbulence. Especially, at low Mach number, the contribution of quadrupolar source can be neglected at the presence of dipolar source.

When the source satisfies the condition of compactness, with the application of

Gutin's principle, the term of the integral of surface pressure in the dipolar source term can be substituted by the instantaneous aerodynamic forces. Since there are ready techniques for evaluating or measuring fluctuating aerodynamic loads, the simplification of Curle's analogy not only facilitates the numerical application, but also lowers the demand for experimental set-up.

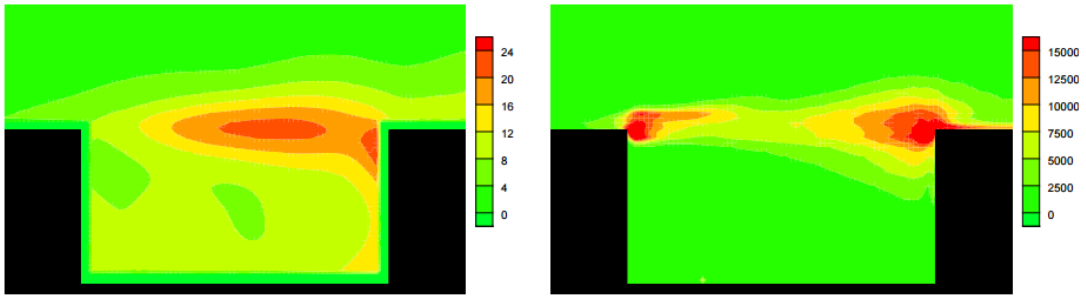

(a) Pressure[Pa] rms (b) $(\omega \times \mathbf{u}) \cdot \nabla \mathbf{Y_1}$[m/s^2] rms

Figure 2.4: Root mean square of the source terms retrieved from PIV measurements of a 2D cavity by Koschatzky et al. (2010)[36]

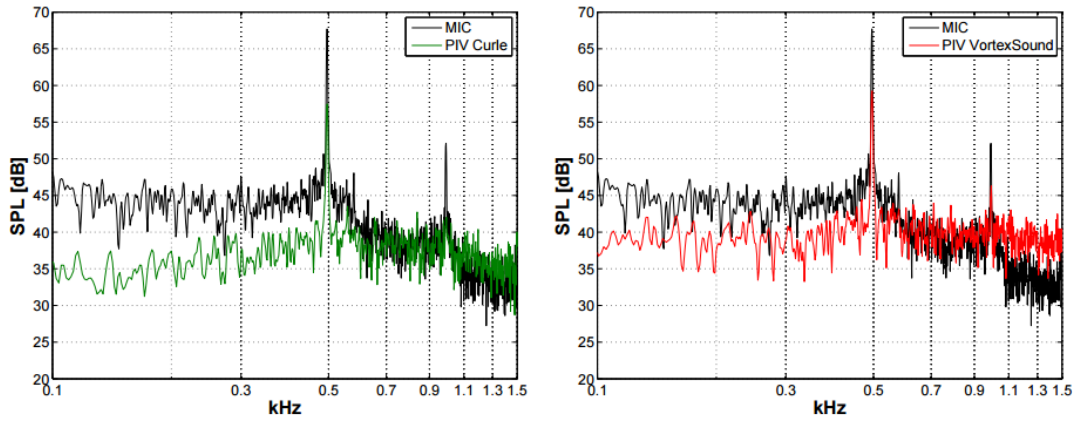

(a) Curle (b) Vortex sound

Figure 2.5: Power spectra of sound signal from a microphone and of sound computed from PIV at the same locations with the Curle's analogy and the vortex sound theory by Koschatzky et al. (2010)[36]

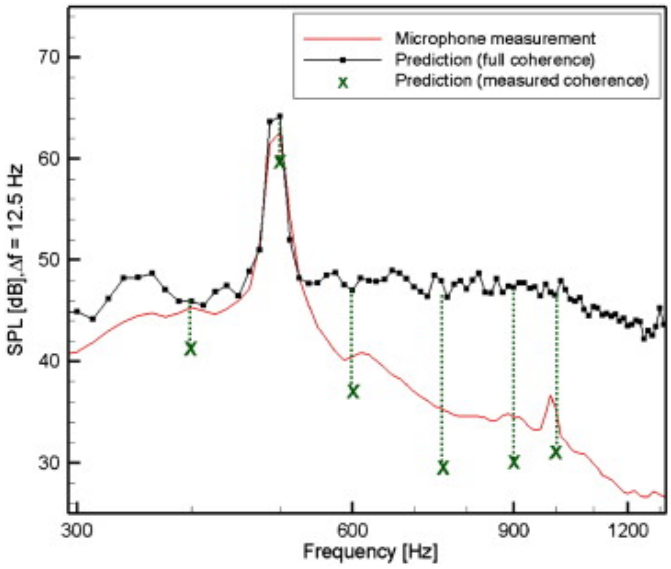

Figure 2.6: Power spectra computed using Curle's analogy with the microphone measurement. Predictions based on full span coherence assumption and on the measured spanwise coherence length by Lorenzoni et al.(2012) [43]

Aeroacoustic predictions with Curle's analogy based on PIV measurements have already been carried out successfully. Haigermoser (2009) [20] derives the acoustic emission of a cavity flow using planar TRPIV measurements in a water tunnel. Koschatzky et al. (2010) [36] applied Curle's analogy and vortex sound theory to the PIV measured velocity field of an open, two-dimensional shallow cavity, where Curle's analogy is superior in predicting broad band noise and inferior in tonal and harmonic component. Lorenzoni et al. (2012) [43] investigates the acoustic emission from vortex-structure interaction with the TRPIV measurements on a rod-airfoil configuration, where the Curle's analogy is applied in both distributed (Equation 2.19) and lumped (Equation 2.20) formulation to acquire the far-field noise.

Chapter 3

Data reduction techniques

The following sections offer a general introduction on the techniques for analysing the experimental data. First, the mathematical background of statistical data analysis methods are introduced, including the causality-correlation, the spectral density calculation and the variance and covariance. Then, the techniques for evaluation of pressure field and aerodynamic loads are presented, which are the bridging techniques between the PIV measured velocity and the application of Curle's analogy.

3.1 Statistical data analysis

This section gives a brief introduction to the data analysis techniques applied in the current study for analysing the relationship between near-/far-field.

3.1.1 Causality-correlation

Cross-correlation is a standard method that detects the relationship between assumed excitation and observed response. The cross-correlation coefficient measures the existence of such interrelationship and their relative strength, which is calculated by [23]:

$$R_{\psi,p}(\mathbf{x},\tau) = \frac{C_{\psi,p}(\mathbf{x},\tau)}{\sigma_\psi(\mathbf{x})\sigma_p} = \frac{\langle \psi'(\mathbf{x},t)p'(t+\tau)\rangle}{\sqrt{\langle \psi'(\mathbf{x},t)^2\rangle \langle p'(t)^2\rangle}} \tag{3.1}$$

where $\psi'(\mathbf{x},t)$ is the zero-mean part of the near-field quantity, such as velocity fluctuation u' and v', measured at position $\mathbf{x}$ and time t; p' represents the acoustic pressure measured in the far-field; τ is the time shift between between the far-field pressure and near-field quantity.

The cross-correlation is similar to the covariance of two functions except for the terms in denominator, $\sigma_\psi(\mathbf{x})$ and σ_p, which are root-mean-square (RMS) of the near and far field variables. The normalization with the RMS results in bounding the value of cross-correlation coefficient $R_{\psi,p}(\mathbf{x},\tau)$ within $[-1,1]$. The bounding value 1 or -1 is taken when the near and far field signals display a perfect linear relationship. Non-linear relationship or data scattering due to measurement noise will force the value $R_{\psi,p}$ to zero.

It should be noted that correlation does not necessarily imply causality, while the latter should be validated by other proof. In the current study of far-field noise generated by an airfoil with Gurney flap, the proof of causality relation is the Curle's analogy described by Equation 2.18. Although Equation 3.1 is given in a time domain, yet it is equivalent to the spatial correlation between near and far field variables in this study, since the retarded time and the spatial distance are related with a constant speed of sound.

Since the experimental data is acquired at discrete time instants t_n, Equation 3.1 should be applied in discrete form:

$$C_{\psi,p}(\mathbf{x},\tau) = \frac{1}{N}\sum_{n=1}^{N}[\psi'(\mathbf{x},t_n)p'(t_n+\tau)] \tag{3.2}$$

with

$$\sigma_\psi(\mathbf{x}) = \sqrt{\frac{1}{N}\sum_{n=1}^{N}\psi'^2(\mathbf{x}, t_n)} \tag{3.3}$$

Series of synchronized PIV and microphone measurements of cylinder wake [22], rod-airfoil configuration [23], cold jet [24] and high-lift device [25] have proved the validity of the causality correlation method in identifying the flow structure responsible for noise generation. Though Henning et al. (2014) [26] proposed the ambiguity of noise source localization with the correlation technique, the relation between near-/far-field is not vitiated.

Caution should be taken when investigating the non-linear system with cross-correlation. In certain cases, signals strongly related by non-linear dynamics can be blinded by cross-correlation coefficient suggesting little correlation due to the zero quadratic moments. The phenomenon is beyond the scope of discussion of the current study. More information about the correlation in non-linear system can be found in [4].

3.1.2 Spectral density

Any signal that can be described as an amplitude varying in time represents a certain physical phenomenon. When these signals are projected onto the frequency domain and are represented in the form of power spectra, often, the underlying properties, such as harmonics, become more evident and thus provide insight into the mechanisms that generate the signal. The power spectrum describes the power distribution over the different frequencies. When the signal is from measurement of turbulent velocity field, the study of power spectrum facilitates revealing the periodicity and dominating time-scale of the vortex structures, and hence the revelation of the mechanism of phenomena related to the vortices.

The spectral density can be defined in three equivalent ways [3]:

1. via correlation functions,
2. via finite Fourier transforms,
3. via filtering-squaring-averaging operations.

The discussion in this section will focus on the first two approaches.
Assume the input and output signal are mono-dimensional continuous time signals $x(\tau)$ and $y(\tau)$, then the general formulation of cross-correlation function is written as:

$$R_{xy}(\tau) = \lim_{T\to\infty} \frac{1}{T} \int_{-\frac{T}{2}}^{\frac{T}{2}} x(t)y(t+\tau)dt \tag{3.4}$$

when $x(\tau) = y(\tau)$, $R_{xy}(\tau)$ becomes the auto-correlation function $R_{xx}(\tau)$ (or $R_{yy}(\tau)$).
The Fourier transform of the correlation function yields the *Power Spectral Density*:

$$S_{xy}(f) = \int R_{xy}(\tau)e^{-2i\pi f\tau}d\tau \tag{3.5}$$

where $S_{xy}(f)$ is the two-sided cross-spectral density function and is an even function of frequency f. Here, the value of f can be both positive and negative. Since the negative frequency and the positive frequency is equivalent, one-sided cross-spectral density can be defined for $f \geq 0$ as:

$$\Phi_{xy}(f) = \begin{cases} 2S_{xy}(f) & f > 0 \\ S_{xy}(f) & f = 0 \end{cases} \tag{3.6}$$

The auto-spectral density Φ_{xx} (or Φ_{yy}) can be defined similarly. Equation 3.5 is often referred to as the Wiener-Khinchine relations in honour of the two mathematicians N. Wiener and A. I. Khinchine.
Alternatively, the spectral density can be derived based on finite Fourier transform, which is better for engineering application since the measurements in real world can only be acquired in finite time interval $0 \leq t \leq T$. The cross-spectral density is defined as:

$$S_{xy}(f,T,k) = \frac{1}{T}X_k^*(f,T)Y_k(f,T) \tag{3.7}$$

where $X_k(f,T)$, $Y_k(f,T)$ are the Fourier transforms of the sample records $x_k(t)$, $y_k(t)$, with $X_k^*(f,T)$ the complex conjugate of $X_k(f,T)$.
To extrapolate $S_{xy}(f,T,k)$ to the infinite time range, expected value of $S_{xy}(f,T,k)$ should be used for statistical consistency:

$$S_{xy}(f) = \lim_{T\to\infty} E[S_{xy}(f,T,k)] \tag{3.8}$$

The definition given by Equation 3.7 and Equation 3.8 is often referred to as the Welch's method, named after P. D. Welch.

3.1.3 Coherence

Coherence, similar to cross-correlation, evaluates how well the two signals are related, except that cross-correlation evaluates the phase lag of the two signals in the time domain, while coherence evaluates the dependency of the average phase angle for each frequency components of the two signals.
The coherence function is defined based on the cross-spectral and auto-spectral density function, which can be used to examine the relation between two signals, such as the investigation of the power transfer between input and output of a linear system or estimation of the causality.
The coherence between two signals is defined as:

$$\gamma_{xy}^2(f) = \frac{|\Phi_{xy}(f)|^2}{\Phi_{xx}(f)\Phi_{yy}(f)} \tag{3.9}$$

$\Phi_{xy}(f)$, $\Phi_{xx}(f)$ and $\Phi_{yy}(f)$ are the cross- and auto-spectral density as defined in subsection 3.1.2.

3.2 Evaluation of pressure from velocity field

Equation 2.19 and Equation 2.20 both require the pressure distribution on the airfoil. The pressure is related to the velocity by the Navier-Stokes equations and

the spatial gradients of pressure can be expressed in either the Eulerian (Equation 3.10) or the Lagrangian formulation (Equation 3.11) as:

$$\nabla p = -\rho \left(\frac{\partial \mathbf{u}}{\partial t} + (\mathbf{u} \cdot \nabla)\mathbf{u} - \nu \nabla^2 \mathbf{u} \right) \tag{3.10}$$

$$\nabla p = -\rho \left(\frac{D\mathbf{u}}{Dt} - \nu \nabla^2 \mathbf{u} \right) \tag{3.11}$$

For the data acquired from PIV measurements, the pressure distribution needs to be reconstructed from the velocity field. Two strategies are available for the computation of the pressure field:

1. direct spatial integration [2],
2. in-plane Poisson [18].

In strategy (1), the pressure gradients are integrated with spatial marching scheme from the boundaries where Dirichlet boundary condition is assigned. The method introduces the accumulation of random errors along the integration path and thus a dependence of the accuracy on the path. Liu and Katz (2006) [42] have developed an omni-directional virtual boundary integration scheme to integrate the acceleration while minimizing the effect of local random error. Strategy (2) takes the in-plane divergence of Equation 3.10 or Equation 3.11 such that the equation about pressure is rearranged into a Poisson equation:

$$\frac{\partial^2 p}{\partial x^2} + \frac{\partial^2 p}{\partial y^2} = -\rho f_{xy} \tag{3.12}$$

where the source term f_{xy} is a function of velocity and can be decomposed into the component of 2D and 3D. For high Reynolds number, the viscous term can be

neglected [66], and thus:

$$
\begin{aligned}
f_{xy} = f_{2D} + f_{3D} &= -\rho \nabla_{xy} \frac{D\mathbf{u}}{Dt} \\
&= \left[\left(\frac{\partial u}{\partial x} \right)^2 + 2 \frac{\partial v}{\partial x} \frac{\partial u}{\partial y} + \left(\frac{\partial v}{\partial y} \right)^2 \right] \\
&+ \left[\frac{\partial (\nabla_{xy} \cdot \mathbf{u})}{\partial t} + (\mathbf{u} \cdot \nabla)(\nabla_{xy} \cdot \mathbf{u}) + \frac{\partial w}{\partial x} \frac{\partial u}{\partial z} + \frac{\partial w}{\partial y} \frac{\partial v}{\partial z} \right]
\end{aligned}
\tag{3.13}
$$

Test cases applying Equation 3.12 can be found in literatures such as [11] [12]. The different approaches (Lagrangian and Eulerian) yield different performance. Violato et al. (2011) [68] compare the two approaches on a rod-airfoil configuration and offer guidelines to the choice of experimental parameters according to the approach adopted. According to the authors, the Lagrangian approach is less sensitive to measurement noise. De Kat and van Oudheusden (2012) [10] further assessed the experimental viability of the approaches in the reconstruction of instantaneous pressure field, giving emphasis on the flow features of convecting vortices.

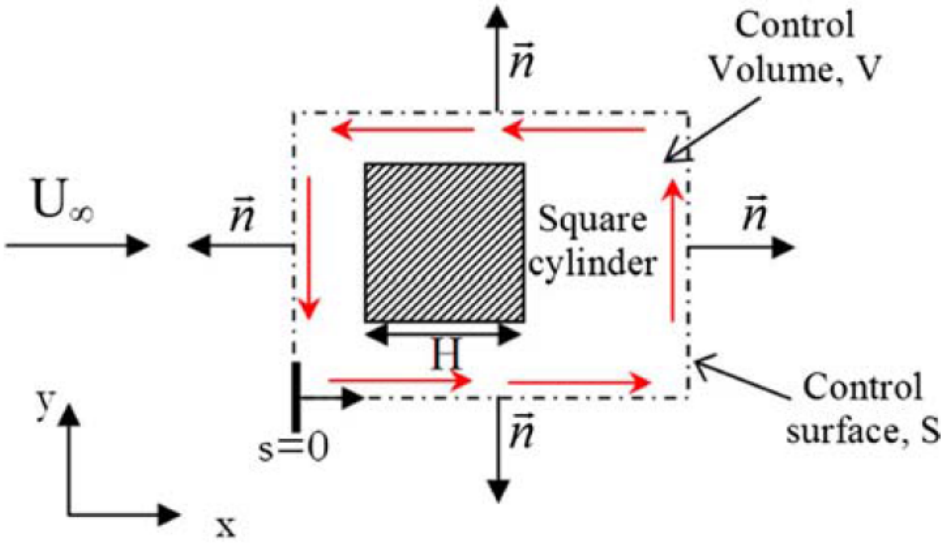

Figure 3.1: Control volume and Control surface around the cylinder [37]

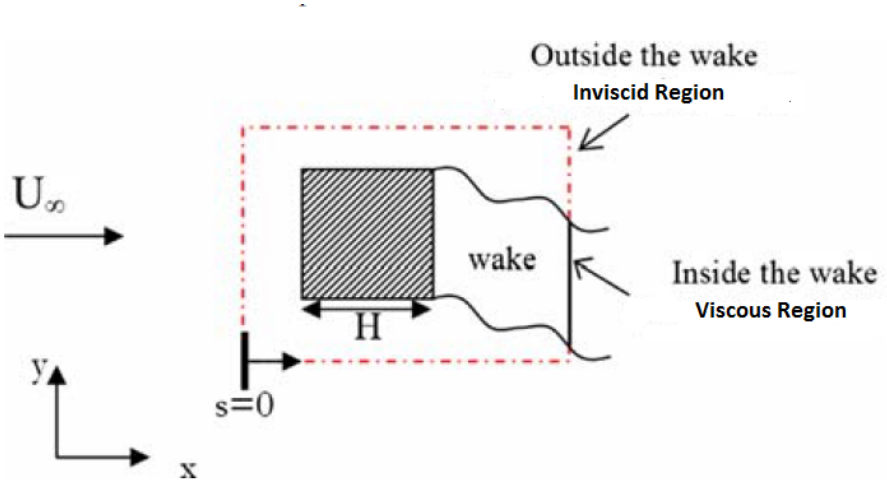

Figure 3.2: Definition of Inviscid and Viscous region on the Control surface [37]

3.3 Evaluation of aerodynamic forces from velocity field

With the pressure field reconstructed in section 3.2, there is still one step before the application of the lumped form Curle's analogy (Equation 2.20), the evaluation of instantaneous aerodynamic forces exerted on the solid body. This section introduces two method for evaluating aerodynamic loads from PIV measured velocity field.

Evaluation of aerodynamic loads based on reconstructed pressure

Kurtulus et al. (2007) [37] estimate the unsteady forces on a square cylinder from the velocity field measured by planar TRPIV. In this article, the aerodynamic forces are evaluated by integrating the momentum balance equation within a control volume enclosing the square cylinder (Figure 3.1). The general integral form of the momentum balance is written as:

$$\vec{F}(t) = -\rho \iiint_V \frac{\partial \vec{V}}{\partial t} dV - \rho \iint_S (\vec{V} \cdot \vec{n}) \vec{V} dS - \iint_S p \vec{n} dS + \iint_S \bar{\bar{\tau}} \vec{n} dS \quad (3.14)$$

In this case the planar PIV measurement cannot resolve the out-of-plane velocity, only 2D components are considered. In addition, with the outer boundary of the control volume sufficiently far from the body surface, the viscous effect is neglected, resulting in:

$$\begin{bmatrix} D \\ L \end{bmatrix} = -\rho \iint_V \begin{bmatrix} \frac{\partial u}{\partial t} dxdy \\ \frac{\partial v}{\partial t} dxdy \end{bmatrix} + \rho \oint_S \begin{bmatrix} -u^2 dy + uv dx \\ -uv dy + v^2 dx \end{bmatrix} + \oint_S \begin{bmatrix} -p dy \\ p dx \end{bmatrix} \quad (3.15)$$

The authors of [37] proposed a robust procedure for the evaluation of the pressure terms on the control surface in Equation 3.15. As shown in Figure 3.2, the part of control surface hit by the wake is defined as 'viscous region', where pressure is obtained by integrating Equation 3.11, but neglecting the viscous contribution. To minimize the effect of error propagation in the process of spatial integration, outside the wake, pressure is estimated by Bernoulli equation. In such a way, pressure in the wake region can be resolved by integrating from both edges of the wake, and the end point of integration, lying in the inviscid region, can be compared with the value given by Bernoulli equation. The discrepancy between

the integration result and the Bernoulli equation can then be used to redistribute the discrepancy along the viscous region with a linear weighting function. The above mentioned technique is derived and applied to the incompressible scenario, an extension of this method to the application of compressible flow can be found in [66], where a test-case with the supersonic flow around a bi-convex airfoil is presented.

Evaluation of aerodynamic loads directly from velocity measurements

There are alternative methods for evaluation of time-dependent forces which circumvent the step of pressure reconstruction and depend only on the velocity measurements obtained in an arbitrarily chosen region enclosing the solid body. Three expressions for a solid body, moving or steady, immersed in an incompressible, viscous and rotational flow are presented and compared by Noca et al.(1999)[50]. The three expressions, all derived from the integral form of momentum equation (Equation 3.14), are referred to as the "Impulse equation", the "Momentum equation" and the "Flux equation". According to the authors, the volume integrals over the control volume required in the force evaluation of the "Impulse equation" and the "Momentum equation" can be prohibitive as the velocity field within the boundary layers of the solid body is not well-resolved. The "Flux equation" circumvents the problem by adding an additional constraint of the velocity field being divergence free ($\nabla \cdot \mathbf{u} = 0$). In such a way, only surface integrals are involved in the equation. The simply-connected domain is constructed by umbilicus to transform the volume integrals to surface integrals, as shown in Figure 3.3. When the solid body is non-permeable and fixed, the "Flux equation" can be written as:

$$\mathbf{F} = \oint_{S(t)} \hat{\mathbf{n}} \cdot \gamma_{flux} dS \tag{3.16}$$

with

$$\begin{aligned} \gamma_{flux} =& \frac{1}{2}u^2\mathbf{I} - \mathbf{uu} - \frac{1}{N-1}\mathbf{u}(\mathbf{x} \wedge \omega) + \frac{1}{N-1}\omega(\mathbf{x} \wedge \mathbf{u}) \\ & - \frac{1}{N-1}\left[\left(\mathbf{x} \cdot \frac{\partial \mathbf{u}}{\partial t}\right) I - \mathbf{x}\frac{\partial \mathbf{u}}{\partial t} + (N-1)\frac{\partial \mathbf{u}}{\partial t}\mathbf{x}\right] \\ & + \frac{1}{N-1}[\mathbf{x} \cdot (\nabla \cdot \mathbf{T})\mathbf{I} - \mathbf{x}(\nabla \cdot \mathbf{T})] + \mathbf{T} \end{aligned} \tag{3.17}$$

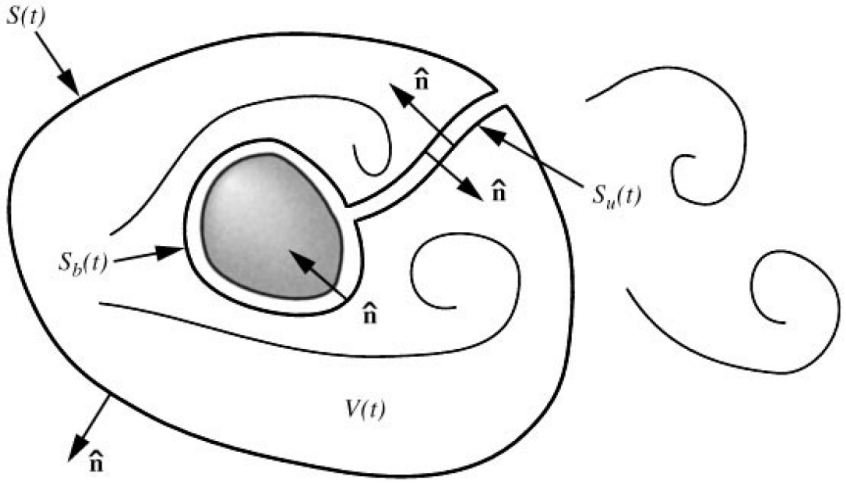

Figure 3.3: Construction of simply-connected domain[50]

where $\hat{\mathbf{n}}$ is the surface normal, N is the spatial dimension, ω is the vorticity, $\mathbf{x}$ is the position vector, $\mathbf{I}$ is the unit tensor and $\mathbf{T}$ is the viscous stress tensor. The authors of [50] recommended that the forces be evaluated from the data across the region of the wake where the vorticity and viscous effects are present since it is probable that the surface integration of the product of $\mathbf{x}$ and $\partial\mathbf{u}/\partial t$ may not converge in the far-wake. Although in 2-D measurements, the divergence-free condition may not be satisfied for the "Flux equation", yet concerning the spurious divergence of velocity field generated by the measurements in the boundary layers of the solid body, the "Flux equation" is still strongly preferred in such situation.

Chapter 4

Experimental techniques

For engineers, theories are not the central objectives, nor an end in itself, but a means to the utilitarian end: the incarnation of the idea of people. Quotes of statement made by a British engineer to the Royal Aeronautical Society in 1922 acknowledged the gap between scientific theories and engineering [67]:

Aeroplanes are not designed by science, but by art in spite of some pretence and humbug to the contrary. I do not mean to suggest for one moment that engineering can do without science, on the contrary, it stands on scientific foundations, but there is a big gap between scientific research and the engineering product which has to be bridged by the art of the engineer.

Experimental research is one of the art of engineer, which not only is effective in validating the prediction made by scientific theories, but also provide information that are out of the reach of modern theories, furthermore, can reversely produce analytical concepts and way of thinking, as with the case of Durand and Lesley's idea of propulsive efficiency of a propeller in front of an obstruction.

In the history of aerodynamics, it is often most fruitful theories and experiments are employed in interactive proximity, such as the Durand-Lesley propeller test, the development of laminar-flow airfoil and the recognition of the relationship between dynamic response and flying qualities etc.. Because of development of more advanced measurement devices, the magic of the art of engineers has been enhanced.

Upon the topic of Gurney flap aerodynamics and aeroacoustics, a various of experimental techniques have been applied for the flow visualization and acoustic measurements. In the current study, particle image velocimetry (PIV) measurements are designed to measure the velocity field and from which derive the related field quantities as described in section 3.2 and 3.3. Microphone measurements are used to acquire the noise spectra in the far-field, which can serve as a comparison to the quantities derived from PIV measurement. The quantities can thus be compared in the domain of both time and frequency, with the techniques described in section 3.1.

This section gives a brief introduction on PIV and microphone measurement techniques, the knowledge of which is indispensable for the design of experimental set-up. In section 4.1, the microphone measurements and related data reduction techniques are described. In section 4.2 the history, the working principle, the main components and the velocity evaluation techniques of PIV system are illustrated.

4.1 Microphone Measurement

Microphone measurement is a direct way to characterizing the acoustic field. A microphone is an acoustic-to-electric transducer that converts the sound pressure into electrical signal. Microphones can be further classified according to the quantity measured, the generation of electric signal, or the directivity. For the current study, the LinearX-M53 microphones are applied in experiments for low noise and low distortion measurement. Since the model is condenser microphone, the following introduction will be focused on condenser microphones with the example

offered by Linear X-M53. For detailed information on working principle of other types of microphones, and the recording techniques for various objectives, one can refer to [14].

Figure 4.2 shows the electronic scheme of a typical condenser microphone. A diaphragm and a backplate form a capacitor, the capacity of which is defined by:

$$C = \frac{\epsilon A}{d} \tag{4.1}$$

where ϵ is the dielectric constant of the substance between the two plates, d and A are the dimensions of the capacitor.

The diaphragm is excited to vibrate by the impinging pressure fluctuation caused by the acoustic wave, and thus the distance between the two plates d is changing with the variation of impinging pressure on the diaphragm. When the charge stored by the capacitor Q is kept constant, according to the capacity law, the voltage V between the two plates responses linearly and continuously to the pressure fluctuation:

$$V = \frac{Q}{C} = \frac{Q}{\epsilon A} d \tag{4.2}$$

The resistor functions as a high pass filter. In such a way, the output voltage measures only the fluctuating part of the pressure signal.

The following sections expatiate on the microphone sensitivity and placement, as well as the data reduction procedure to convert the voltage back to acoustic pressure. These aspects are essential for succeeding in capturing sound with microphone. For measurements of good quality, there are other factors one needs to consider, such as background noise and reflection etc. (refer to [47]), which are beyond the discussion of this article for the concern of brevity.

4.1.1 Microphone sensitivity

Microphone sensitivity defines the ratio between the output voltage and the input pressure signal. The sensitivity is depicted in two dimensions:

- **Directional sensitivity**
  Directional sensitivity, or directionality, describes the microphone's sensitivity to sound from various directions.
- **Frequency sensitivity**
  Frequency sensitivity, or angular sensitivity, describes the amplitude response of microphone to signal of different frequencies.

Figure 4.3 shows the directional sensitivity of Linear X-M53. It can be observed that in audible frequency range (20 Hz to 20 kHz), the model is essentially omnidirectional. When moved to higher frequencies, the sensitivity lobe moves to the front and the directionality becomes hypercardioid.

Figure 4.4 shows the frequency sensitivity of Linear X-M53. It can be observed that from 50 Hz to 10 kHz, the ratio between output and input signal is roughly constant. The reason behind this phenomenon is due to the schematic of the condenser microphone. In the range of frequency below 50 Hz, the amplitude of fluctuation is large due to the large amount of energy contained by the low frequency components. The displacement of diaphragm is insufficient to measure the amplitude of fluctuation in this frequency range, resulting in the low sensitivity. In the frequency range above 10 kHz, the response first increases then quickly drops because of the insufficiency of the dynamic response. The time lag introduced by the diaphragm-condenser system causes out-of-phase cancellation.
Microphone response can be corrected to acquire a constant response with the frequency, which requires a source in anechoic environment with known constant amplitude and position.

4.1.2 Microphone placement

To determine the microphone placement in the experiments, several characteristics should be taken into consideration, such as source directivity, near-field effect, background noise and reflections. The scope of this study focuses on the validation of method of acoustic prediction by PIV where microphone measurements

only offer a comparison of acoustic pressure at certain locations and thus does not include the mapping of acoustic source. Therefore the major concern of microphone placement lies in avoiding the near-field effect while having sufficient signal to noise ratio.
Microphones placed in the near-field region measure the radiation sound and the pseudo-sound at the same time, resulting in the loss of representation of the sound propagating to the far-field. To avoid this effect, acoustic measurements are usually conducted in the far-field, in which the microphone is placed at least one acoustic wavelength and two source dimensions away from the source.
On the basis of far-field measurement, the microphone should be placed in the region close to the source, such that the sound level of the source is strong enough to dominate the background noise as well as the reflections. The signal-to-noise difference is preferred to be above 10 dB. In occasions where 10 dB is not achievable, a lesser difference is tolerable as long as the interfering noise can be separated from the data.[47]

4.1.3 Data reduction procedure

Data recorded by microphones is in voltage. To derive the sound pressure in Pa from the voltage, calibration with piston phone calibrator is required. The G.R.A.S. Pistonphone 42AA used in this study produces a sound source of 114 dB at 250 Hz. Before the measurement, the microphone first record a 30-second signal of the sound generated by the piston phone. The recording can be used to derive the transfer function of the measuring system.
Equation 4.2 shows the linear relation between sound pressure input and voltage output. Further, it can be seen in Figure 4.4 that the output-to-input ratio remains roughly constant in range between 50 Hz and 10 kHz. Additionally, frequency out of this range falls out of the interest of this study. The reason is that below 50 Hz, the sound is basically background noise; above 10 kHz, the amount of energy contained by this frequency range is several orders smaller than in the range of lower frequency. Thus, a constant output-input ratio can be assumed for all frequencies, as in Figure 4.5.

From Equation 1.1, the root mean square of sound pressure can be calculated by:

$$P = P_0 \cdot 10^{\frac{SPL}{20}} (SPL = 114dB) \tag{4.3}$$

And with the root mean square of voltage V acquired from the microphone recording, the output-input ratio H can be thus written as:

$$H = \frac{V}{P} \tag{4.4}$$

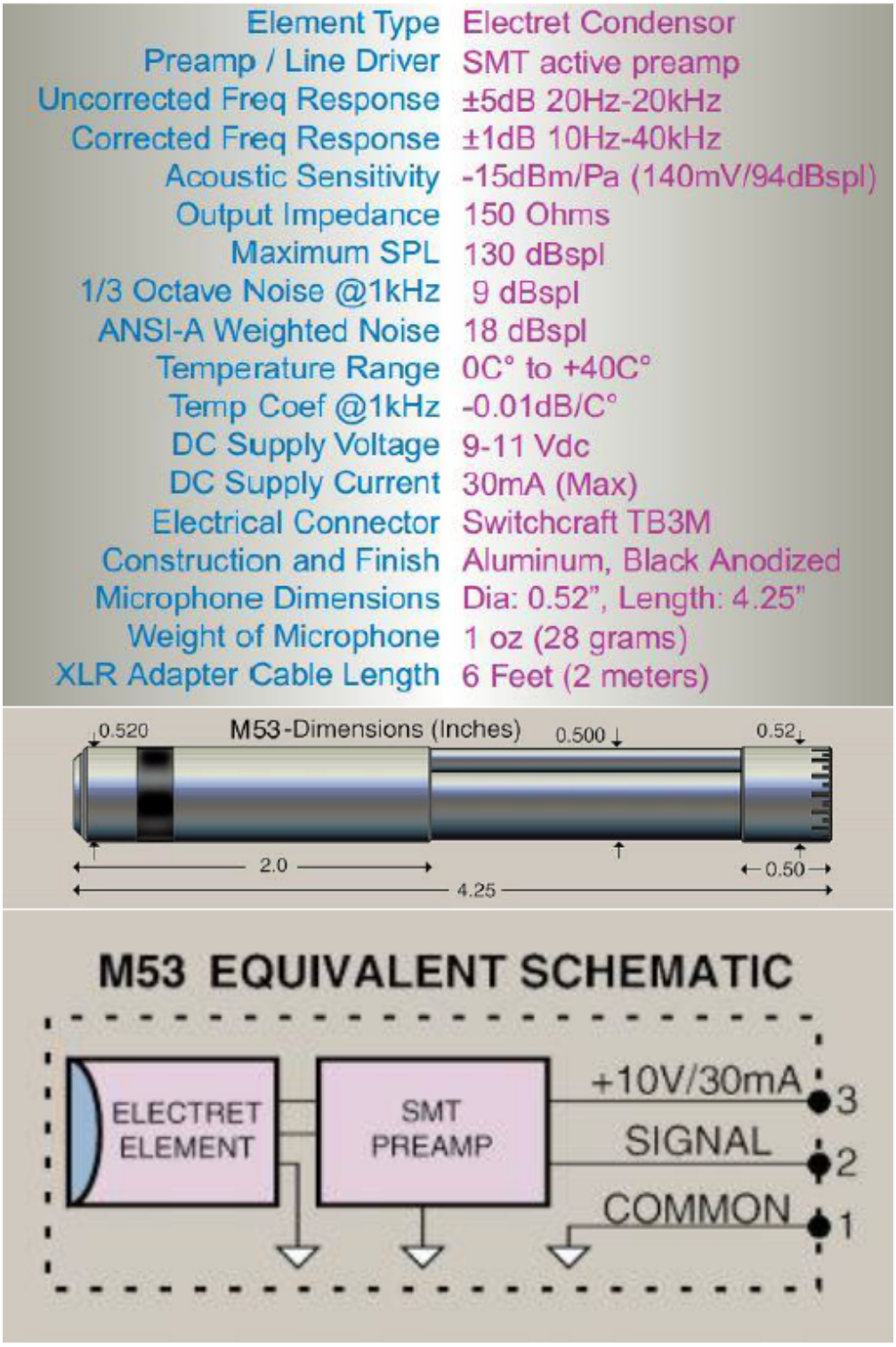

Figure 4.1: The technical chart, the dimensions and the equivalent schematic of a Linear X-M53 microphone[31]

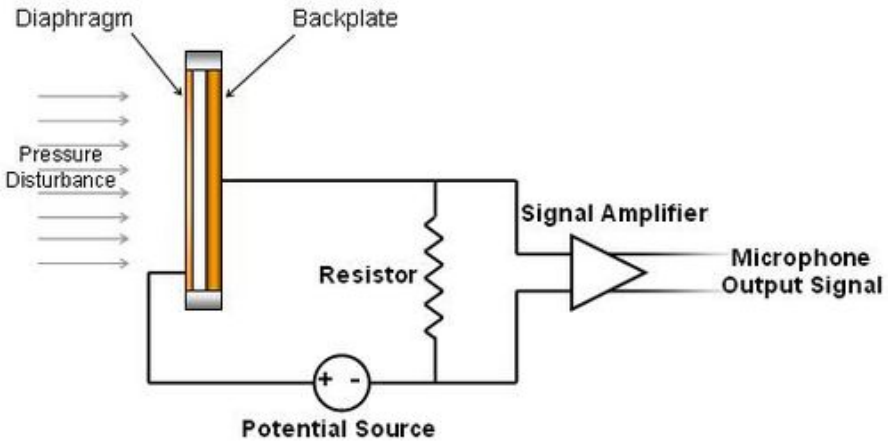

Figure 4.2: Electronic scheme of a condenser microphone

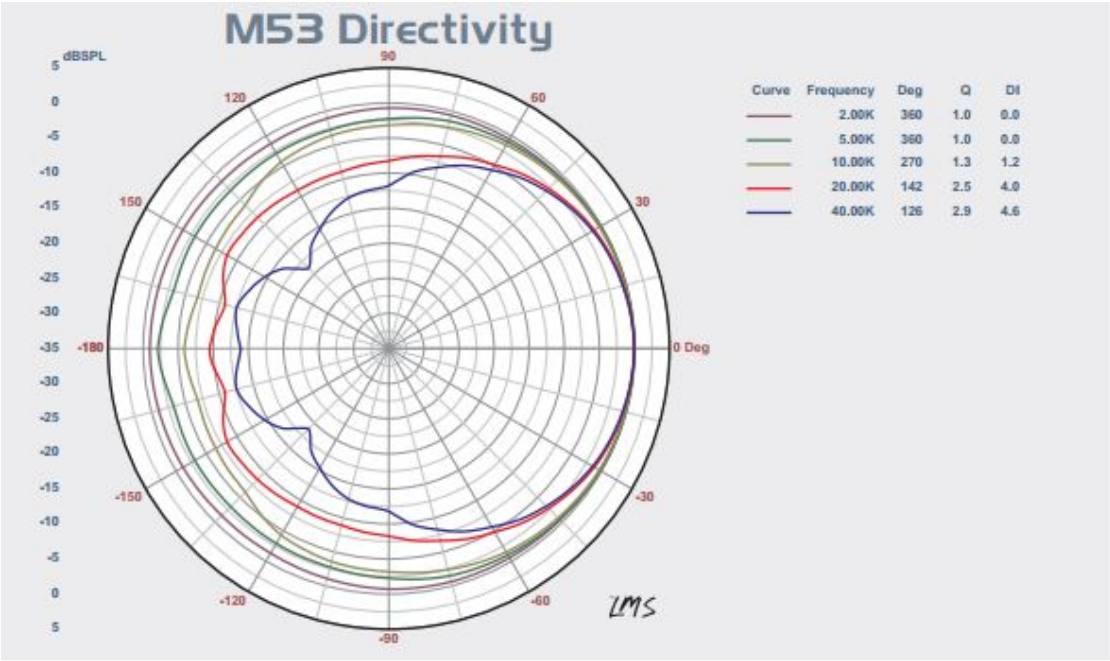

Figure 4.3: Directivity at different frequencies of a Linear X-M53 microphone[31]

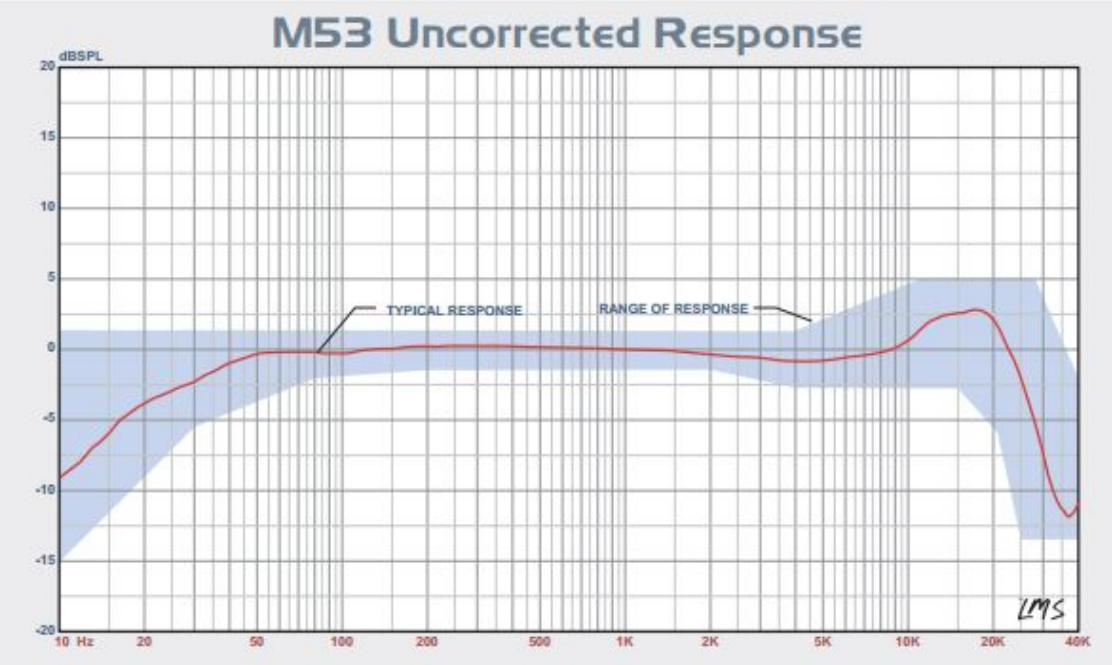

Figure 4.4: Original frequency response of a Linear X-M53 microphone[31]

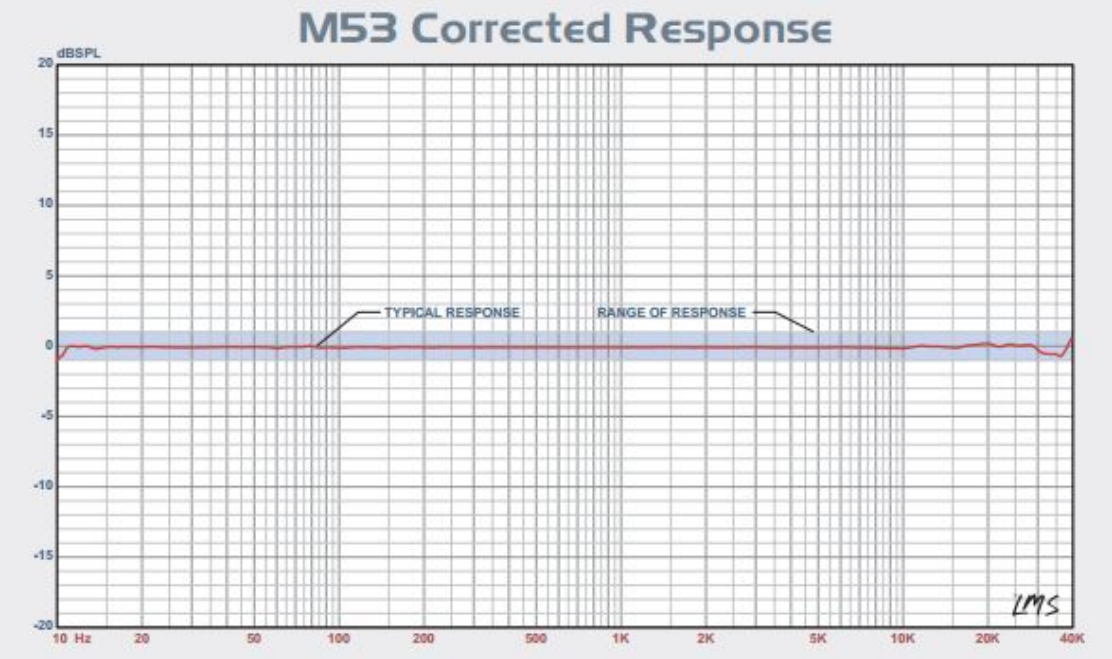

Figure 4.5: Corrected frequency response of a Linear X-M53 microphone[31]

Figure 4.6: G.R.A.S. Pistonphone 42AA

4.2 Particle image velocimetry

Particle image velocimetry (PIV) is a non-intrusive measurement technique for research and diagnostics of flow field. The velocity measurement of PIV is based on the measurement of the displacement of tracer particles δx carried by the flow during a short time interval δt. The tracer particles are seeded into the flow and illuminated by a thin light sheet or a small light volume. The light scattered by the particles is recorded with high speed cameras onto two subsequent image frames, from which the displacement of the particles can be determined. And thus the local velocity of the flow can be calculated by:

$$U = \frac{\delta x}{\delta t} \tag{4.5}$$

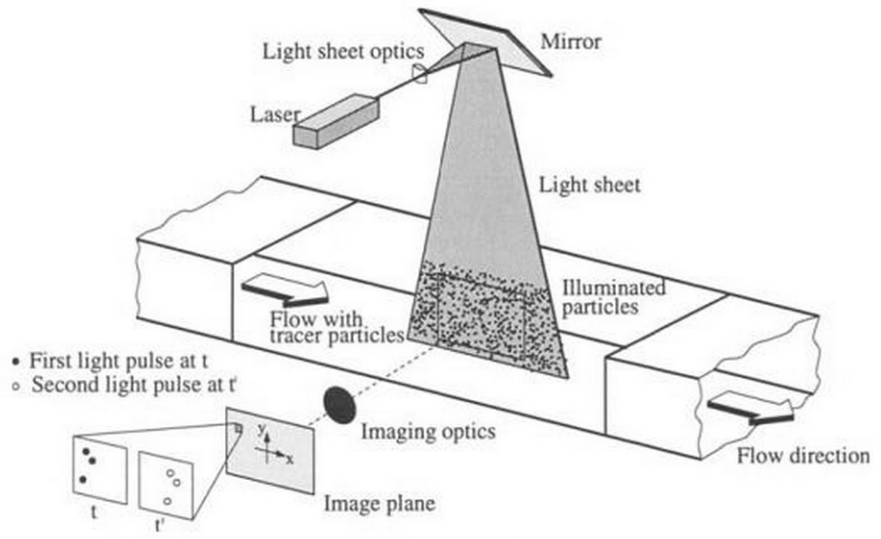

Figure 4.7: PIV working principle[57]

The idea of PIV is derived from the laser speckle velocimetry used by several research groups in late 1970s, and was greatly developed in the following decades. The availability of high-speed lasers and cameras allows for variations upon the original idea, such as:

- **Standard planar PIV**
  Standard planar PIV measures two velocity components in a 2D plane with a single camera.
- **Stereoscopic PIV**
  Stereo-PIV measures three velocity components in a 2D plane with two cameras.
- **Tomographic PIV**
  Tomo-PIV measures three velocity components in a volume using two, or more cameras.
- **Time-Resolved PIV**
  Time-Resolved PIV benefits from the advances in CMOS camera technology to enable the measurement with high time-resolution.

A comprehensive review on PIV techniques and related applications can be found in [57]. The following sections will mostly focus on time-resolved planar and stereo PIV, since they are employed in the experiments of this study.

4.2.1 Seeding

Tracer particles play a vital role in PIV. There are essentially three requirements for the particles:

- The particles should exactly follow the motion of the fluid flow.
- The particles should not alter the local flow patterns.
- The particles should scatter light efficiently.

To choose the proper tracer particle that meets the demands, the mechanical properties and the scattering properties of the particle should be considered.

Mechanical properties

For very small particles in low speed motion, the quasi steady viscous term, namely the Stokes drag dominates the particle dynamics. The difference between the particle velocity $\mathbf{V}$ and that of the surrounding fluid $\mathbf{U}$ is used to describe how well the tracer particle can follow the flow. This difference is often referred to as *slip velocity* and is defined as:

$$\mathbf{V} - \mathbf{U} = \frac{2}{9}a^2 \frac{\rho_p - \rho_f}{\mu} \frac{d\mathbf{V}}{dt} \tag{4.6}$$

where $a = \frac{1}{2}d_p$ is the radius of the tracer particle, μ is the dynamic viscosity of fluid, ρ_p and ρ_f are the density of particle and fluid respectively.
When $(\rho_p - \rho_f)(\rho_f) << 1$, the particle is said to be neutrally buoyant. Equation 4.6 indicates that the motion of fluid is well represented by the tracer particles when the buoyancy neutral condition is satisfied and the diameter of the particle is small. For gas flows, $(\rho_p - \rho_f)/\rho_f << 1$ cannot be achieved. Thus typical values of density ratio $(\rho_p - \rho_f)/\rho_f = O(10^3)$ and small particle diameter $(0.5\mu m < d_p < 5\mu m)$ are employed in gas flows.
Since the term $d\mathbf{V}/dt$ is difficult to characterize, the ratio between the particle time response τ_p and the characteristic flow time scale τ_f, namely the *Stokes number* is used as an indication of the tracer particle's ability to follow the flow.

$$St = \frac{\tau_p}{\tau_f} \tag{4.7}$$

where

$$\tau_p = \frac{1}{18}d_p^2 \frac{\rho_p - \rho_f}{\mu} \tag{4.8}$$

Theoretically, Stokes number should be $St << 1$. In gas flow, for practical limitations, $St < 0.1$ is used.

Scattering properties

The scattering efficiency of the tracer particles depends on:

- ratio between the refractive index of particle and fluid n_p/n_f
- wavelength of incoming light λ^{-4}
- particle diameter d_p

Wavelength is restricted by laser and camera sensor and thus cannot be chosen freely. To acquire a high refractive index ratio, material of high index of refraction is preferred. Furthermore, according to Mie's theory, particle of large diameter is advantageous.

It can be seen that the indications in the choice of particle diameter given by mechanical properties and scattering properties are contradictory. The most common approach is to choose the largest particle that can follow the flow accurately.

4.2.2 Illumination

Due to the working principle of PIV measurements, there are several requirements on the illumination. First, the particles should be sufficiently illuminated such that the scattered light can be captured by the camera sensor. Second, the illumination should be in short duration, such that the particle images do not appear as streaks. Third, the light provided by the light source can be shaped into thin sheet that only particles lying within can be imaged in focus.
For the requirements mentioned above, in PIV setups, lasers are often used as the light source due to their ability to provide light beam that is:

- of high energy in short pulses,
- with low chromatic aberrations,
- collimated with approximately plane wave front.

Lasers differ in the laser material, geometrical dimensions, power consumption, pulse energy, pulse repetition rate and wavelength of emitted light. In this study,Nd:YLF (lasers based on neodymium-doped yttrium lithium fluoride crystals) is used. The light is emitted primarily at 1053 nm and then turned into visible green light of 526 nm by crystal frequency doubler. Currently the pulse energy emitted by Nd:YLF laser ranges between 10 to 30 mJ, at a repetition rate of 1 to 5 kHz.

A set of optics is used to transmit the light and to form the light sheet. Typically, the light beam is shaped into a thin light sheet with the combination of spherical lenses and cylindrical lenses. Either, it is a combination of cylindrical concave lens (expanding the beam) followed by two orthogonal cylindrical convex lenses (converging into light sheet); or, it can be a combination of a concave spherical lens, followed by a convex spherical lens.

4.2.3 Imaging

The imaging system is characterized by the focal length f, the aperture number $f_\#$ and the magnification factor M. Focal length and magnification factor are related to image distance d_i and object distance d_o in the thin lens approximation, by:

$$\frac{1}{f} = \frac{1}{d_i} + \frac{1}{d_o}; M = \frac{d_i}{d_o} \tag{4.9}$$

The aperture number (also referred to as f-number), is defined as the ratio of focal length f and the aperture diameter D. However, in practice, $f_\#$ is determined by the magnification factor and the thickness of the light sheet. The relation is explained as follows.

The focal depth δz is the depth within which the particles are in focus, and is described by the wavelength of the light source λ, the f-number and the magnification factor as:

$$\delta z = 4.88\lambda f_\#^2 \left(\frac{M+1}{M}\right)^2 \tag{4.10}$$

δz should be larger or equal than the light sheet thickness Δz, which is about 1mm in practice.

There is a trade-off in the choice f-number, since a large f-number allows a higher depth of field while a small f-number enhances the light intensity collected by the sensor. This issue is far from trivial for recordings with high repetition rate where the power per pulse decreases.
The diameter of particle image d_τ depends on the geometric optics effect and the diffraction effect:

$$d_\tau = \sqrt{(Md_p)^2 + (d_{diff})^2} \tag{4.11}$$

where

$$d_{diff} = 2.44\lambda(1 + M)f_\# \tag{4.12}$$

Typically, the term (Md_p) is much smaller than d_{diff} and hence can be neglected. The particle image diameter is a parameter concerning the accuracy of velocity measurements. When the particle image occupies less than one pixel, it is referred to as *peak locking*, which lowers the accuracy of measurement since the particle positions are locked to integer values and cannot be detected with subpixel accuracy.

4.2.4 Recording

High-speed cameras used in PIV measurements usually store the images in memory on board during the measurement and later transfer to the computer. For the current study, cameras with CMOS sensors are used. The CMOS cameras available offer frame rates of over 5000 frames per second for full mega pixel resolution (1024×1024 pixels). Higher frame rates can be reached when sensor is cropped. For example, at 512×512 pixel resolution, 10,000 frames per second can be reached. In the current study, Double Frame/Single Exposure acquisition is used. The camera shuttering time and the laser pulses are synchronised in so-called frame straddling mode, as shown in Figure 4.8, where T_{shut} is the camera shutting and data transfer time, δt is the laser pulse separation and Δt is the acquisition time of an image couple.

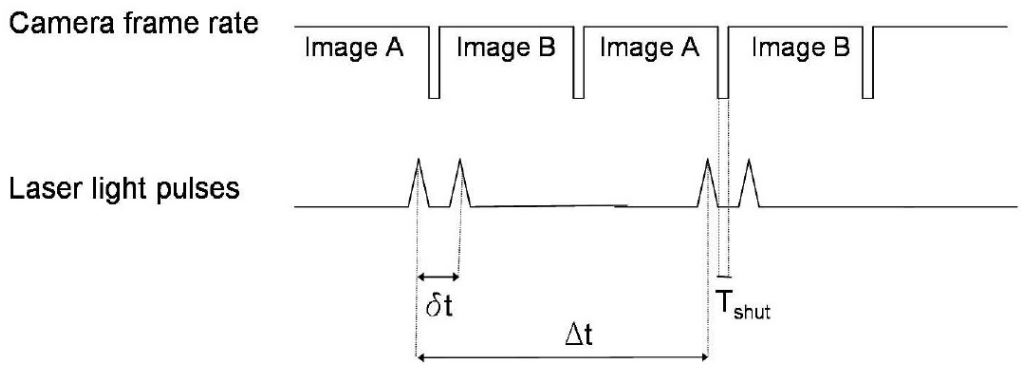

Figure 4.8: Timing diagram for PIV recording based on Double Frame/Single Exposure frame straddling mode [44]

4.2.5 Image interrogation

To evaluate the velocity of the flow field, the displacement of particles during the pulse separation δt should be evaluated from the two subsequent image frames. The steps and rules to follow are described as follows.

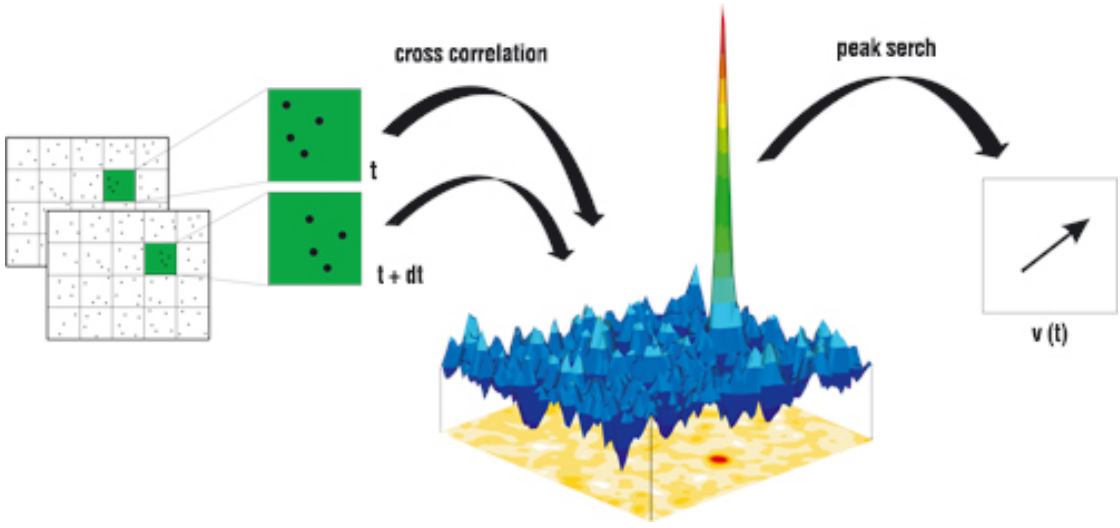

Figure 4.9: Procedure of evaluating velocity from PIV images[16]

1. **Image windowing**

   Since the displacement of particles is usually not uniform on the entire region, the image is first partitioned into small windows, inside which the displacement is assumed to be uniform. To optimize between the pulse separation and window size, there are a few rules:

   - The maximum in-plane displacement should be smaller than 1/4 of the window size.
   - The maximum out-of-plane displacement should be less than 1/4 of the light sheet thickness.
   - The maximum in-plane variation of particle image displacement for particles inside the same window should not exceed the particle image diameter.

2. **Cross-correlation analysis**

   Cross-correlation is applied the image pair to determine the particle displacement in each window. Let $I(x, y, t)$ and $I'(x, y, t + \delta t)$ the two interrogation window at time t and time $t+\delta t$ as shown in Figure 4.9. The cross-correlation function Φ is computed in its discrete form reads:

   $$\Phi(m, n) = \frac{\sum_{i=1}^{I} \sum_{j=1}^{J} I_A(i, j) \cdot I_B(i + m, j + n)}{\sqrt{\sum_{i=1}^{I} \sum_{j=1}^{J} I_A^2(i, j) \cdot \sum_{i=1}^{I} \sum_{j=1}^{J} I_B^2(i, j)}} \tag{4.13}$$

   The m and n corresponding to the largest Φ define the displacement in integer number of pixels.

3. **Sub-pixel interpolation**

   The displacement in pixels defined by correlation coefficient Φ defines only discrete pixel locations. In order to reach sub-pixel precision, the correlation peak is interpolated, typically by means of Gaussian interpolator, around the maximums as shown in Figure 4.10. There are additional peaks besides the main peak on the correlation coefficient plot due to noise and correlation of non-paired particles. Assume the value of highest peak be Φ_1, the second highest peak Φ_2, and the correlation signal-to-noise ratio can be defined as shown in Equation 4.14.

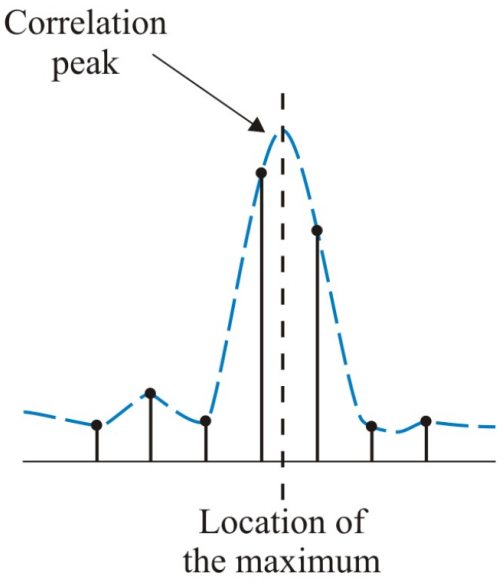

Figure 4.10: Sub-pixel interpolation of correlation peak[15]

$$SN = \frac{\Phi_1}{\Phi_2} \tag{4.14}$$

Usually, small interrogation window is preferred for higher vector resolution, especially in the case where fine flow patterns are involved. However, this requirement give rise to the problem of the reduction in image density N_I and hence the information contained in one interrogation window. Another disadvantage with small interrogation window is particles escaping the computation domain, namely *Loss-of-pairs*. The above mentioned two defects both lead to rise in the uncertainty of particle image displacement.

The Multi-pass interrogation is a solution to this issue. The method is an iterative process, in which a relatively large interrogation window is used to produce an initial velocity approximation; then, the approximated velocity is used to shift (or deform) the correlation windows. In each iteration, the window size decreases and corrections are applied to the location of correlation peak.

Peak-locking should be avoided for reliable PIV measurement, since particle image much smaller than pixel size leads to discontinuous velocity field. Theoretically, $f_\#$ should be increased for larger particle image. However, in the case where the

pulse duration is short due to high acquisition frequency, small $f_{\#}$ is required for the sake of image contrast. In such case, a slight defocusing of the camera lenses helped to avoid this effect in practice.

Chapter 5

Experimental set-up

Given the experimental techniques presented in chapter 4, this chapter furthers the discussion on the experimental set-up for the aeroacoustic investigation of the Gurney flap. The experiments can be divided into two categories: (i) the synchronized planar PIV and acoustic measurement, from which noise is evaluated from the measured velocity field and then is compared with the simultaneous microphone recording, and (ii) the stereoscopic PIV measurement, which takes into consideration of 3D effect that is beyond the reach of planar PIV measurement and in such a way correcting the predicted noise level.

The facilities and models to fulfil the above mentioned measurements are introduced in section 5.1. The detailed experimental parameters and arrangements are then presented in the two sections that follow: section 5.2 and section 5.3. In section 5.4, a brief description on retrieving velocity field from PIV raw images is presented. This study is a continuation of the work of J.Shah [63]. For this reason, the airfoil and Gurney flap model, the wind tunnel, and the experimental conditions were remained the same as in the previous work. The modifications to the previous set-up is due to the choice of PIV field of view (FOV), which is enlarged to enable the flow visualization on both sides of the airfoil for the reason of acoustic predictions. In addition, the FOV of the planar PIV measurements are shifted

upstream and downstream in different rounds of measurements for the parametric study of the optimum FOV location for acoustic related PIV measurements.

5.1 Facilities and models

All experiments of this study are carried out with the facilities and equipment available on campus of Delft University of Technology. The following sections give a brief introduction on the experimental facilities and models. The wind tunnel and test sections used for this study are introduced in subsection 5.1.1, following which, the airfoil and trailing edge models are presented in subsection 5.1.2.

5.1.1 Wind tunnel facility

The wind tunnel test was carried out at the vertical low turbulence wind tunnel (V-tunnel) located in the Low Speed Laboratory (LSL) at Delft University of Technology. The V-tunnel has an open test section with a vertical inflow coming from below, with an operating velocity range of 5 - 45 m/s. Figure 5.1 shows the schematics of the V-tunnel.

A circular exit with a diameter of $0.6m$ leads the inflow to the open section. In this study, due to the requirements of model installation and acoustic measurement, a transition duct was installed on top of the circular exit to accommodate the square test section sized $0.4 \times 0.4m^2$.

The reasons for choosing V-tunnel for this study are: (i) the low turbulence level of the inflow (below 0.1%) due to the high contraction ratio between the settling chamber and the open-section exit, such as to provides incoming flow with high flow quality, and (ii) the relatively low operating noise level, which makes the tunnel suitable for accommodating acoustic measurements in absence of an anechoic wind tunnel. For PIV measurement alone, the closed test section was built from plexiglass. For synchronized PIV and acoustic measurement, two side walls of the test section were substituted with Kevlar, which is transparent for acoustic waves

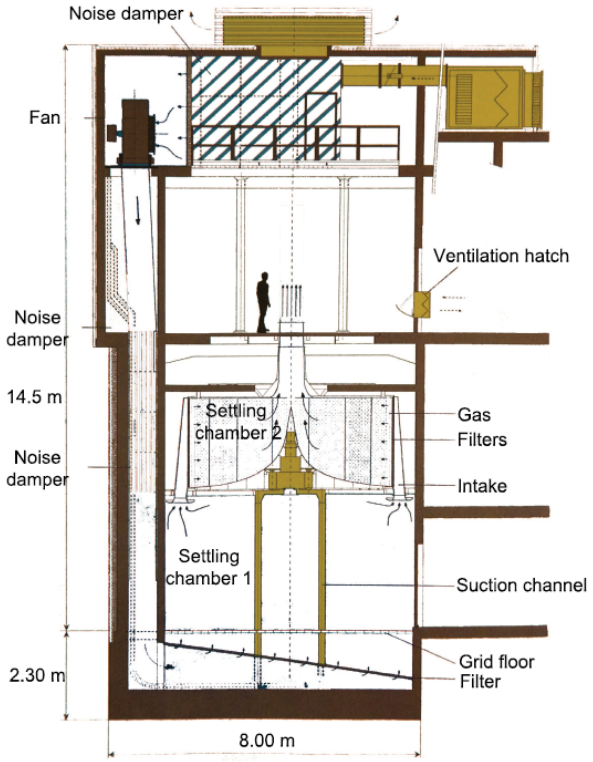

Figure 5.1: Schematic of vertical low turbulence wind tunnel (V-tunnel) in TU Delft [55]

[13] but impermeable (at least to some degree) to air flow.

5.1.2 Airfoil and trailing edge models

A NACA 0015 airfoil with detachable Gurney flap sized 0%, 2%, 4% and 6% the chord length were designed and manufactured for the wind tunnel experiments. The airfoil have a chord length of $20cm$ and a span of $40cm$. The detachable trailing edge were made from plexiglass to allow the passage of laser light, by which means the velocity field on both pressure and suction side of the trailing edge can be captured simultaneously.

The 0% (or 'clean') and 6% Gurney flap (Figure 5.3) were chosen for this PIV-based noise investigation by evaluating the results of the previous study given by J.Shah. In addition, roughness elements (height around $0.841mm$) made of

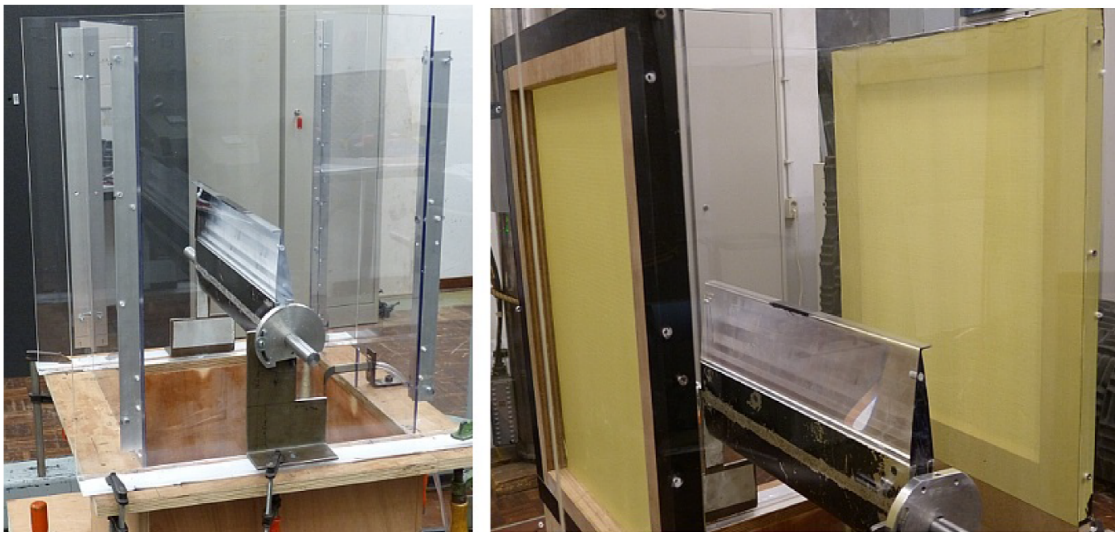

Figure 5.2: Test sections for stereoscopic PIV measurements(left) and synchronized acoustic-planar PIV measurements(right) designed by J.Shah [63]

carborundum grains were added at quarter-chord to trip the boundary layer. In such a way, at the trailing edge, on both sides of the airfoil, the boundary layer is turbulent. Until this point, the experimental conditions remain the same as those in reference [63].

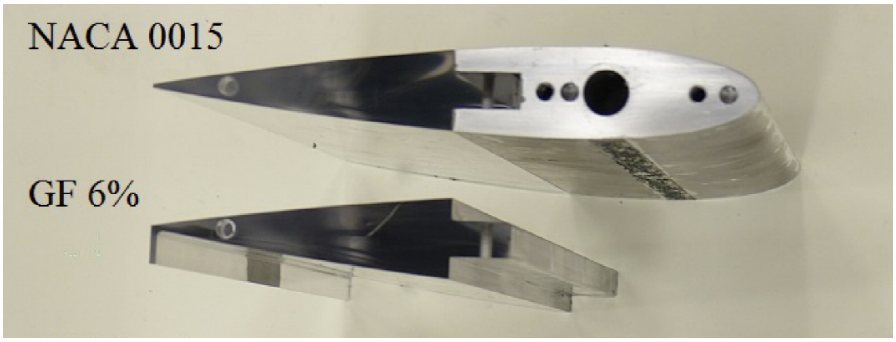

Figure 5.3: NACA 0015 and Gurney flap models designed by J.Shah [63] and manufactured at TU Delft

5.2 Experimental set-up for synchronized planar PIV and microphone measurements

The schematic diagrams showing the side view and top view of the synchronized planar PIV and microphone measurements set-up can be found respectively in Figure 5.5 and Figure 5.6. The measurements were taken for the NACA 0015 airfoil models with Gurney flap of height $0\%c$ and $6\%c$, with an incoming flow at velocity of $20m/s$, correspondingly, the chord Reynolds number Re_c of 2.7×10^5 and Mach number Ma_∞ of 0.059. The aim of the planar PIV measurements is to capture the flow patterns around and downstream the Gurney flap with high temporal and spatial resolution, the measurements of which can be used for the reconstruction of pressure in the flow field and the prediction of far-field noise.

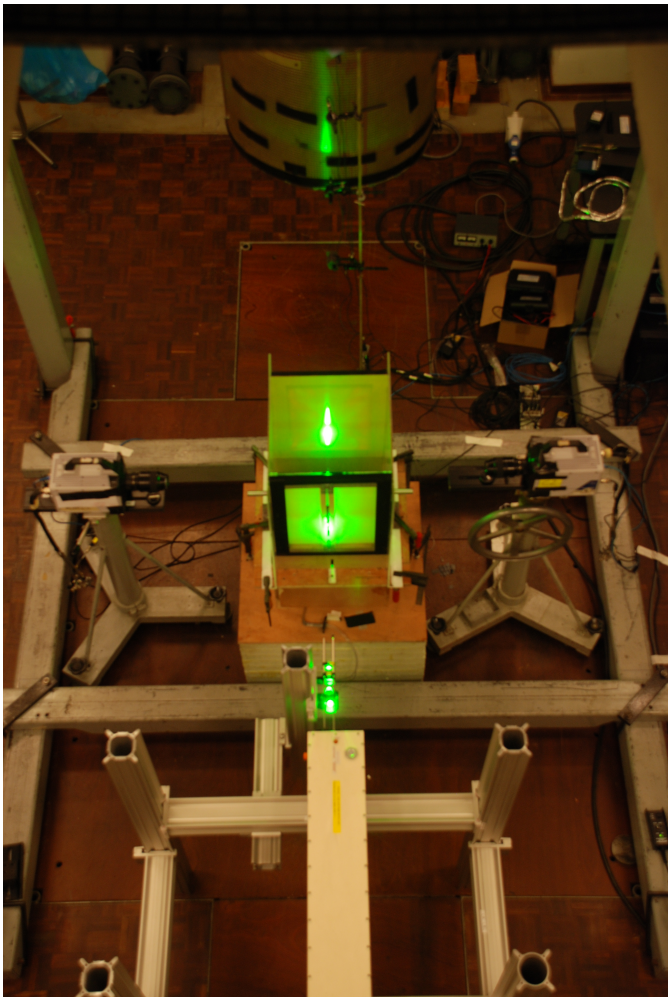

Figure 5.4: Photograph of the experimental set-up for synchronized planar PIV and microphone measurements

The NACA 0015 model was placed vertically in the wind tunnel with geometric angle of attack set to 4°. The laser light produced by the Nd:YLF laser was shaped in to a thin light sheet (thickness around $1mm$) and hit the location around the mid-span of the model to illuminate the field of view (FOV). For the reason of spatial resolution, two Photron Fastcam SA1.1 cameras with

CMOS sensors, placed facing each other on both sides of the test section, were used for image acquisition. The FOVs of the two cameras have an overlap of 25% (see Figure 5.7), which is used to stitch the two FOVs together in the procedure of image processing. For the concern of high temporal resolution, the sensors of the cameras were cropped to 704×704 to reach an acquisition frequency at $5kHz$. The flow is seeded with water-glycol based fog with size of particles $d_p \approx 1\mu m$.

PIV images are acquired in double frame mode at the acquisition frequency of

Parameter	Value	Unit
Airfoil chord length, c	20	cm
Gurney flap height, h	0(0%c, or clean), 12(6%c)	mm
Angle of attack, α	4	$^\circ$
Incoming flow velocity, V_∞	20	m/s
Incoming flow chord Reynolds number, Re_c	2.7×10^5	–
Incoming flow Mach number, Ma_∞	0.059	–

Table 5.1: Synchronized planar PIV and microphone measurement: experimental parameters

Illumination	Nd: YLF laser
Seeding	Water-glycol based fog
Cameras	Photron Fastcam SA1.1 with CMOS sensors
Microphone	Linear X-M53

Table 5.2: Synchronized planar PIV and microphone measurements: experimental devices

$5kHz$, with a delay between two frames of $50\mu s$. Detailed parameters of PIV recording can be found in Table 5.3.

Simultaneous velocity and acoustic measurements were performed since previous works (reference [63]) found the quality of causality correlation to be poor when velocity and acoustic measurements are not performed simultaneously. The two types of measurements can be synchronized by recording the trigger input of the CMOS cameras. Usually, the duration of microphone measurement is much longer than that of the PIV measurement and thus, the trigger input can be used to crop from microphone measurement the portion of recording that is simultaneous with

the PIV measurement.

The microphones should be placed in the far-field, which means the distance between the microphone and the source of sound (in this case can be assumed as the airfoil trailing edge) has to be larger than the wave length of the sound as well as two times the acoustic dimension (in this case, the chord length of the airfoil). The former was estimated as $0.85m$ according to the measurements in reference [63] and [64]. The latter is $0.4m$. For structural reasons in the laboratory, the distance between the airfoil trailing edge and the microphones was chosen as $1.3m$ in practice.

Parameter	Value	Unit
Field of View (FOV), for each camera	80×80	mm^2
Field of View (FOV), combined	80×140	mm^2
Sensor size	704×704	pixels
Magnification factor, M	0.176	–
Focal length, f	105 (both cameras)	mm
Numerical aperture, $f_\#$	2.8 (both cameras)	–
PIV acquisition frequency, f_s	5	kHz
Pulse separation, dt	50	μs
Particle image diameter,$d\tau$	4.278(0.21)[1]	μm $(pixels)$
Digital image resolution	8.8	$pixels/mm$
Recording mode	Double frame	–
Number of images, N	5773	–
Microphone placement (distance from the trailing edge)	1.3	m
Microphone acquisition frequency, f_{mic}	51.2	kHz

Table 5.3: Synchronized planar PIV and microphone measurements: recording parameters

[1] In experiments, cameras were slightly defocused to make the particle image larger such as to avoid peak-locking

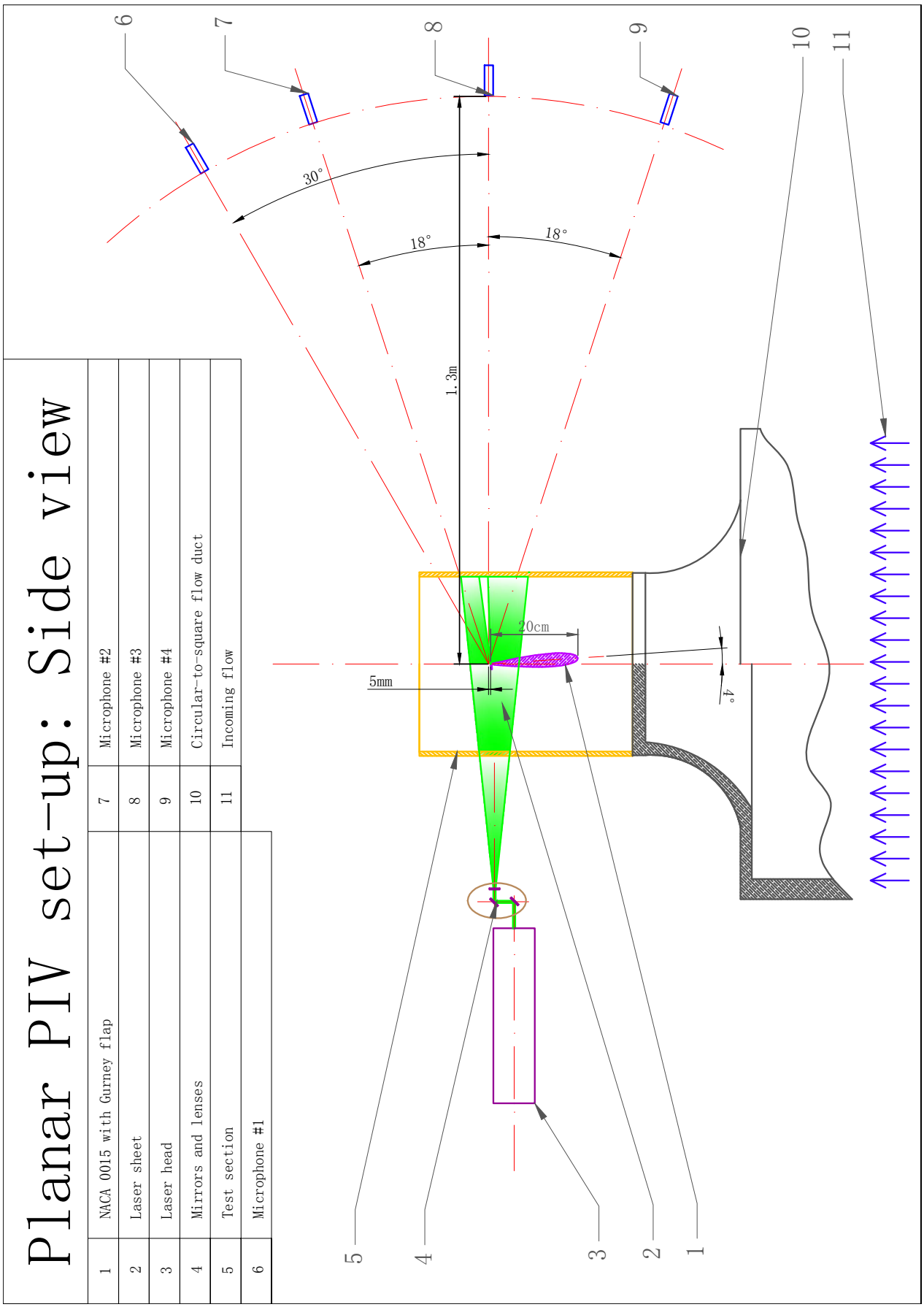

Figure 5.5: Schematic of set-up for synchronised planar PIV and microphone measurements(side view)

Planar PIV set-up: Top view

1	NACA 0015 with Gurney flap	5b	Test section: plexiglass
2	Laser sheet	6, 7, 8, 9	Microphone #1, 2, 3, 4
3	Laser head	12	Camera #1
4	Mirrors and lenses	13	Camera #2
5a	Test section: Kevlar		

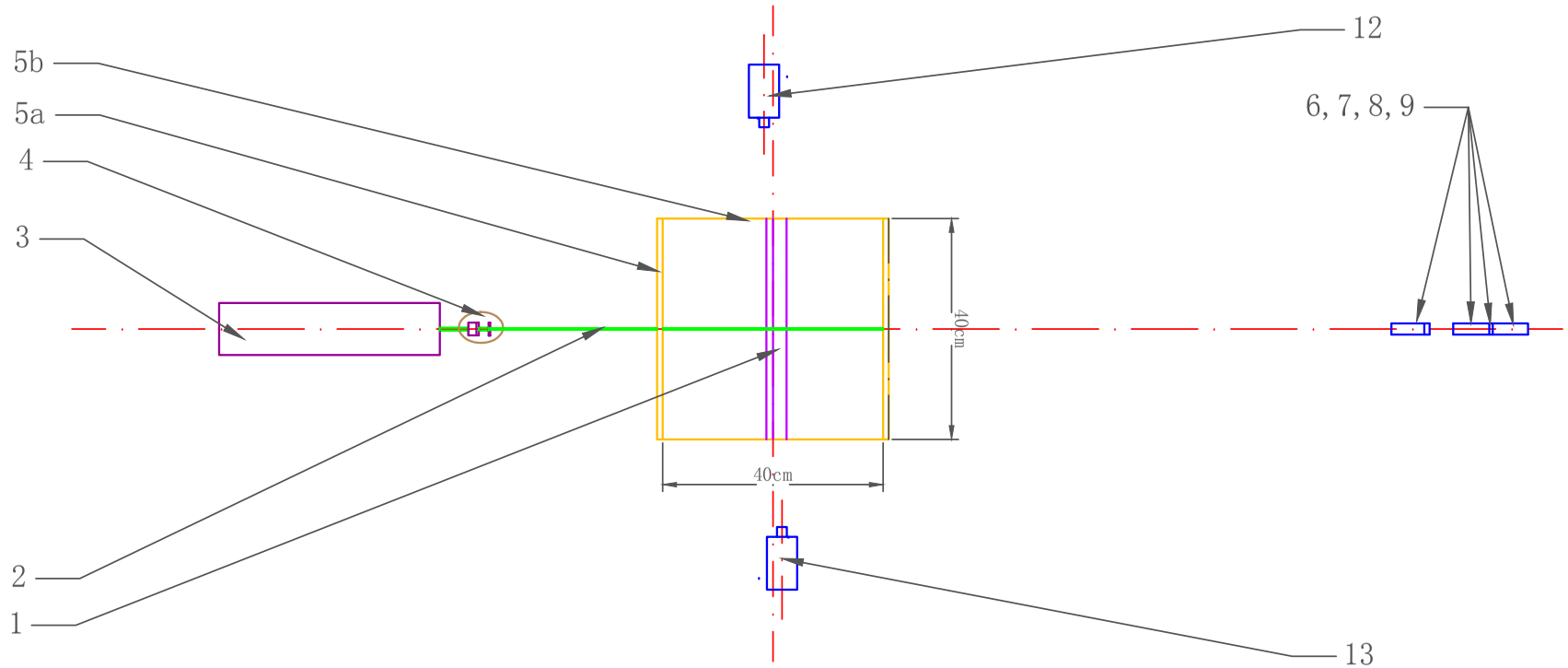

Figure 5.6: Schematic of set-up for synchronised planar PIV and microphone measurements(top view)

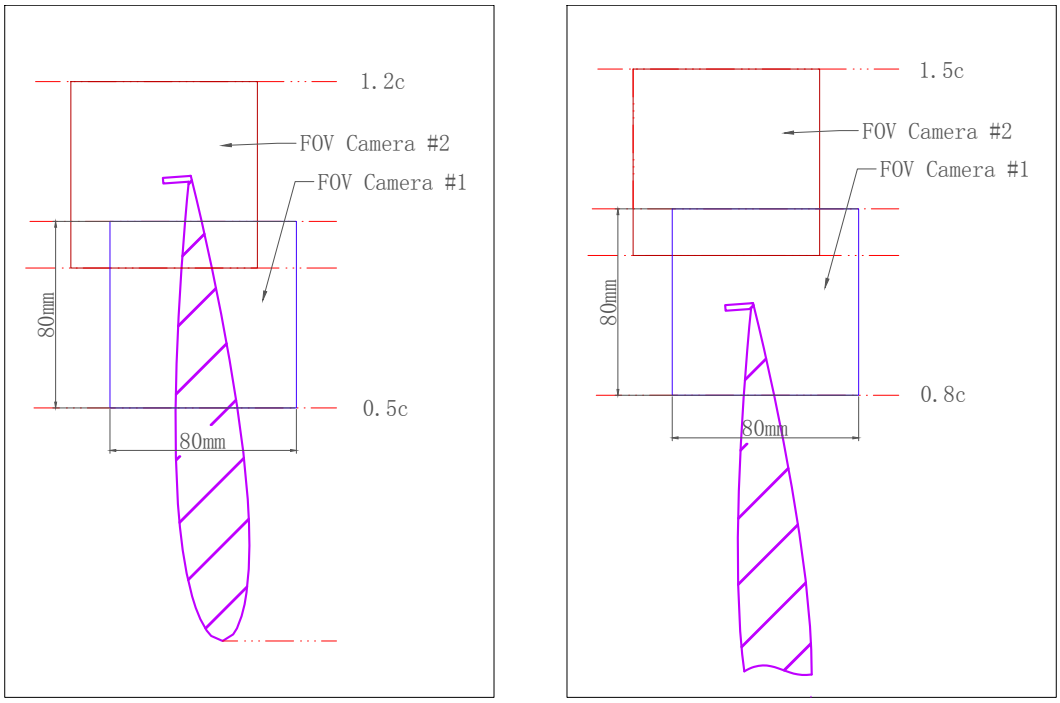

Figure 5.7: Two versions of Field of View for two-camera recording: FOV1(left) and FOV2(right)

5.3 Experimental set-up for stereoscopic PIV measurements

The experimental parameters and devices for the stereoscopic PIV measurements are identical as those applied for planar PIV measurements (refer to Table 5.1 and 5.2), except that the stereoscopic PIV measurements were not synchronised with acoustic measurements and therefore the microphones were not used.

The aim of stereoscopic measurements is to assess the spanwise coherence of the flow structures. The spanwise coherence can be used for the correction of 3D effect in noise generation, since noise predictions based on planar PIV measurements are essentially based on 2D assumptions.

In the stereoscopic PIV measurements, the sheet of laser sheet was placed normal to the free stream. The distance between the laser sheet and the Gurney flap is $15mm$, which is approximately one Gurney flap height downstream the Gurney flap. Velocity components of all three dimensions were captured, from which the spatial derivatives in the spanwise and transverse dimension can be resolved.
The front and top views of the set-up of the stereoscopic PIV measurements are illustrated in Figure 5.9. Detailed recording parameters of the PIV system can be found in Table 5.4.

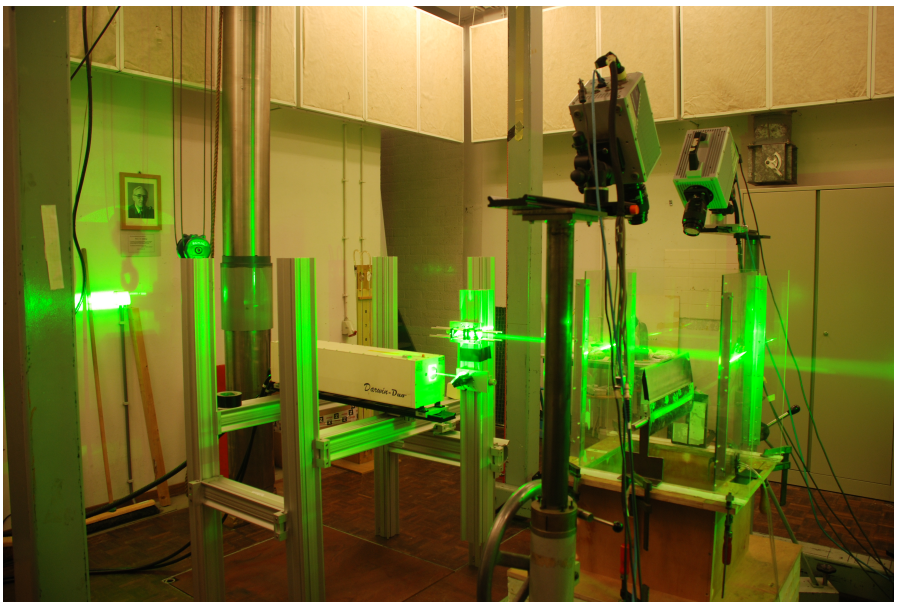

Figure 5.8: Photograph of the experimental set-up for stereoscopic PIV measurements

Parameter	Quantity	Unit
Field of View (FOV), for each camera	70×70	mm^2
Sensor size	704×704	pixels
Magnification factor, M	0.201	–
Laser sheet position (distance downstream the trailing edge)	15	mm
Focal length, f	105 (both cameras)	mm
Numerical aperture, $f_\#$	2.8 (both cameras)	–
PIV acquisition frequency, f_s	5	kHz
Pulse separation, dt	30, 35	μs
Recording mode	Double frame	–
Number of images, N	5773	–

Table 5.4: Stereoscopic PIV measurements: recording parameters

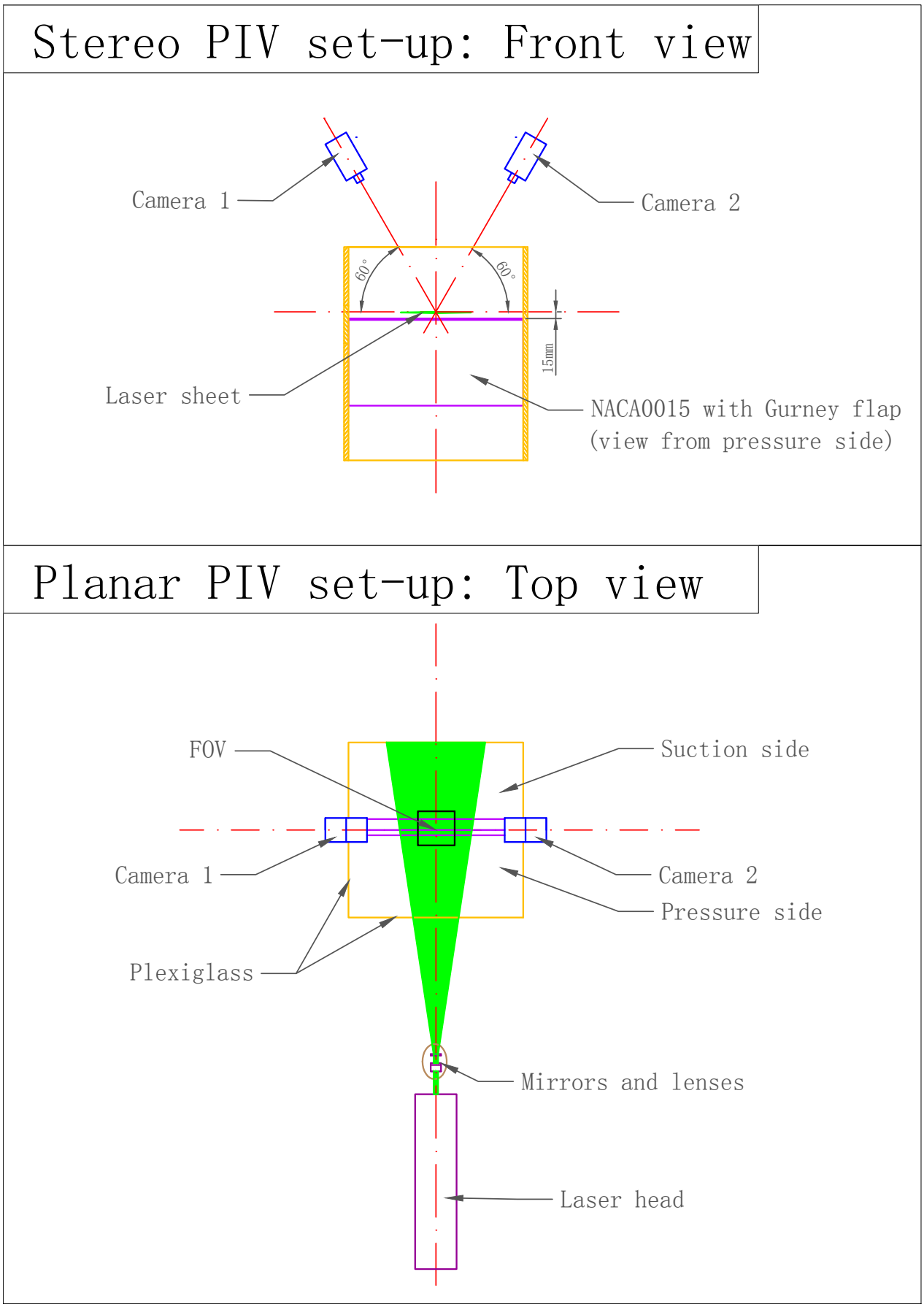

Figure 5.9: Schematic of set-up for stereoscopic PIV measurements

5.4 PIV image processing

DAVIS 8.2 provides various pre/post-processing techniques to retrieve the velocity field from PIV raw images. The following subsections offer a brief summary on the image processing procedures of planar and stereoscopic PIV measurements.

5.4.1 Planar PIV image processing

Pre-processing of the raw images lies in minimum intensity subtraction from the time series such as to remove the unwanted reflections. Sequential cross-correlation algorithm with multi-pass iterations of decreasing interrogation window sizes (from 64×64, 50% overlap, 2-pass, square-shaped window to 32×32 to 75% overlap, 3-pass, round-shaped window) is applied for vector field calculation.
Vector post-processing is applied to remove the outliers. The spurious velocity vectors are detected by means of the normalized median test that yields a 'universal' probability density function for the residual and hence a single threshold value can be applied to variety of flow conditions without *a priori* knowledge of the flow characteristics to detect spurious vectors. The method is developed by Westerweel and Scarano in 2005 [71]. The velocity fields evaluated by DAVIS 8.2 are shown in Figure 5.10.
To obtain the combined velocity field, the two velocity fields are first trimmed to remove the verge effect (measurements of poor quality at the verge of the camera sensor). The trimmed velocity fields are then concatenated with MATLAB programme, which detects the overlap region and averages the vector values given by the two vector fields. An example of the combined velocity field is given by Figure 5.11.

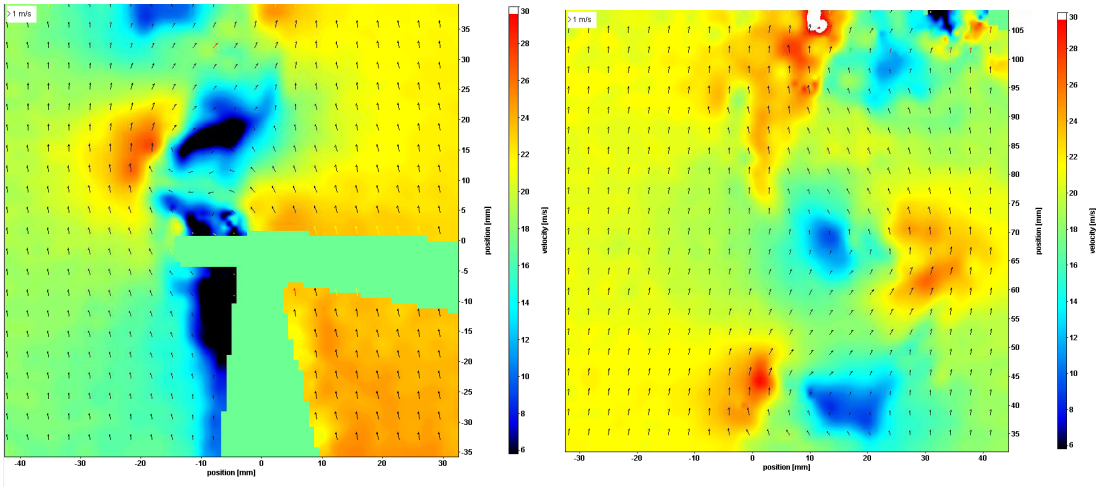

Figure 5.10: Velocity field obtained by camera 1(left) and camera 2(right)

5.4.2 Stereoscopic PIV image processing

The image processing of the stereoscopic PIV measurements basically follows the same procedures as that of the planar PIV, except that the cross-correlation algorithm applied should be stereo cross-correlation algorithm. In this study, the interrogation window size set for multi-pass iterations for stereoscopic PIV image processing is: 75% overlap, 2-pass, from 64×64 square-shaped to 16×16 round-shaped.

Correct calibration is essential for PIV velocity measurements. An additional step in calibration of stereoscopic PIV is referred to as the 'self-calibration', developed and validated by Wienke in 2005 [72]. Self-calibration involves computation of a disparity map based on the real particle images taken by camera 1 and 2 at the same time (in practice, very short pulse separation, e.g. $1\mu s$). The cross-correlation of the two images determines whether the calibration plate coincides with the light sheet. The true position of the light sheet and the mapping functions are then corrected according to the disparity vectors, and thus improve the calibration of the stereoscopic PIV.

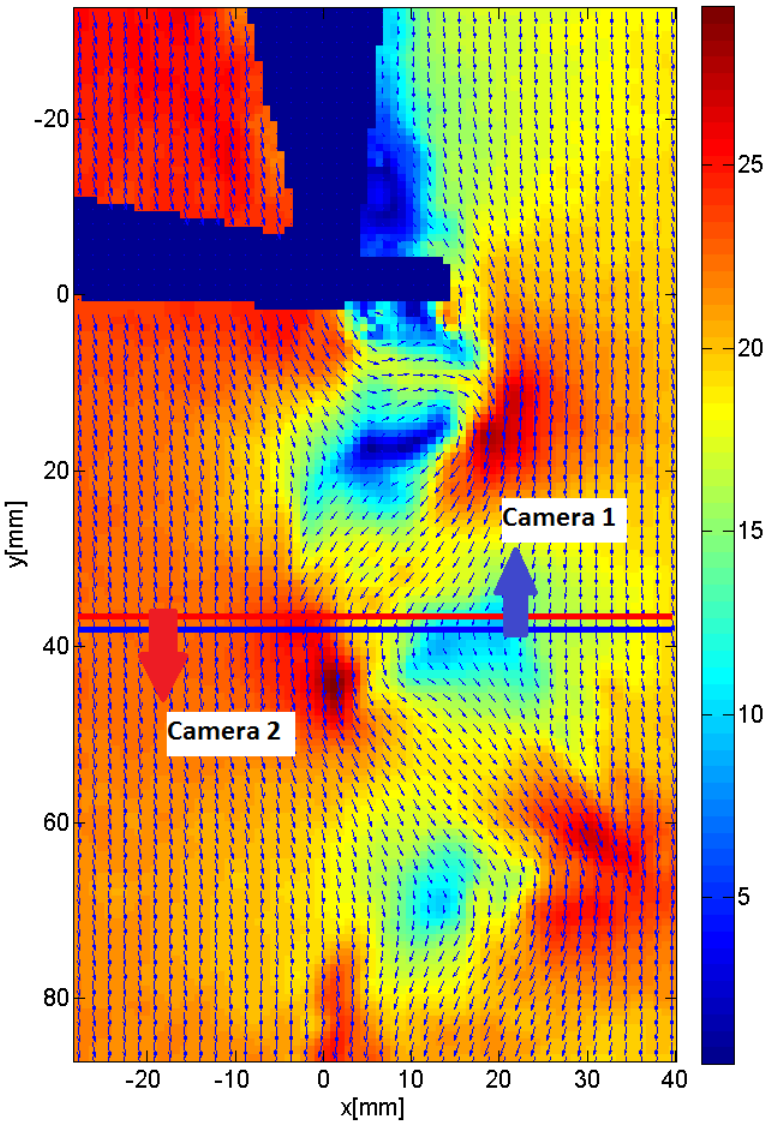

Figure 5.11: Combined velocity field from two-camera measurement

Chapter 6

Results and discussion

This chapter presents the results of the velocity measurements, acoustic measurements and the deducted far-field acoustics with the implementation of different formulation of the Curle's analogy. To start with, section 6.1 presented the velocity fields measured by the time-resolved planar PIV, from which, the pressure in the flow field is evaluated by in-plane Poisson solver. On the basis of evaluated pressure fields, in section 6.2, the far-field acoustic pressure is evaluated at each location of the four microphones with the distributed formulation of the Curle's analogy. The far-filed acoustic pressure is evaluated based on the PIV measurements obtained from both FOV 1 and FOV 2, and the results are compared. Section 6.3 continues with the far-field acoustic prediction, but with the lumped formulation of Curle's analogy. The section starts with the evaluation of aerodynamic loads. Thereafter, the lumped formulation is applied and the predictions are compared to the simultaneous microphone measurements both in time series and in power spectra. Finally, in section 6.4, the 2D acoustic predictions are corrected with the length of coherence in order to narrow the discrepancies between the PIV and microphone measurements.

6.1 Instantaneous velocity fields and reconstructed pressure fields

The velocity fields and reconstructed pressure fields presented in this section are retrieved from the PIV measurement at free stream velocity $V_\infty = 20m/s$ and with the field of view FOV 2 (see Figure 5.7).

6.1.1 Overall flow visualization

Previous study (reference [63], p.74) has shown that for airfoil with Gurney flap, the velocity fluctuation and the far-field microphone measurement share the same peak frequency on power spectra. Hence, the Kármán vortex shedding period $T_{shed} = 0.32ms$ can be evaluated from the peak frequency $314.9Hz$ in the power spectra of microphone measurement (see Figure 6.11, subsection 6.3.2).
The sequence of instantaneous snapshots of the transverse velocity (u-component) and the streamwise velocity (v-component) in one shedding period (0 to $0.32ms$) are presented respectively in Figure 6.1 and 6.2. The shadow region (as shown in Figure 5.11), which is caused by refraction of laser light when passing through the airfoil trailing edge, is filled with velocity values evaluated from nearest neighbour-interpolation. Such interpolation is justifiable for the following reasons:

- According to the experimental parameters for boundary layer characterization given in reference [63], measurement of flow in the boundary layer is beyond the resolution of the experimental set-up of the current study.
- Outside the boundary layer, the flow is essentially irrotational and effectively inviscid [1], and thus the relation between pressure and velocity is governed by Bernoulli equation.
- The Gurney flap moves the stagnation point downstream [69] and the spatial variation of pressure on the suction side is small within the last 3% of the trailing edge. Consequently, the spatial variation in velocity is expected to be small.

It can be observed from Figure 6.2 the velocity deficit in the wake region downstream the Gurney flap. The alternation of positive and negative transverse velocity (u-component) observed in Figure 6.1 indicates the existence of large vortical structures.
Correspondingly, the sequence of vorticity at the same time instants are shown in Figure 6.3, where red (counter-clockwise vorticity) and blue (clockwise vorticity) blobs indicate the counter-rotating vortices. The vortices shed at the trailing edge are conveyed downstream at an average spacing of $5cm$ with a velocity around $16.7m/s$, which is approximately 83% of the free stream velocity.

6.1.2 Pressure reconstruction

The in-plane pressure is reconstructed from the PIV measured velocity by Poisson solver as described in section 3.2 (Equation 3.12 and 3.13). As for the velocity measured by planar PIV, the spanwise velocity component is not measured and the flow is assumed as 2D flow. Consequently, the source term is reduced to:

$$f_{xy} = \left(\frac{\partial u}{\partial x}\right)^2 + 2\frac{\partial v}{\partial x}\frac{\partial u}{\partial y} + \left(\frac{\partial v}{\partial y}\right)^2 \tag{6.1}$$

As shown in Equation 6.1, the source term is a combination of spatial velocity gradients. However, the velocity gradients retrieved from planar PIV measurement in the region directly downstream the Gurney flap are unreliable due to the occurrence of high intensity 3D motion. Such velocity gradients can cause spurious oscillations in the solution and may spoil the whole pressure field. To avoid this problem, the velocity field is smoothed with the Gaussian kernel filter available in Matlab® , with standard deviation $\sigma = 10$ and window size [10 10].
To facilitate the explanation about the boundary conditions, the outer boundary of the domain is again divided into 'viscous region' and 'inviscid region' as in section 3.3. The criterion applied in this case is the local value of enstrophy, defined as:

$$\varepsilon = |\overrightarrow{\omega}|^2 \tag{6.2}$$

In this case, the threshold for viscous region is set as $\varepsilon > 1.5 \times 10^4 [Hz^2]$.
Dirichlet boundary condition is assigned to the inviscid region of the boundary, where pressure is calculated by Bernoulli equation:

$$p = P_\infty + \frac{1}{2}\rho V_\infty^2 - \frac{1}{2}\rho(u^2 + v^2) \tag{6.3}$$

Neumann boundary condition is assigned to the airfoil surface and to the viscous region of the outer boundary. The pressure gradient in the Neumann condition is defined as in Equation 3.10.
The sequence of instantaneous snapshots of pressure fields corresponding to the previously shown velocity and vorticity are presented in Figure 6.4. The pressure downstream the Gurney flap exhibits a coherence pattern as well as a distinguishable convection process as that exhibits by the vorticity. The locations of the local minima of the pressure coincide with the locations of the cores of vortices as shown in Figure 6.3, while the local maxima indicate the stagnation region caused by flow impinging the solid surface (upstream the Gurney flap) or the interaction of the vortices (downstream the Gurney flap).

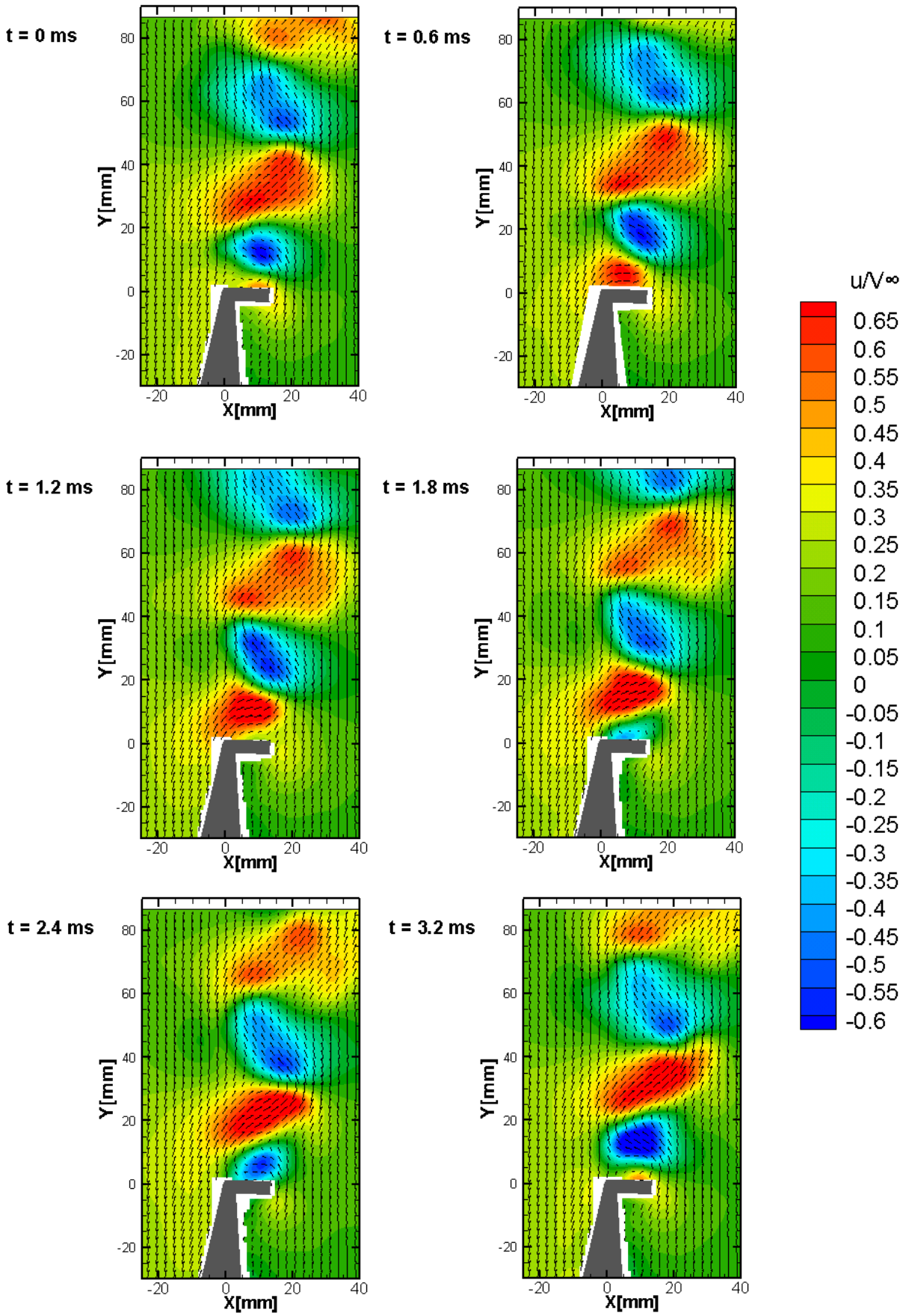

Figure 6.1: Non-dimensionalized instantaneous transverse velocity (u-component) at different time instant: GF6-AOA4-V20-FOV2

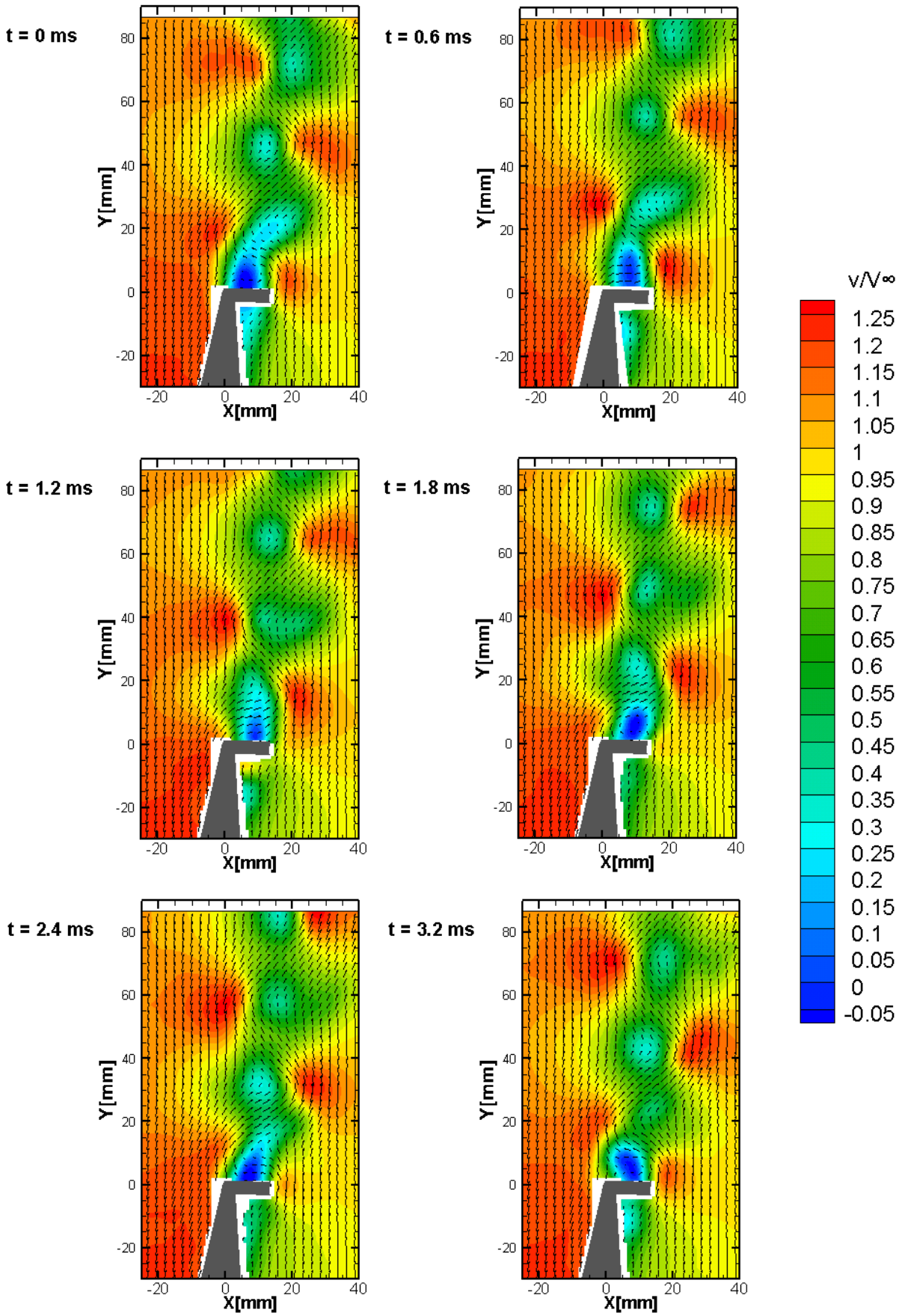

Figure 6.2: Non-dimensionalized instantaneous streamwise velocity (v-component) at different time instant: GF6-AOA4-V20-FOV2

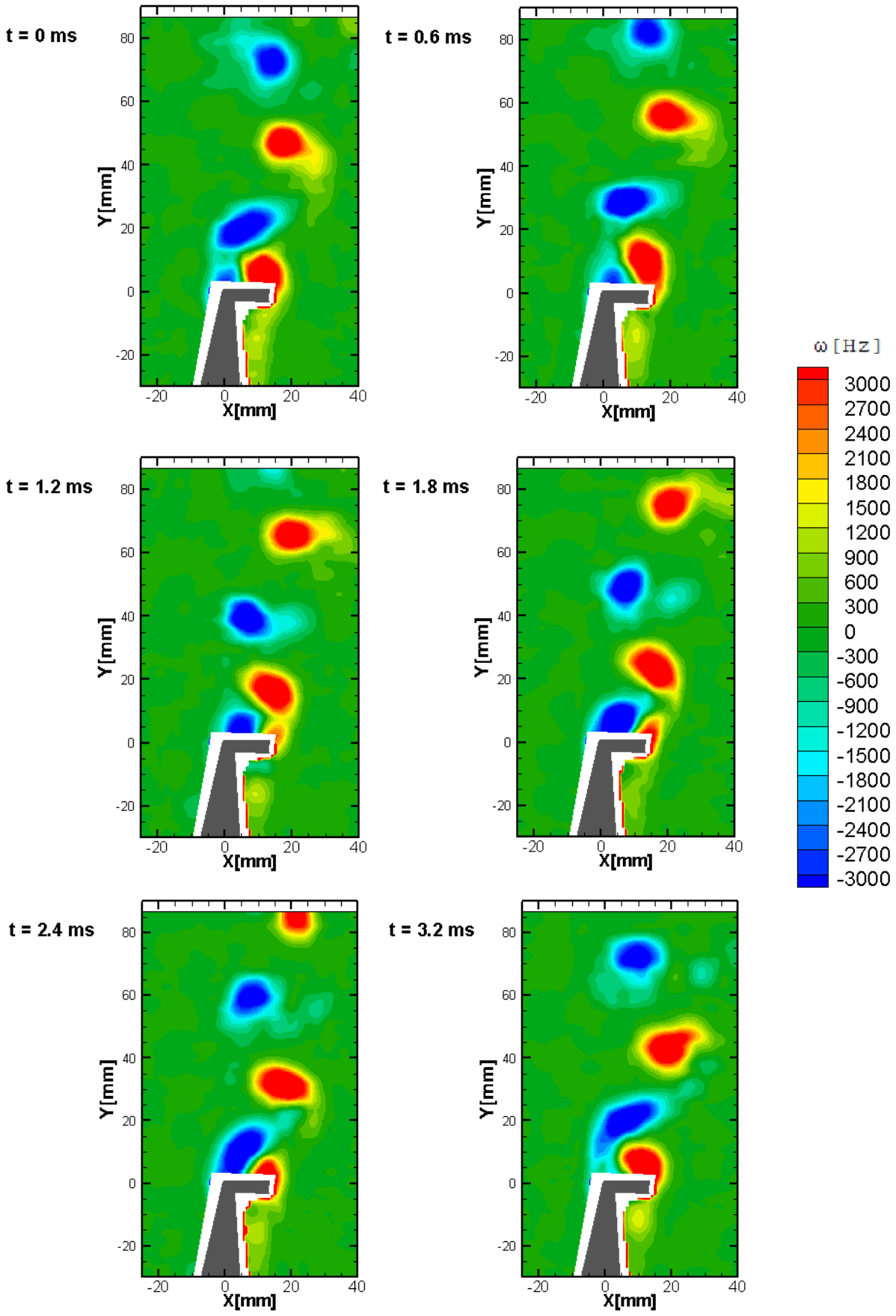

Figure 6.3: Instantaneous vorticity at different time instant: GF6-AOA4-V20-FOV2

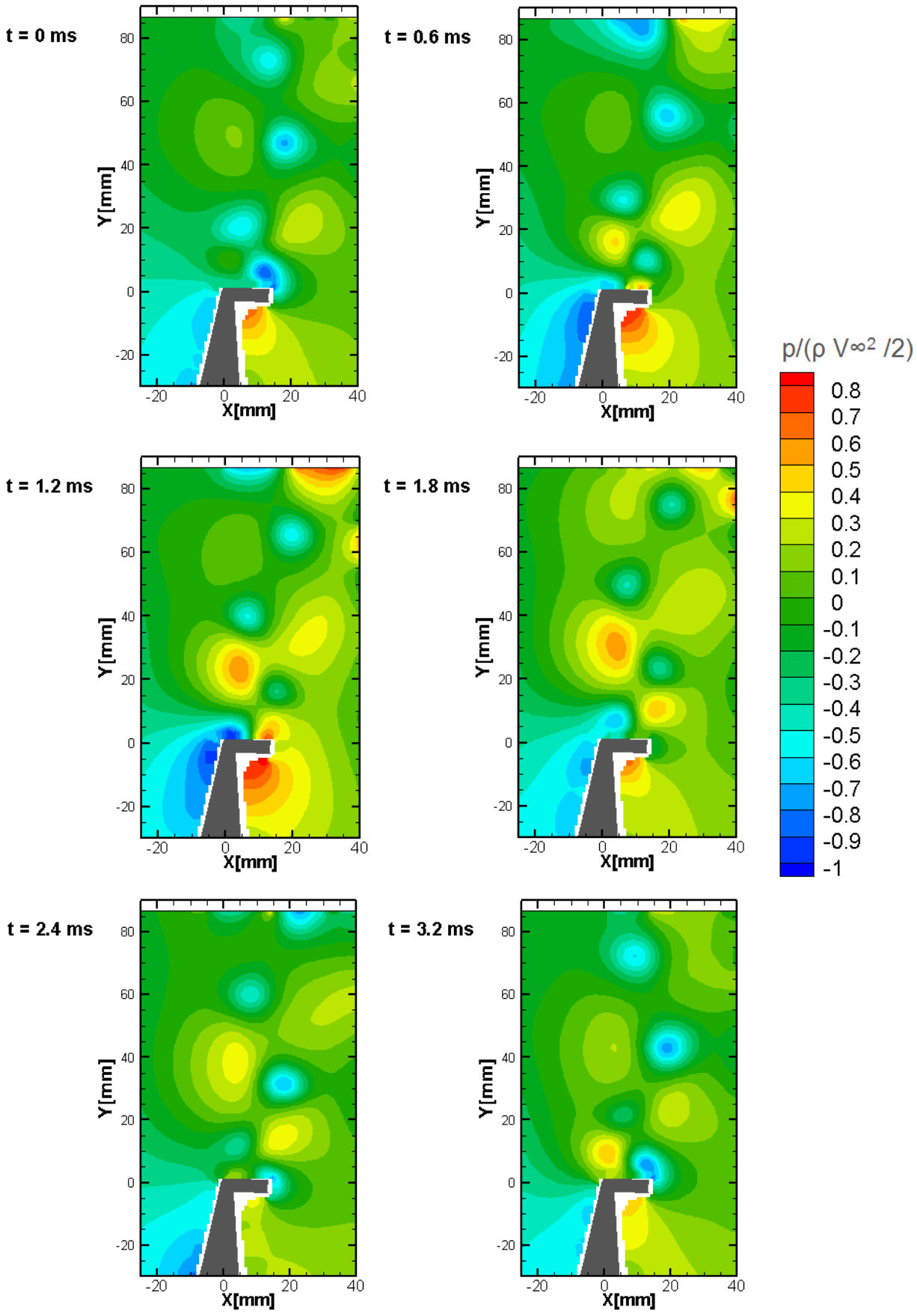

Figure 6.4: Reconstructed pressure (non-dimensionalised by free stream dynamic pressure) at different time instant: GF6-AOA4-V20-FOV2

6.2 Acoustic prediction based on the distributed formulation of the Curle's analogy

This section presents the results of acoustic prediction obtained by the implementation of the distributed formulation of the Curle's analogy (Equation 2.19), based on the PIV measurements performed on both FOV 2 (more information downstream of the Gurney flap) and FOV 1 (more information upstream of the Gurney flap). Comparison between the two aeroacoustic computations as well as to the far-field microphone measurements are presented in power spectra of $2.4Hz$ resolution.

6.2.1 Prediction of the far-field acoustic pressure based on velocity measurements with FOV 2

As shown in Equation 2.19, the pressure fluctuation at the location of listener (or microphone) is the sum of influence received at time instant t by the listener and emitted at (different) retarded time instant(s) t_e by the sources. Therefore, information about the retarded time for each source location is required before summing up the influence of sources at the location of listener.
Since both the listener and the sources are fixed in this case, the value $t-t_e = r/c_0$ is a constant value for a certain source with respect to a certain listener. The values of $t - te$ of this case are evaluated for the solid surface locations within the PIV field of view and are summarized in Table 6.1.

Listener	min.$(t-t_e)[ms]$	max.$(t-t_e)[ms]$	mean.$(t-t_e)[ms]$	max.$(\Delta(t-t_e))[ms]$
Microphone 1	4.3	4.4	4.4	0.1
Microphone 2	4.0	4.0	4.0	0
Microphone 3	3.8	3.9	3.8	0.1
Microphone 4	3.9	4.0	4.0	0.1

Table 6.1: Value of $t - t_e$ for microphones with respect to the sources distributed on the airfoil surface

It can be observed that the largest difference in retarded time is $0.1ms$ along the surface of airfoil. Under the sampling rate of the current study ($5000Hz$), the time interval between two snapshots of velocity field is $0.2ms$. For the source locations with a different retarded time from the mean value, the treatment can either be interpolation of the local time series of pressure to obtain the value in between the two snapshots, or approximating with the value of the nearest snapshot in time.
With further observation of the mean value of $(t - t_e)$, it can be inferred that source locations with a value of $(t - t_e)$ different from the mean value only account a small portion of airfoil surface. Concerning the simplicity of application, each microphone is assigned with the respective mean value of $(t - t_e)$ for the calculation of retarded time. The observation of retarded time inversely testifies that the experimental set-up for the current study satisfies the compact source assumption as described in section 2.4.
The resulting power spectra of the acoustic prediction based on the PIV measurement on FOV 2 are presented in Figure 6.6 (blue curve). As comparison, the measurements by corresponding microphones are plotted on the same schematic (red curve).
The spectra of microphone measurements and the acoustic prediction all feature a local peak at $315Hz$ in correspondence to the vortex shedding frequency, with the drift of peak frequency no more than $10Hz$. The first harmonic $630Hz$ can be observed but not obvious for microphone measurements, yet it is more remarkable on the spectra predicted from PIV measurement. The noise level at the peak frequency is slightly over-estimated by PIV measurement for listener locations at microphone 1, 2 and 3. The over-estimation of noise level can be attributed to the 2D flow assumption, or full spanwise coherence assumption. However, the over-estimation in noise level is not observed for microphone 4. Thus, the full spanwise coherence assumption is only one (though important) of the factors that may influence the prediction of noise level. In other words, the extent of over-estimation in noise level should be larger if the full coherence assumption is the only contributing factor. The reduce in estimated noise level can possibly be ascribed to:

- The omission of velocity/pressure fluctuations on the airfoil surface upstream the FOV 2.

- The damping of fluctuation amplitude due to smoothing of velocity field.

To reduce the influence of the above mentioned two factors, one can either move the field of view upstream, or avoid the smoothing of velocity field by applying the lumped formulation of Curle's analogy. The viability of the two options is discussed respectively in subsection 6.2.2 and section 6.3.
Less agreement between the PIV prediction and the microphone measurements is retrieved in broadband components. The microphone spectra feature a rise in amplitude in frequency range below $100Hz$. The low frequency components in the microphone spectra have been shown to be caused by the wind tunnel operation noise, concluded from the preliminary background measurements and the measurements on the airfoil model without Gurney flap (Figure 6.11,green curve). Self-evidently, the background noise of wind tunnel operation cannot be revealed by acoustic computation based on velocity measurements.
The sharp decay in magnitude observed at $1445Hz$ in Figure 6.6 has no physical meaning. The artificial magnitude reduction is mainly due to the numerical smoothing of the signal in the calculation of the time derivatives. Comparison of the effect of the discrete method used for time derivatives was presented by Lorenzoni (2008)[44], suggesting that the central scheme (which is applied in the present study) is more effective in magnitude reduction since a wider kernel is used for the computation of the differences.
The amplitude of computed acoustic spectra does not decay in the high frequency range as in the spectra of microphone measurements since the high frequency components are more susceptible to experimental and numerical noise which can be attributed to:

- The effect of 3D motion with high intensity directly downstream the Gurney flap.

- Inaccuracy of the experimental data.

- Energy fold-back due to finite sampling frequency.

6.2.2 Prediction of the far-field acoustic pressure based on velocity measurements with FOV 1

As mentioned in subsection 6.2.1, the omission of velocity/pressure fluctuations upstream the FOV 2 may influence the predicted noise level. This subsection presents the effect on noise prediction when moving the PIV field of view more upstream.

The velocity field measured by PIV on FOV 1 is again smoothed with the Gaussian kernel filter as for the case of FOV 2 , with standard deviation $\sigma = 10$ and window size [10 10]. However, in this case, the threshold for viscous region is set as $\varepsilon > 2 \times 10^6 Hz^2$. The reason for increasing the threshold is to guarantee sufficient Dirichlet boundary such as to prevent the numerical instabilities of the system. Otherwise, since the downstream edge of the physical domain is too close to the Gurney flap, the local enstrophy is too high to allow any Dirichlet boundary condition on this edge. Example snapshots of the velocity, vorticity and reconstructed pressure at the same time instant are presented in Figure 6.5.

The resulting power spectra of the acoustic prediction based on the PIV measurement on FOV 1 are presented in Figure 6.6 (green curve). Instead of yielding a higher noise level than the prediction made from FOV 2, the noise level predicted from FOV 1 is lower. This reduction in amplitude of pressure fluctuation can be attributed to the deliberate increase in the threshold of 'viscous region'. The extra Dirichlet boundary condition assigned to the outer boundary while stabilizes the solution, also exerts damping effect on the fluctuation.

It can be observed that moving the PIV field of view upstream while maintaining the spatial resolution (and hence the size of the field of view) is not preferable for pressure reconstruction, since the downstream edge the physical domain is submerged in the near-wake of the Gurney flap, the condition of which incommodes the choice of boundary conditions and exacerbates the stability of Poisson solver.

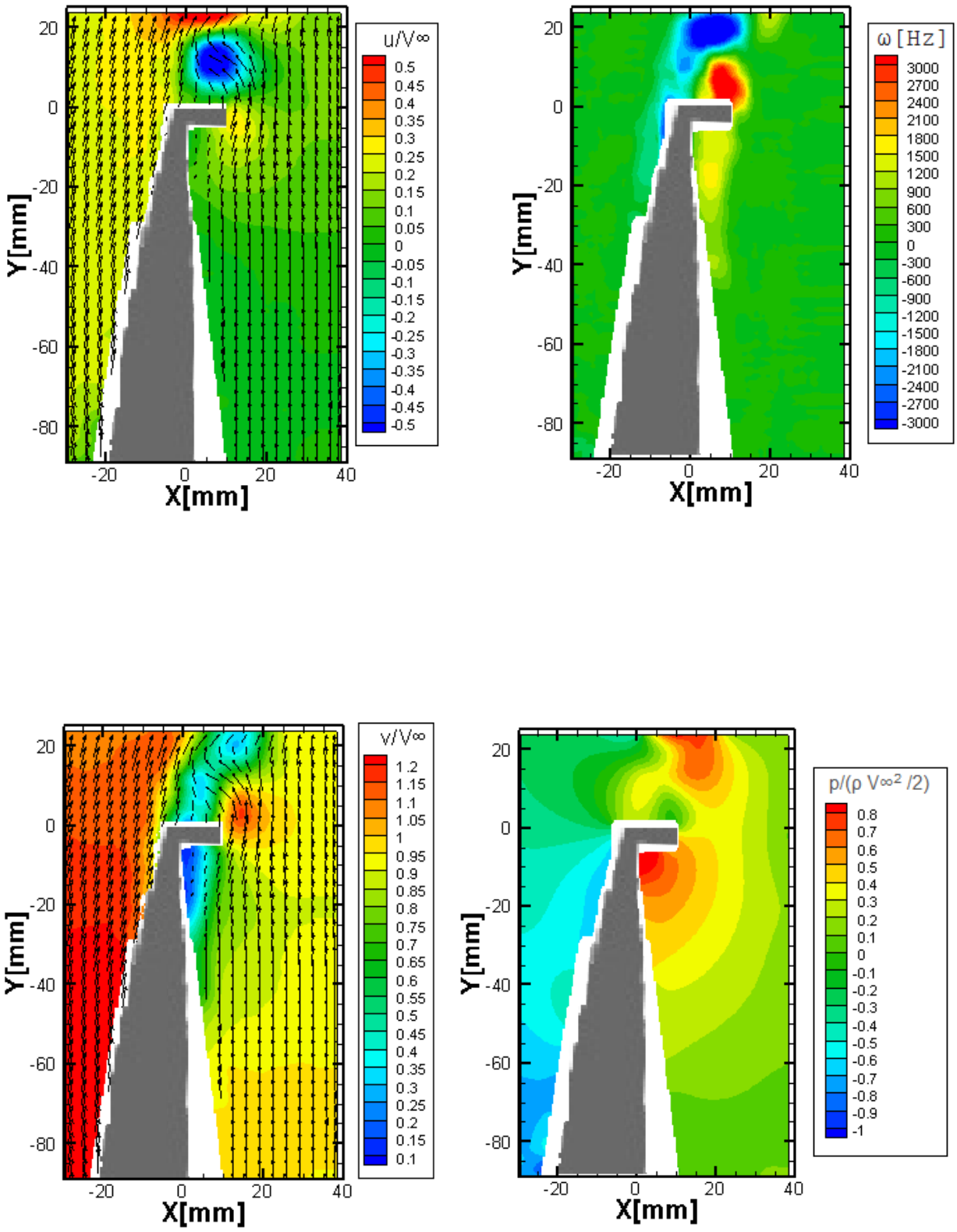

Figure 6.5: A snapshot of the instantaneous transverse velocity, streamwise velocity, vorticity and pressure evaluated from GF6-AOA4-V20-FOV1

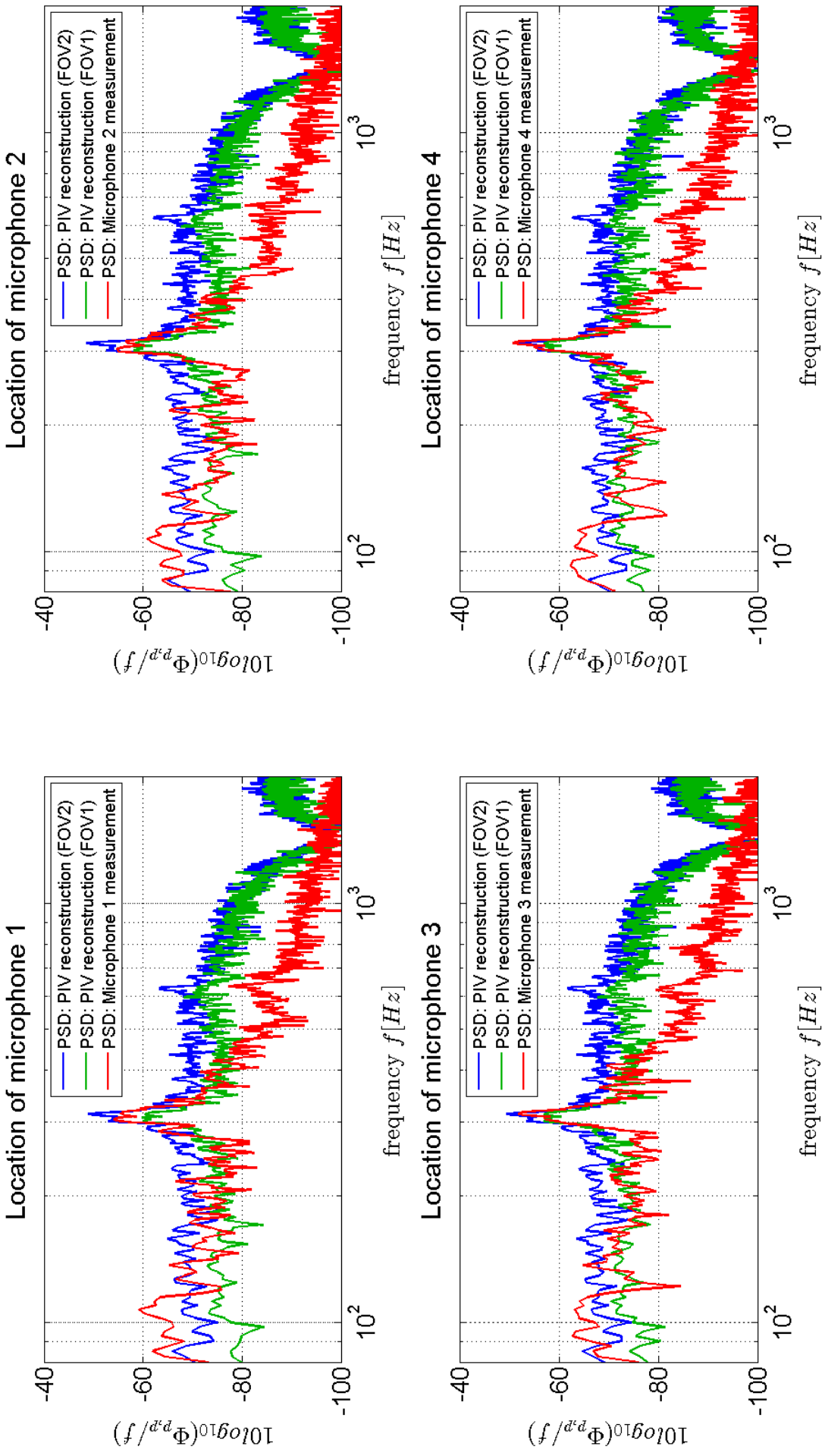

Figure 6.6: Power spectra ($\Delta f = 2.4Hz$) of far-field acoustic pressure evaluated by distributed formulation of Curle's analogy from PIV measurement (GF6-AOA4-V20-FOV2) and (GF6-AOA4-V20-FOV2) based on full span coherence assumption in comparison with the simultaneous microphone measurement at the same location

6.3 Acoustic prediction based on the lumped formulation of the Curle's analogy

As discussed in section 6.2, due to the damping effect of velocity fields smoothing as treatments for PIV measurements noise and the local 3D motions, the far-field noise level is unavoidably under-estimated by the distributed formulation of Curle's acoustic analogy with the pressure field reconstructed by Poisson solver. To circumvent the above-mentioned issues, given that the source of sound has been proved to be compact under the experimental set-up of this study, in this section, the acoustic prediction results from the implementation of the lumped formulation of the Curle's analogy (Equation 2.20) are presented.

6.3.1 Evaluation of aerodynamic forces with FOV 2

The first step towards the application of Equation 2.20 is the evaluation of aerodynamic loads of the airfoil. The velocity measurement on FOV 2 is chosen since the outer boundaries of the control volume should preferably be away from the airfoil surface to avoid the influence of local 3D motions on the reconstructed pressure.
Lift and drag of the airfoil model are estimated with the momentum balance equation (Equation 3.15). The pressure in the momentum balance is evaluated by the method proposed by Kurtulus et al. (2007) as described in section 3.3. In this case, the threshold for viscous region is set as $\varepsilon > 1.5 \times 10^4 Hz^2$ as in subsection 6.2.1.
The excerpts of lift and drag in time series are plotted respectively in Figure 6.7 and 6.8, with the aerodynamic loads plotted in black and the first, second and third term in Equation 3.15 plotted respectively in green, blue and red. The plots also show the mean value of the aerodynamic loads, plotted in magenta.

Periodicity can be observed in the reconstructed aerodynamic loads and the components. For lift, the fluctuations are majorly attributed to the volume integral

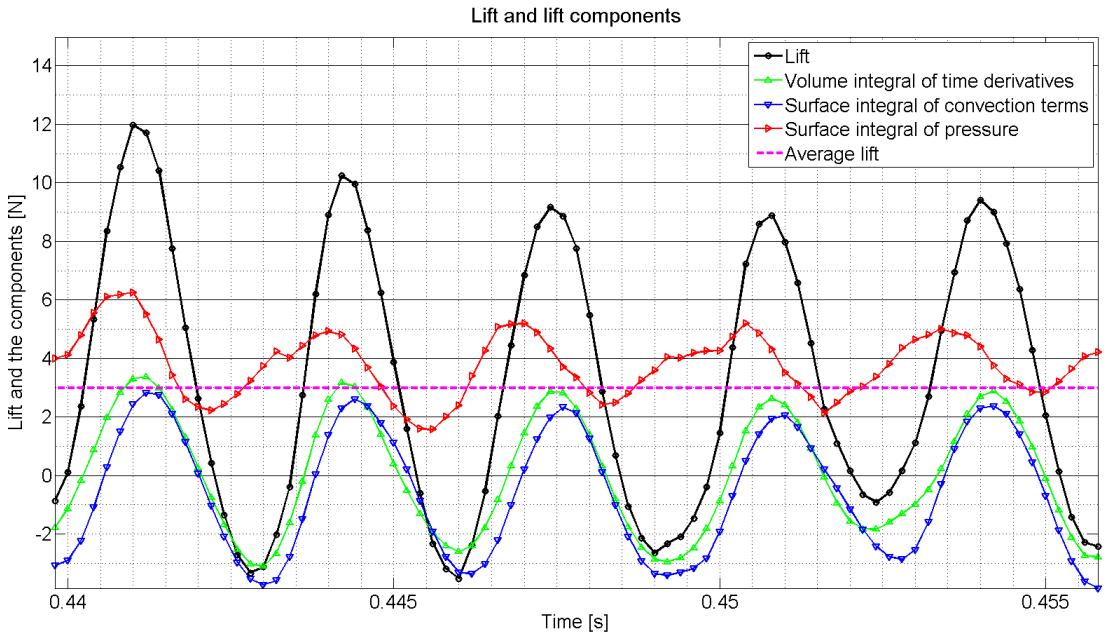

Figure 6.7: An excerpt of time history of lift and the components of lift evaluated from PIV measurement:GF6-AOA4-V20-FOV2

of the time derivatives of the velocity and the surface integral of the convection, while for drag, the major components of fluctuations are the two surface integral terms. However, it would be arbitrary to neglect any of the three components in both lift and drag, when looking closely at the order of magnitude and considering their contribution to the phase of the overall fluctuation.
The resulting power spectra of the aerodynamic loads evaluated from the PIV measurement on FOV 2 are presented in Figure 6.9. Both the lift and the drag peak at the frequency of $314.9Hz$, which is consistent with the shedding frequency.

6.3.2 Prediction of the far-field acoustic pressure with FOV 2

Based on the aerodynamic loads evaluated from the PIV measurement, Equation 2.20 is implemented to reconstruct the far-field acoustic pressure. The distance

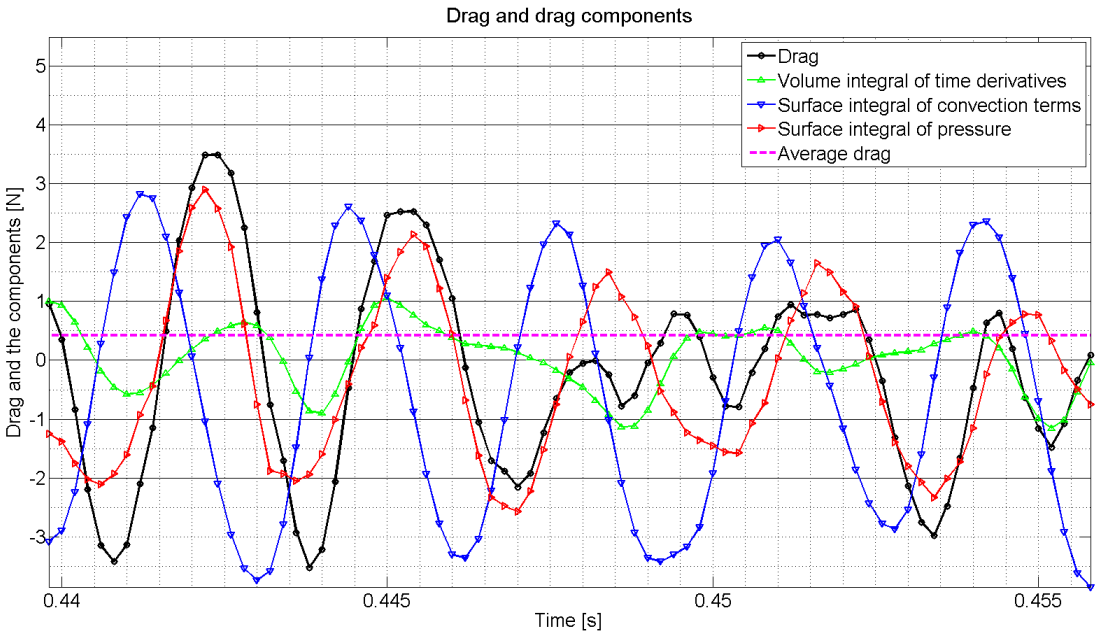

Figure 6.8: An excerpt of time history of drag and the components of drag evaluated from PIV measurement:GF6-AOA4-V20-FOV2

from the airfoil trailing edge and the certain microphone is used to calculate the uniform retarded time for that specified microphone. The values of $t - t_e$ of the microphones coincide with the average values listed in Table 6.1.

The excerpts of the far-field acoustic pressure in time series, both the microphone measurements and the reconstruction from PIV measurements based on full spanwise coherence assumption are shown in Figure 6.10. The two measurements roughly share the same period and phase. However, due to the many stages in between, such as the smoothing of velocity fields, the computation of time and spatial derivatives and the acoustic analogy, the maximum coefficients obtained from the cross-correlation of the far-field pressure measured by microphone and that evaluated by PIV is barely 0.19.

As expected, the amplitude predicted by PIV measurements is larger than that measured by the microphones at all four locations of microphones, since in reality the flow is intrinsically 3D and the spanwise coherence length is shorter than the span.

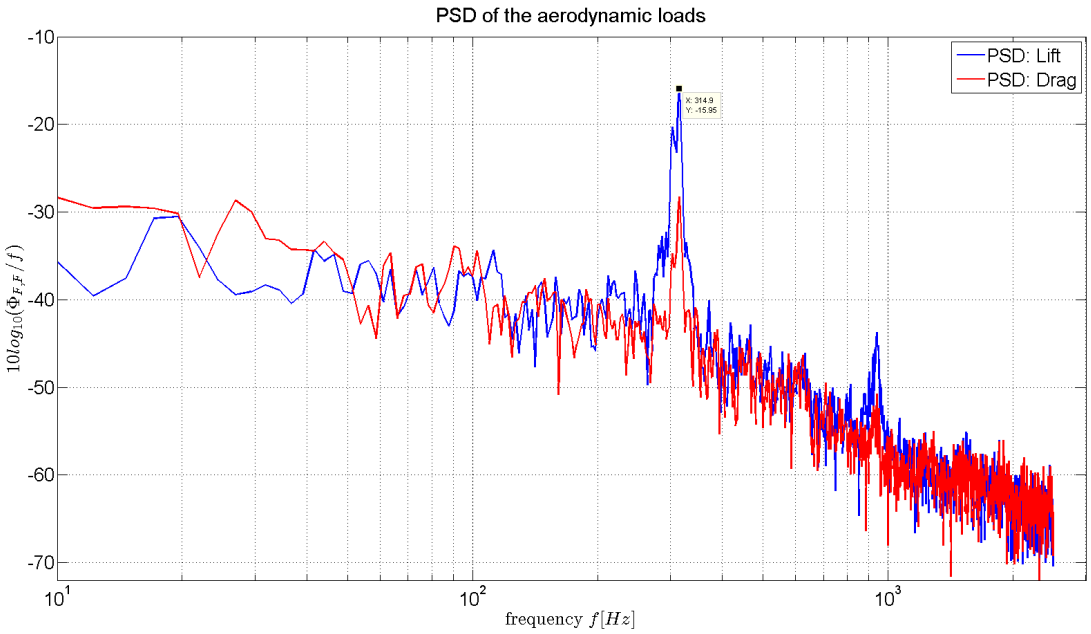

Figure 6.9: Power spectra ($\Delta f = 2.4Hz$) of lift and drag evaluated from PIV measurement:GF6-AOA4-V20-FOV2

Figure 6.11 shows the power spectra of the far-field acoustic pressure. The blue curve and the red curve show respectively the predictions of PIV and the measurements of microphones, and both peak at frequency around $315Hz$, which has been observed in the power spectra of the prediction given by distributed form of Curle's analogy (Figure 6.6) and is consistent with the peak frequency of aerodynamic loads. The latter consistency is expected, since at the Mach number of the current study ($Ma_\infty = 0.059$), the Doppler effect is negligible, the frequency reaching the receiver should be equal to the frequency emitted by the source.
The extra green curve in Figure 6.11 offers a comparison of the power spectra of the clean NACA 0015 (microphone recordings performed at same locations), which consists of only broadband components. The absence of frequency peak on the clean NACA 0015 power spectra serves as a side proof that the tonal noise generated by the model with Gurney flap should be attributed to the presence of the Gurney flap.

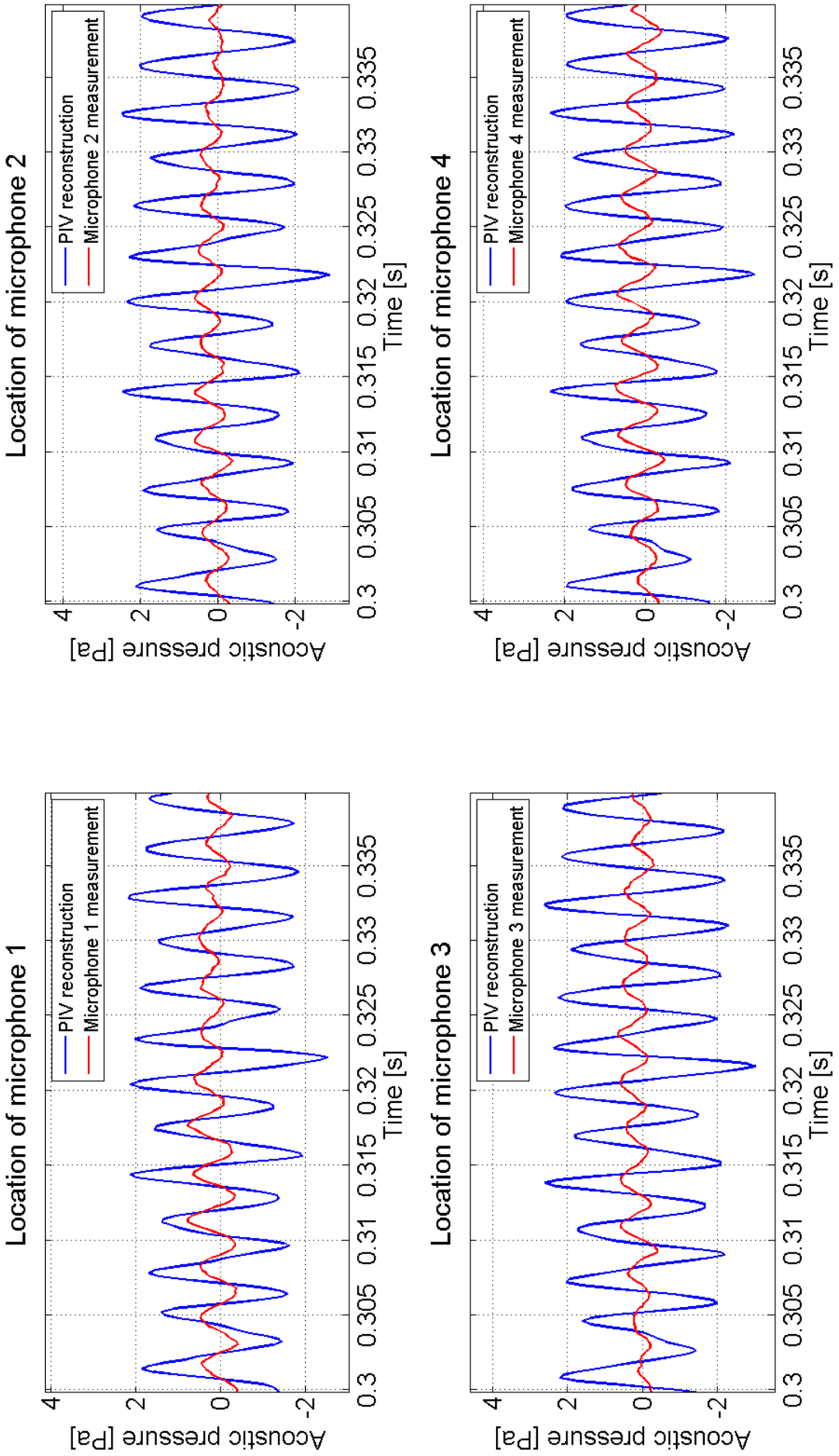

Figure 6.10: An excerpt of time history of far-field acoustic pressure evaluated by lumped formulation of Curle's analogy based on full span coherence assumption from PIV measurement (GF6-AOA4-V20-FOV2) in comparison with the simultaneous microphone measurement at the same location

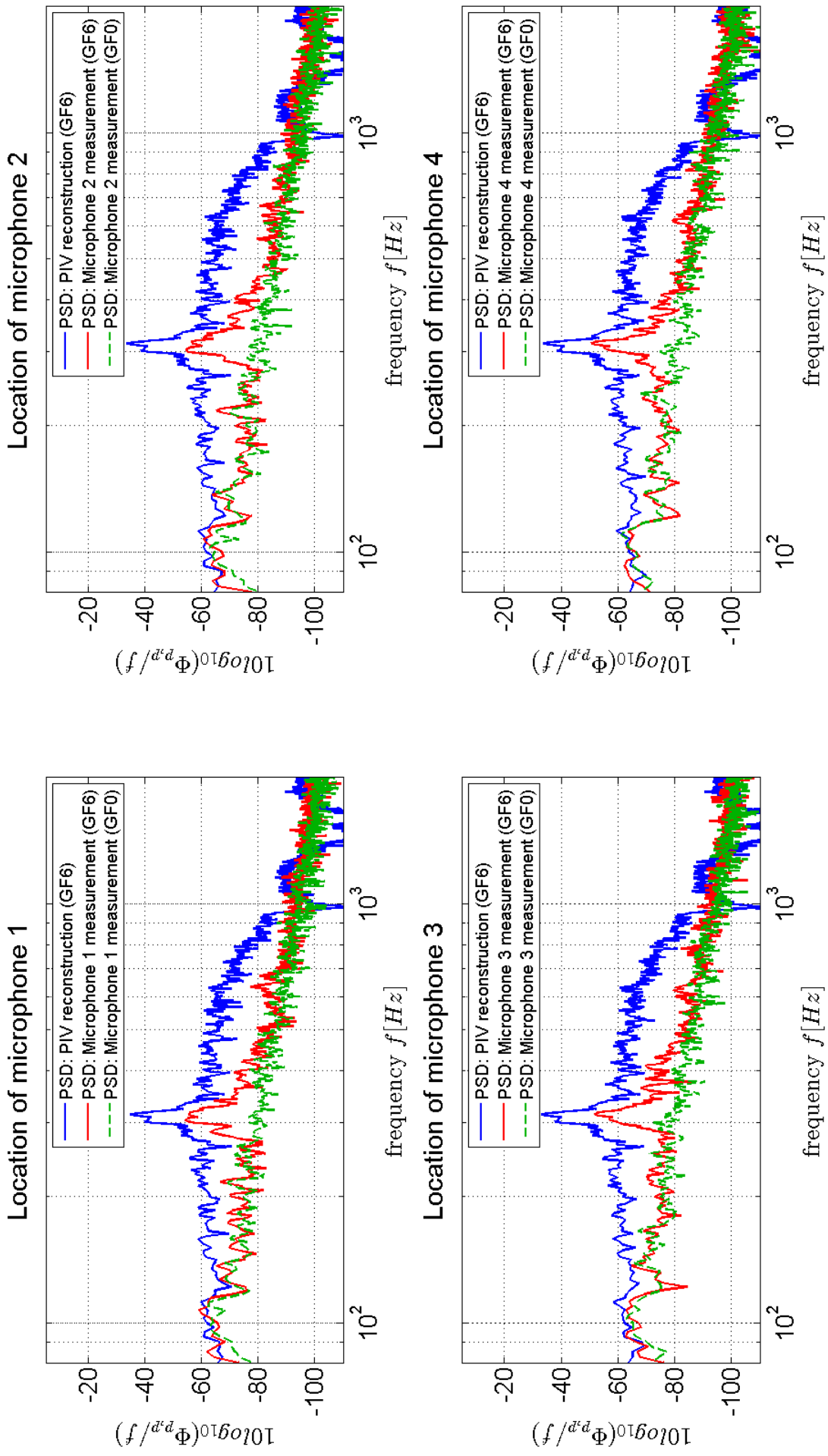

Figure 6.11: Power spectra ($\Delta f = 2.4Hz$) of far-field acoustic pressure evaluated by lumped formulation of Curle's analogy based on full span coherence assumption from PIV measurement (GF6-AOA4-V20-FOV2) in comparison with the simultaneous microphone measurement at the same location on GF6 and GF0 model.

6.4 Correction of acoustic prediction based on length of coherence

It can be observed from Figure 6.6 and Figure 6.11 that, based on the full spanwise coherence assumption, where the intensity and phase of the fluctuations are presumably the same along the span, the PIV measurements over-estimate the far-field acoustic pressure. In fact, it is reasonable to assume the intensity of the fluctuation to be uniform along the span except for the region close to the test section walls where horse shoe vortex develops. However, the assumption of uniform phase angle along the span could be the dominating factor leading to the overprediction as much as $20dB$ in the frequency range of lumped formulation of the Curle's analogy.
Since the planar PIV measurements only offers the intensity and phase information at the location of the thin light sheet, assumptions should be made on the pressure fluctuations out of the measuring plane. The coherence function (as introduced in subsection 3.1.3) provides a good measure of the dependency of the average phase angle at two locations. An equivalent coherence length can be defined by choosing a critical value for the coherence function. When the value of the coherence function is above the chosen critical value, the fluctuation can be regarded as in the same phase, and otherwise, the phase angle is completely independent.
The method is originally proposed by Kato et al.[35] and is proven to work reasonably well by literatures such as [43], [51] and [56].

6.4.1 Calculation of spanwise coherence length

The measurements by the stereoscopic PIV set-up(see section 5.3) are used for the assessment of the spanwise length of coherence. The mean velocity, RMS of the velocity fluctuation and a snapshot of the instantaneous cross-plane velocity fields of u-component and v-component are shown in Figure 6.12.
The length of coherence is evaluated for both transverse (u) and streamwise (v) components. The spanwise coherence was calculated along the line parallel to the airfoil trailing edge, where the maximum RMS of velocity fluctuation locates. In

Figure 6.12, the trailing edge of the airfoil locates at $x = 0$, while the lines for calculation of coherence are marked with grey dash dots.

For the calculation of the coherence of fluctuations at two spatial locations, Equation 3.9 is adapted as:

$$\gamma^2(z, f) = \frac{|\langle \hat{u}'(z_0, f)\hat{u}'^*(z, f)\rangle|^2}{|\langle \hat{u}'(z_0, f)\hat{u}'^*(z_0, f)\rangle \langle \hat{u}'(z, f)\hat{u}'^*(z, f)\rangle|} \tag{6.4}$$

In this case, z_0 is chosen as the mid-span location.

The equivalent coherence length is dependent on the frequency f. In the current study, a Gaussian function is fitted for all the frequency components around the spanwise location $z = z_0$ (for detailed information, see Appendix A). The critical value of coherence function is chosen as $\gamma_c = e^{-2}$. The coherence length l is thus defined as the width of the coherence curve at the critical value.

As reported by literatures such as [35] and [43], the equivalent length indicates high values only at the frequency associated with large vortex shedding phenomena (in this case, the shedding frequency $314.9Hz$) and should drops drastically below or above the tone. However, for some reasons, the coherence length peaks at $271Hz$ based on the stereoscopic measurements of this study. For the reason that the coherence length is later applied for the correction of the planar PIV acoustic prediction, it is rescaled such that the peak coherence length locates at $314.9Hz$. The length of coherence is plotted with respect to frequency in Figure 6.13.

The occurrence of $271Hz$ frequency in the coherence length is incongruous when compared to the shedding frequency measured by planar PIV, however, it is consistent with the stereoscopic PIV measurement, since under the set-up of stereoscopic PIV, the shedding frequency is measured as $271Hz$. The experimental data obtained by J.Shah[63], who applied similar experimental set-up, also reports discrepancy in shedding frequencies measured by planar and stereoscopic PIV set-ups. The phenomenon can be a result of change in test section material in two set-ups. The discussion on the discrepancy of shedding frequency is dilated in Appendix B.

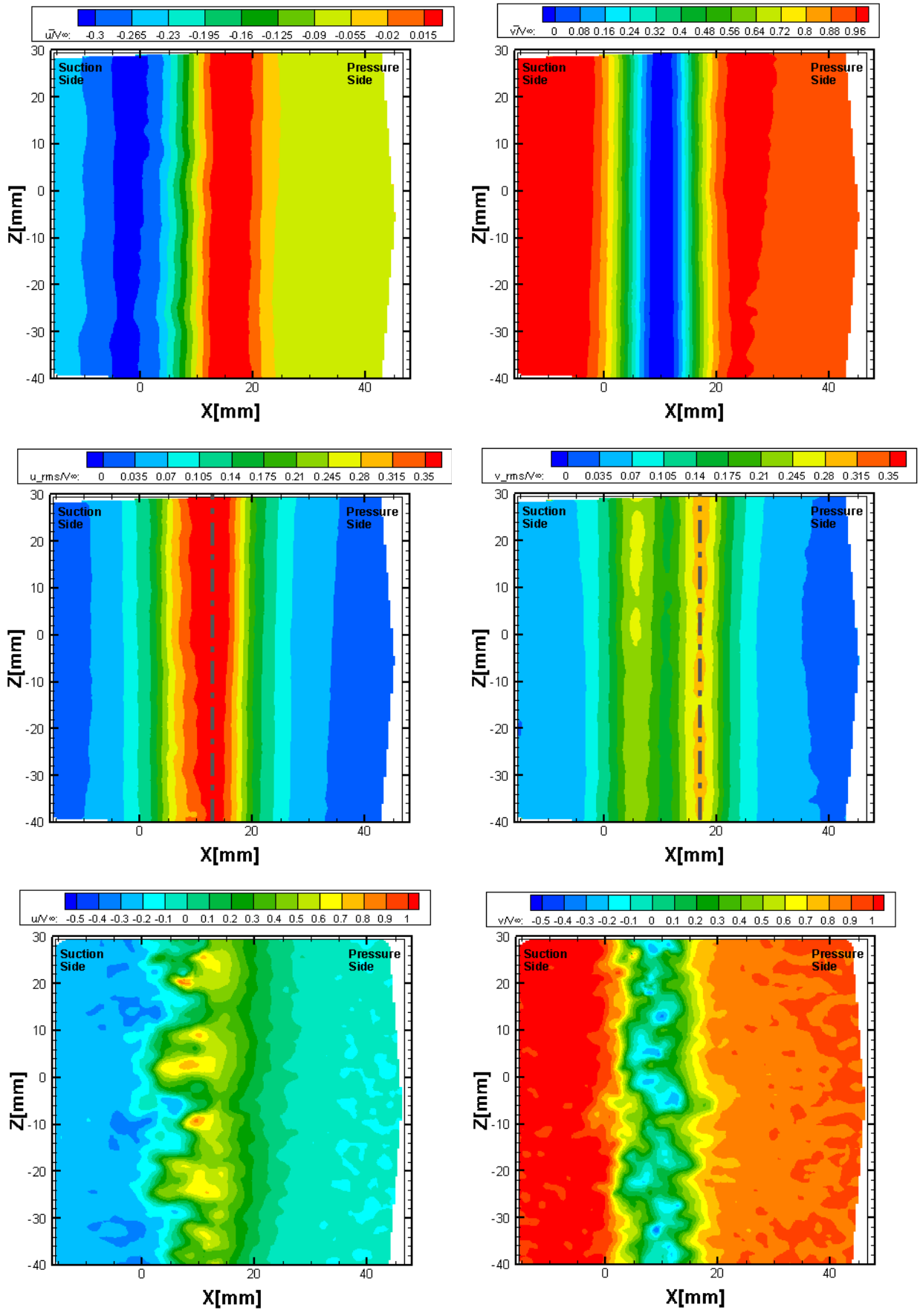

Figure 6.12: Stereoscopic PIV measurement: GF6-AOA4-V20, $z = 15mm$ (First row: mean velocity, Second row: velocity RMS, Third row: a snapshot of instantaneous velocity, Left column: transverse u-component, Right column: streamwise v-component)

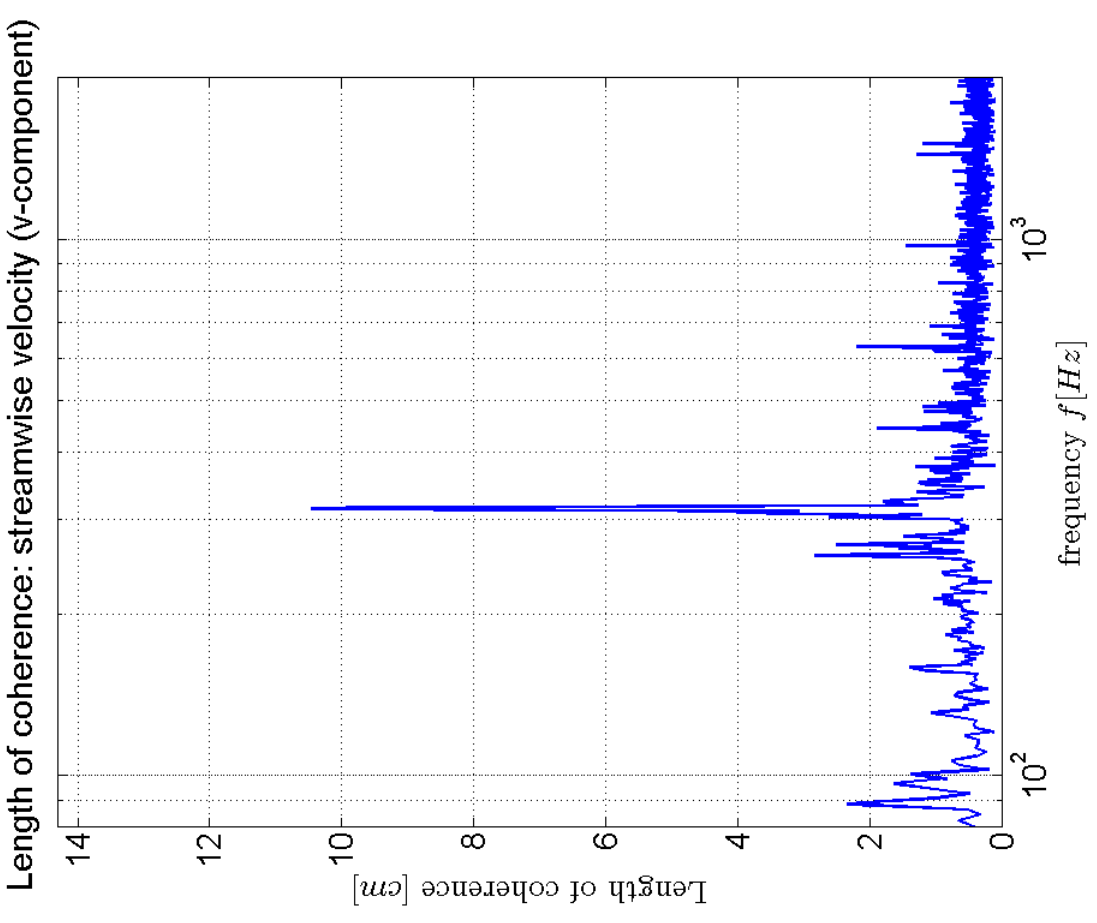

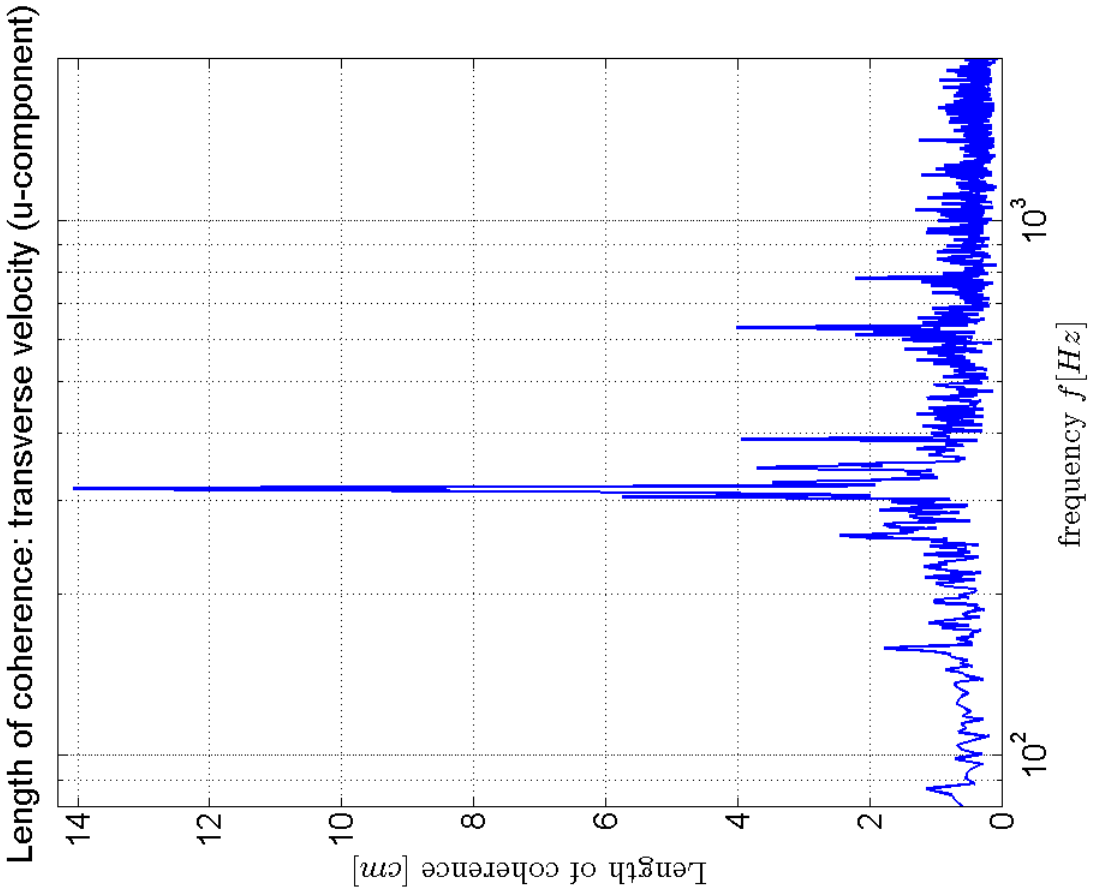

Figure 6.13: Coherence length of the transverse (u-component) and streamwise (v-component) velocity calculated from stereoscopic PIV measurement.

6.4.2 Correction to the full coherence prediction

The values of the coherence length are used for the corrections of the 2D predictions of the far-field acoustic pressure, which corresponds to adding to each specified frequency a correction value equals to:

$$-10log_{10}\left(\frac{L}{l(f)}\right) \tag{6.5}$$

where L is the full span length, and $l(f)$ is the coherence length at the specified frequency f.

The corrections of both the coherence length calculated from u-component(green prisms) and that from v-components(black diamonds) are applied. Figure 6.14 to 6.17 illustrate the results of corrections on the acoustic prediction from distributed formulation of Curle's analogy, and figure 6.18 to 6.21 show the results of corrections on the acoustic prediction from lumped formulation of Curle's analogy.

It can be observed that for both formulations of the Curle's analogy, the coherence length correction improves the acoustic prediction in the right tendency, that is to decrease the amplitude. The corrected predictions by distributed formulation yield amplitudes lower than the microphone measurements, while for the prediction by lumped formulation, the over-estimation is not completely removed by the correction.

However, the results of coherence length correction presented in this section is only illustrative of the viability of this method. Within the scope of current study, the effectiveness of the coherence length correction cannot be evaluated, since the above-mentioned shift in shedding frequency observed in the stereoscopic PIV measurements has rendered the evaluation of coherence length questionable.

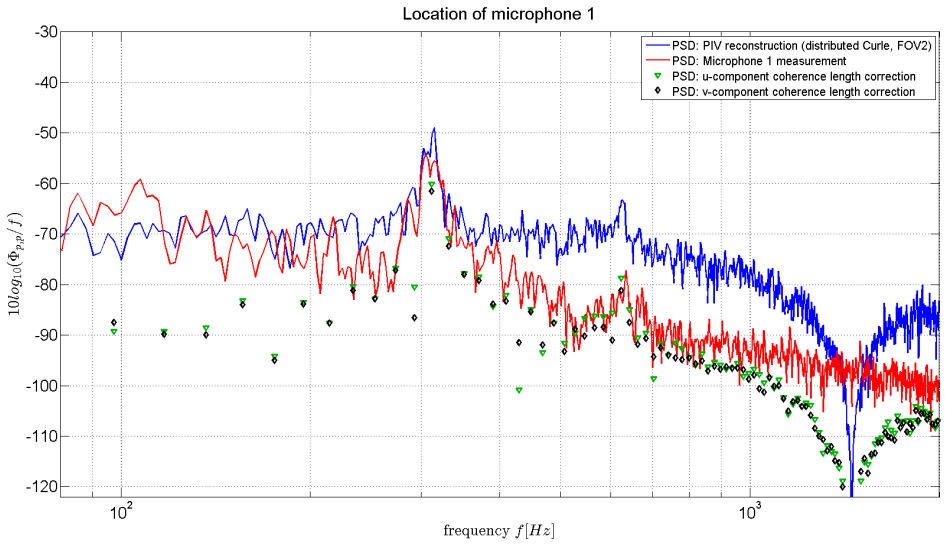

Figure 6.14: Power spectra ($\Delta f = 2.4Hz$) of acoustic pressure predicted by distributed formulation of Curle's analogy at the location of Microphone 1: correction based on measured spanwise coherence of transverse (u) and streamwise (v) velocity

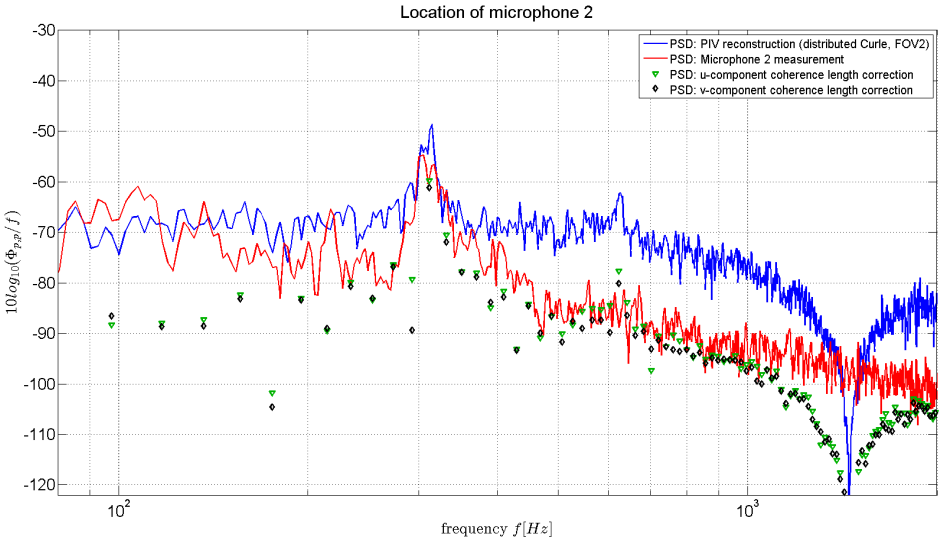

Figure 6.15: Power spectra ($\Delta f = 2.4Hz$) of acoustic pressure predicted by distributed formulation of Curle's analogy at the location of Microphone 2: correction based on measured spanwise coherence of transverse (u) and streamwise (v) velocity

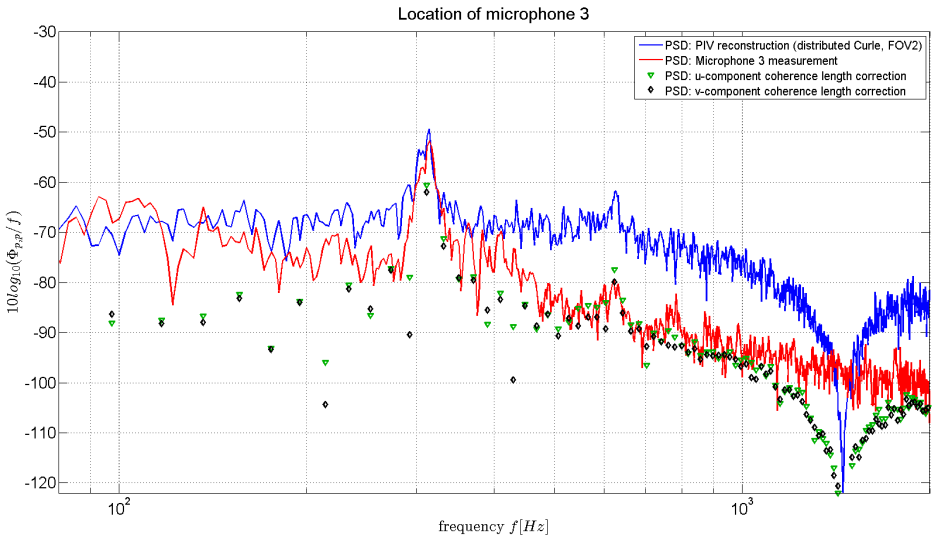

Figure 6.16: Power spectra ($\Delta f = 2.4Hz$) of acoustic pressure predicted by distributed formulation of Curle's analogy at the location of Microphone 3: correction based on measured spanwise coherence of transverse (u) and streamwise (v) velocity

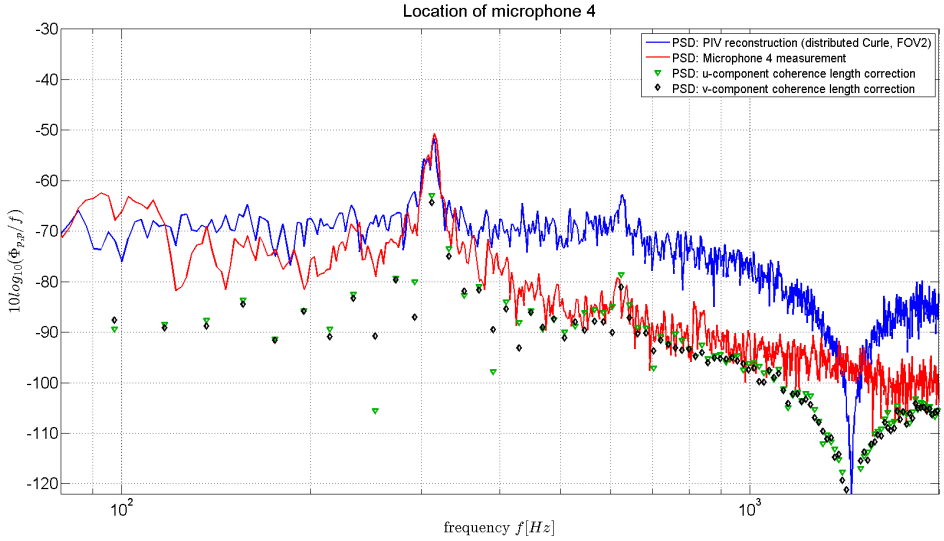

Figure 6.17: Power spectra ($\Delta f = 2.4Hz$) of acoustic pressure predicted by distributed formulation of Curle's analogy at the location of Microphone 4: correction based on measured spanwise coherence of transverse (u) and streamwise (v) velocity

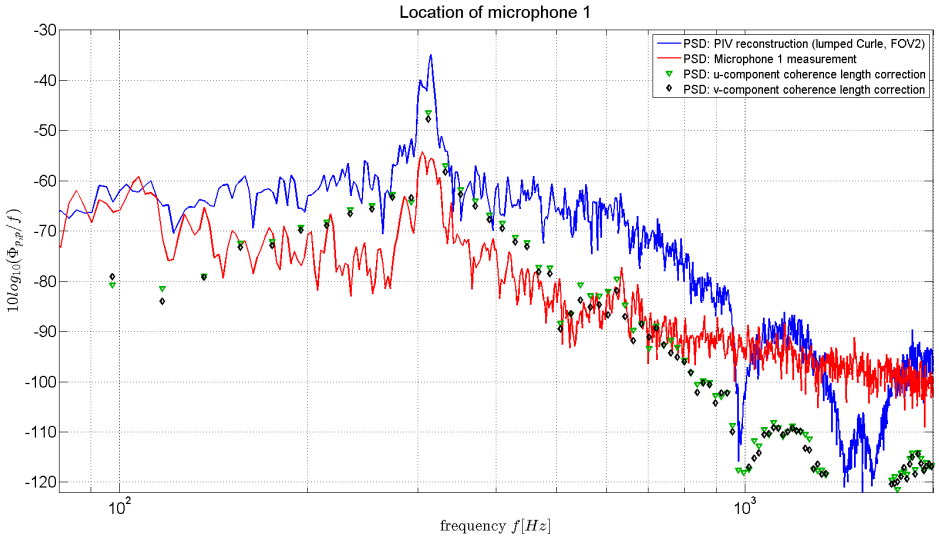

Figure 6.18: Power spectra ($\Delta f = 2.4Hz$) of acoustic pressure predicted by lumped formulation of Curle's analogy at the location of Microphone 1: correction based on measured spanwise coherence of transverse (u) and streamwise (v) velocity

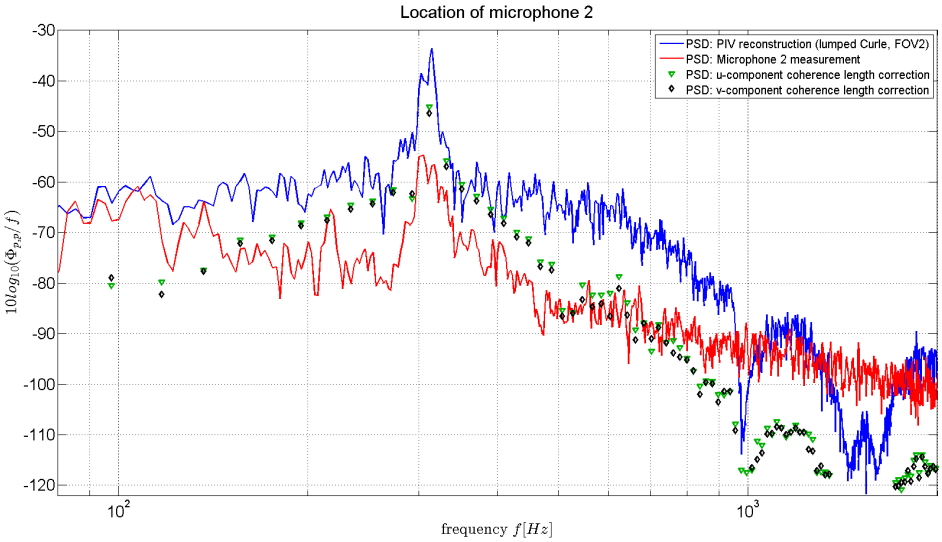

Figure 6.19: Power spectra ($\Delta f = 2.4Hz$) of acoustic pressure predicted by lumped formulation of Curle's analogy at the location of Microphone 2: correction based on measured spanwise coherence of transverse (u) and streamwise (v) velocity

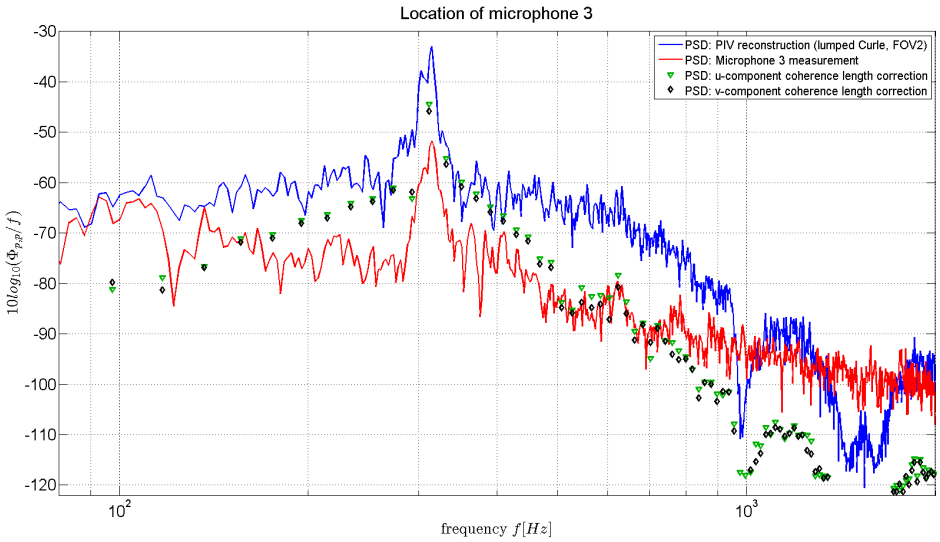

Figure 6.20: Power spectra ($\Delta f = 2.4Hz$) of acoustic pressure predicted by lumped formulation of Curle's analogy at the location of Microphone 3: correction based on measured spanwise coherence of transverse (u) and streamwise (v) velocity

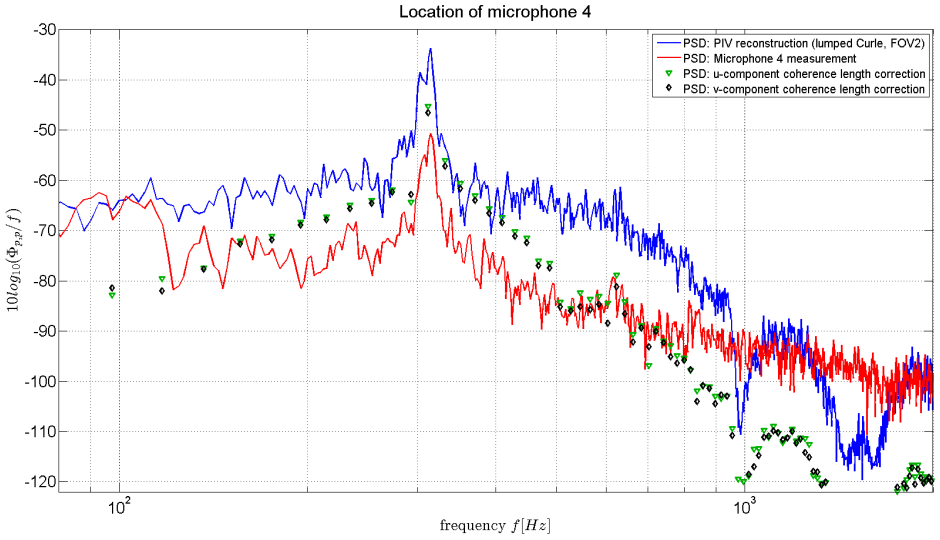

Figure 6.21: Power spectra ($\Delta f = 2.4Hz$) of acoustic pressure predicted by lumped formulation of Curle's analogy at the location of Microphone 4: correction based on measured spanwise coherence of transverse (u) and streamwise (v) velocity

Chapter 7

Conclusions and recommendations

An aeroacoustic investigation on NACA 0015 with Gurney flap has been performed based on the measurements of time-resolved PIV. This chapter first highlights the main findings of this study in section 7.1, following which, the recommendations for the future investigations are given in section 7.2.

7.1 Conclusions

The main findings from the literature study, the experimental campaigns and the analysis of the present work, as listed below:

1. The Kármán vortex shedding is the dominating vortex shedding mode of the Gurney flap. The interaction between the vortices and solid boundaries forms dipolar sources resided on the solid surface, which is the major source of the noise generated by trailing edge with Gurney flap. The frequency of the tonal noise is consistent with the frequency of vortex shedding. The power spectra of the fluctuations of velocity, aerodynamic loads and far-field pressure did not indicate the existence of the second shedding mode for this configuration

as the one proposed by Troolin et al.[64]. (chapter 2, chapter 6)

2. The in-plane pressure was reconstructed from PIV measured velocity with the in-plane Poisson solver proposed by Gurka et al.[18] for both the measurements on FOV 1 and FOV 2. Coherence pattern and distinguishable convection can be observed downstream the Gurney flap in the reconstructed pressure field. In addition the locations of the local minima of the reconstructed pressure are consistent with the locations of vortex cores identified in the vorticity field. (chapter 6: section 6.1)

3. The far-field acoustic pressure predicted by the distributed formulation of the Curle's analogy based on the in-plane pressure reconstruction yielded results that were slightly over-estimated but in fair agreement with the simultaneous microphone measurements. However, the noise level predicted under the full span coherence assumption was lower than expected. The phenomenon can be attributed to the damping of fluctuations because of the Gaussian smoothing. For the case of FOV 1, the deliberate rise in enstrophy threshold for more Dirichlet boundary conditions also contributed to the damping effect.(chapter 6: section 6.2)

4. The noise level predicted by the lumped formulation is higher than that of the distributed formulation, and at all four microphone locations, the PIV measurements yielded over-estimation in noise level when compared to the simultaneous microphone measurements. Such over-estimation was expected under the assumption of full span coherence. The lumped formulation of the Curle's analogy was implemented to avoid the smoothing of velocity field, and therefore avoiding the concomitant damping of the near-field fluctuations. (chapter 6: section 6.2, 6.3)

5. The over-estimated noise level under the full spanwise coherence assumption was corrected with the method of equivalent coherence length, proposed by Kato et al.[35]. The correction reduced the noise level on the power spectra for all frequencies. The correction was in the right direction, but the effectiveness cannot yet be estimated in this study for the reason of the observed inconsistency in shedding frequencies measured by planar PIV and stereoscopic PIV. The values of coherence length were rescaled before applied to

the noise level correction. (chapter 6:section 6.4)

7.2 Recommendations

The present study proved the applicability and revealed the limitation of the PIV techniques in the acoustic investigations of an airfoil with Gurney flap. Hereby are recommendations on the further researches on the topic:

- **Pressure reconstruction based on PIV measurements**
  For planar PIV measurements, before the implementation of the in-plane Poisson solver proposed by Gurka et al.(Equation 3.12), it is preferable that the velocity fields first be smoothed to remove the spurious spatial derivatives caused by experimental noise. And for the planar PIV set-up, it is advisable that the outer boundaries of the field of view should avoid the region with high vortex intensity and strong 3D motions. An alternative solution can be the use of tomographic PIV, which allows 3D flow visualization. In such a way, the 3D components in the source term of Equation 3.13 can be resolved.

- **Evaluation of far-field acoustic pressure**
  Under the experimental condition of planar PIV, lumped formulation of the Curle's analogy is preferable as it avoids resolving the pressure fluctuations on the solid surfaces. Although the far-field pressure fluctuation can be obtained with both formulations of the Curle's analogy, yet with the effect of the unresolved 3D motions which dominates the near-wake region, the fluctuations of pressure on the solid surface are damped in the process of in-plane pressure reconstruction.

- **Evaluation of the aerodynamic loads from PIV measurements**
  For the evaluation of aerodynamic loads for the application of the lumped formulation of the Curle's analogy, this study used the method of momentum balance proposed by Kurtulus et al.(Equation 3.14), which involves the pressure evaluation on the integral surfaces. Alternatively, the aerodynamic

forces can be computed directly from the velocity fields with the "flux equation" proposed by Noca et al. (Equation 3.16), circumventing completely the pressure reconstruction. Simultaneous PIV and balance (with high frequency response) measurements is a continuation of the current study, from which the accuracy of the two approaches can be evaluated.

- **Materials of the test sections**
  The materials of the test sections used in planar PIV and stereoscopic PIV measurements should remain the same, since the change in material leads to change in acoustic impedance of the side walls, and the vortex shedding frequency is found to be shifted by the transverse sound wave in the flow duct. Test sections of same materials can avoid the discrepancy in measured vortex shedding frequencies and thus the rescaling of coherence length. Although plexiglass is the preferable test section material for the PIV set-up, yet it is advisable that at least one side wall of the test section be made of Kevlar in order to avoid the flow induced resonance.

- **Application to high-lift devices with complex structure**
  With the feasibility of PIV based acoustic prediction proved on the Gurney flap, a prospective extension can be the application of the PIV technique to the noise prediction of high-lift devices with structures that are more complex. This continuation may facilitate the design of quieter lift enhancing devices.

Bibliography

[1] J. Anderson Jr. *Fundamentals of Aerodynamics*. McGraw Hill, 2001.

[2] T Baur and J Köngeter. Piv with high temporal resolution for the determination of local pressure reductions from coherent turbulence phenomena. In *3rd international workshop on particle image velocimetry, Santa Barbara, CA, USA*, 1999.

[3] Julius S Bendat and Allan G Piersol. *Random data: analysis and measurement procedures*, volume 729. John Wiley & Sons, 2011.

[4] Stephen A Billings. *Nonlinear system identification: NARMAX methods in the time, frequency, and spatio-temporal domains*. John Wiley & Sons, 2013.

[5] RD Blevins. The effect of sound on vortex shedding from cylinders. *Journal of Fluid Mechanics*, 161:217–237, 1985.

[6] YN Chen. Criteria for the cross-flow-induced tube vibrations in tube bank heat exchangers. In *Vibration in nuclear plant. Proceedings of international conference held at Keswick, UK in May 1978*, 1979.

[7] National Research Council. *Improving the Continued Airworthiness of Civil Aircraft: A Strategy for the FAA's Aircraft Certification Service*. The National Academies Press, Washington DC, 1998.

[8] DG Crighton and FG Leppington. Scattering of aerodynamic noise by a semi-infinite compliant plate. *Journal of Fluid Mechanics*, 43(04):721–736, 1970.

[9] N Curle. The influence of solid boundaries upon aerodynamic sound. In *Proceedings of the Royal Society of London A: Mathematical, Physical and Engineering Sciences*, volume 231, pages 505–514. The Royal Society, 1955.

[10] R De Kat and BW Van Oudheusden. Instantaneous planar pressure determination from piv in turbulent flow. *Experiments in fluids*, 52(5):1089–1106, 2012.

[11] Roeland de Kat and Bas W van Oudheusden. Instantaneous planar pressure from piv: analytic and experimental test-cases. In *Proceedings of the 15th international symposium on applications of laser techniques to fluid mechanics, Lisbon, Portugal*, 2010.

[12] Roeland De Kat, Bas W Van Oudheusden, and Fulvio Scarano. Instantaneous planar pressure field determination around a square-section cylinder based on time resolved stereo-piv. In *Proceedings of the 14th International Symposium on Applications of Laser Techniques to Fluid Mechanics, Lisbon, Posrtugal, 07-10 July, 2008, paper No. 1259*. Calouste Gulbenkian Foundation, 2008.

[13] M Debrouwere. An assessment of acoustically transparent wind tunnel walls. *Master of Science Thesis, Delf university of technology, Aerospace department*, 2013.

[14] John M Eargle. *Handbook of recording engineering*. Springer Science & Business Media, 2012.

[15] Scarano F. Experimental aerodynamics. Lecture Notes, 2013.

[16] LaVision GmbH. Piv image evaluation. http://www.piv.de/piv/measurement_principle/page_1.php. Accessed: 2015-09-29.

[17] Marvin E Goldstein. Aeroacoustics. *New York, McGraw-Hill International Book Co., 1976. 305 p.*, 1, 1976.

[18] Roi Gurka, Alex Liberzon, D Hefetz, D Rubinstein, and U Shavit. Computation of pressure distribution using piv velocity data. In *Workshop on particle image velocimetry*, volume 2, 1999.

[19] Richard Haberman. Applied partial differential equations with fourier series and boundary value problems. *AMC*, 10:12, 2004.

[20] Christian Haigermoser. Application of an acoustic analogy to piv data from rectangular cavity flows. *Experiments in fluids*, 47(1):145–157, 2009.

[21] Colin H Hansen and David A Bies. *Engineering noise control*. Spon, 1995.

[22] Arne Henning, Kristian Kaepernick, Klaus Ehrenfried, Lars Koop, and Andreas Dillmann. Investigation of aeroacoustic noise generation by simultaneous particle image velocimetry and microphone measurements. *Experiments in fluids*, 45(6):1073–1085, 2008.

[23] Arne Henning, Lars Koop, and Klaus Ehrenfried. Simultaneous particle image velocimetry and microphone array measurements on a rod-airfoil configuration. *AIAA journal*, 48(10):2263–2273, 2010.

[24] Arne Henning, Andreas Schröder, Lars Koop, and J Agocs. Causality correlation analysis on a cold jet by means of simultaneous piv and microphone measurements. In *6th AIAA/CEAS Aeroacoustics Conference, Stockholm (Sweden), vol AiAA-2010-3753*, 2010.

[25] Arne Henning, Björn Wrede, and Reinhard Geisler. Aeroacoustic investigation of a high-lift device by means of synchronized piv and microphone measurements.

[26] Arne Henning, Björn Wrede, and Andreas Schröder. About the ambiguity of noise source localization based on the causality correlation technique. In *Proceedings of the 17th international symposium on applications of laser techniques to fluid mechanics, Lisbon, Portugal*, 2014.

[27] Avraham Hirschberg and Christophe Schram. A primitive approach to aeroacoustics. In *Sound-Flow Interactions*, pages 1–30. Springer, 2002.

[28] Michael S Howe. *Theory of vortex sound*, volume 33. Cambridge University Press, 2003.

[29] MS Howe. The influence of vortex shedding on the generation of sound by convected turbulence. *Journal of Fluid Mechanics*, 76(04):711–740, 1976.

[30] MS Howe. A review of the theory of trailing edge noise. *Journal of Sound and Vibration*, 61(3):437–465, 1978.

[31] LinearX Systems Inc. *M53 Measurement Microphone*, 2000.

[32] American National Standards Institute. *American National Psychoacoustical Terminology S3.20*. American Standard Association, 1973.

[33] David Jeffrey, Xin Zhang, and David W Hurst. Aerodynamics of gurney flaps on a single-element high-lift wing. *Journal of Aircraft*, 37(2):295–301, 2000.

[34] MG Jones, WR Watson, and TL Parrott. Benchmark data for evaluation of aeroacoustic propagation codes with grazing flow. *AIAA paper*, 2853:2005, 2005.

[35] Chisachi Kato, AKIYOSHI Iida, Yasushi Takano, HAJIME Fujita, and MASAHIRO Ikegawa. Numerical prediction of aerodynamic noise radiated from low mach number turbulent wake. *AIAA paper*, (93-0145), 1993.

[36] Valentina Koschatzky, Jerry Westerweel, and Bendiks Jan Boersma. Comparison of two acoustic analogies applied to experimental piv data for cavity sound emission estimation. In *Proceedings of the 16th AIAA/CEAS Aeroacoustic Conference*, pages 7–9, 2010.

[37] DF Kurtulus, F Scarano, and L David. Unsteady aerodynamic forces estimation on a square cylinder by tr-piv. *Experiments in Fluids*, 42(2):185–196, 2007.

[38] LD Landau and EM Lifshitz. Fluid mechanics, vol. 6. *Course of Theoretical Physics*, pages 227–229, 1987.

[39] YC Li, JJ Wang, GK Tan, and PF Zhang. Effects of gurney flaps on the lift enhancement of a cropped nonslender delta wing. *Experiments in fluids*, 32(1):99–105, 2002.

[40] Robert H Liebeck. Design of subsonic airfoils for high lift. *Journal of aircraft*, 15(9):547–561, 1978.

[41] Michael J Lighthill. On sound generated aerodynamically. i. general theory. In *Proceedings of the Royal Society of London A: Mathematical, Physical and Engineering Sciences*, volume 211, pages 564–587. The Royal Society, 1952.

[42] Xiaofeng Liu and Joseph Katz. Instantaneous pressure and material acceleration measurements using a four-exposure piv system. *Experiments in Fluids*, 41(2):227–240, 2006.

[43] V Lorenzoni, M Tuinstra, and F Scarano. On the use of time-resolved particle image velocimetry for the investigation of rod–airfoil aeroacoustics. *Journal of Sound and Vibration*, 331(23):5012–5027, 2012.

[44] Valerio Lorenzoni. Aeroacoustic Investigation of Rod-Airfoil Noise based on Time-Resolved PIV. Master's thesis, Delft University of Technology, the Netherlands, 2008.

[45] David Mackenzie. *ICAO: a history of the international civil aviation organization*. University of Toronto Press, 2010.

[46] American Scientist Magazine. http://www.americanscientist.org/Libraries/images/201473114311210514-2014-09CoxF3.jpg. Accessed: 2015-11-03.

[47] Thomas J Mueller. *Aeroacoustic measurements*. Springer Science & Business Media, 2002.

[48] Roy Myose, Michael Papadakis, and Ismael Heron. Gurney flap experiments on airfoils, wings, and reflection plane model. *Journal of Aircraft*, 35(2):206–211, 1998.

[49] Tomomichi Nakamura, Shigehiko Kaneko, Fumio Inada, Minoru Kato, Kunihiko Ishihara, Takashi Nishihara, and Njuki W Mureithi. *Flow-induced vibrations: Classifications and lessons from practical experiences*. Butterworth-Heinemann, 2013.

[50] F Noca, D Shiels, and D Jeon. A comparison of methods for evaluating time-dependent fluid dynamic forces on bodies, using only velocity fields and their derivatives. *Journal of Fluids and Structures*, 13(5):551–578, 1999.

[51] RM Oreslli, Julio R Meneghini, and Fabio Saltara. Two and three-dimensional simulation of sound generated by flow around a circular cylinder. In *15th AIAA/CEAS Aeroacoustics Conference, AIAA*, volume 3270, 2009.

[52] G Philippe, D Guy, and L Jean. Gurney flap scaling for optimum lift-to drag ratio. *AIAA j*, 35(12):1888–1890, 1997.

[53] Alan Powell. On the aerodynamic noise of a rigid flat plate moving at zero incidence. *The Journal of the Acoustical Society of America*, 31(12):1649–1653, 1959.

[54] Alan Powell. Theory of vortex sound. *The journal of the acoustical society of America*, 36(1):177–195, 1964.

[55] S Probsting. Coherent structures at the serrated trailing-edge of a naca 0012. *Master of Science Thesis, Delf university of technology, Aerospace department*, 2012.

[56] Stefan Pröbsting, Fulvio Scarano, Matteo Bernardini, and Sergio Pirozzoli. On the estimation of wall pressure coherence using time-resolved tomographic piv. *Experiments in fluids*, 54(7):1–15, 2013.

[57] Markus Raffel, Christian E Willert, Jürgen Kompenhans, et al. *Particle image velocimetry: a practical guide*. Springer, 2013.

[58] M Roger. Aeroacoustics: Some theoretical background—the acoustic analogy. *Computational Aeroacoustics*, pages 2006–05, 2006.

[59] Daniel A Russell, Joseph P Titlow, and Ya-Juan Bemmen. Acoustic monopoles, dipoles, and quadrupoles: An experiment revisited. *American Journal of Physics*, 67(8):660–664, 1999.

[60] T.Watanabe S. Hayama. In *Proceedings of the 73rd JSME's Annual Meeting (in Japanese) pp.155 á156*, 1995.

[61] S Salcedo, F Monge, F Palacios, F Gandía, A Rodríguez, M Barcala, and Crtra Ajalvir. Gurney flaps and trailing edge devices for wind turbines. *EWEC. Athens: EWEA*, 2006.

[62] Christophe Schram and Lilla Koloszár. Validation and improvement of airframe noise prediction tools. *Innovation for Sustainable Aviation in a Global Environment: Proceedings of the Sixth European Aeronautics Days, Madrid, 30 March-1 April, 2011*, page 144, 2012.

[63] J Shah. Aeroacoustics and flow dynamics of an airfoil with a gurney flap using tr-piv. *Master of Science Thesis, Delf university of technology, Aerospace department*, 2015.

[64] DR Troolin, EK Longmire, and WT Lai. Time resolved piv analysis of flow over a naca 0015 airfoil with gurney flap. *Experiments in Fluids*, 41(2):241–254, 2006.

[65] Seppo Uosukainen. *Foundations of acoustic analogies*. VTT Publications 757, 2011.

[66] Bas W van Oudheusden, Fulvio Scarano, Eric WM Roosenboom, Eric WF Casimiri, and Louis J Souverein. Evaluation of integral forces and pressure fields from planar velocimetry data for incompressible and compressible flows. *Experiments in Fluids*, 43(2-3):153–162, 2007.

[67] Walter G Vincenti. *What engineers know and how they know it*, volume 141. Baltimore: Johns Hopkins University Press, 1990.

[68] Daniele Violato, Peter Moore, and Fulvio Scarano. Lagrangian and eulerian pressure field evaluation of rod-airfoil flow from time-resolved tomographic piv. *Experiments in fluids*, 50(4):1057–1070, 2011.

[69] JJ Wang, YC Li, and K-S Choi. Gurney flap—lift enhancement, mechanisms and applications. *Progress in Aerospace Sciences*, 44(1):22–47, 2008.

[70] Meng Wang, Jonathan B Freund, and Sanjiva K Lele. Computational prediction of flow-generated sound. *Annu. Rev. Fluid Mech.*, 38:483–512, 2006.

[71] Jerry Westerweel and Fulvio Scarano. Universal outlier detection for piv data. *Experiments in Fluids*, 39(6):1096–1100, 2005.

[72] B Wieneke. Stereo-piv using self-calibration on particle images. *Experiments in Fluids*, 39(2):267–280, 2005.

[73] Wikipedia. Open cylinder resonance. https://upload.wikimedia.org/wikipedia/commons/4/48/OpenCylinderResonance.svg. Accessed: 2015-12-01.

[74] JE Williams and LH Hall. Aerodynamic sound generation by turbulent flow in the vicinity of a scattering half plane. *Journal of Fluid Mechanics*, 40(04):657–670, 1970.

[75] JE Ffowcs Williams. Hydrodynamic noise. *Annual Review of Fluid Mechanics*, 1(1):197–222, 1969.

[76] X Zhang. Finite element numerical simulation of straightforward method for liner impedance eduction. *Bachelor of Science Thesis (in Chinese), Beihang University, School of Jet Propulsion*, 2013.

Appendix A

Gaussian curve fitting for the evaluation of coherence length

The purpose of the present appendix is to offer a brief mathematical description of the Gaussian curve fit procedure applied in the computation of spanwise coherence length, as mentioned in subsection 6.4.1.
The standard Gaussian equation is written as:

$$y = g(x) = Ae^{-\frac{(x-\mu)^2}{2\sigma^2}} \tag{A.1}$$

Based on the considerations of the properties of the coherence, the coherence coefficients ranges from 0 to 1, and thus in this case $A = 1$. In addition, the value of coherence coefficients are calculated at a specified spanwise location with respect to the mid-span location ($z = 0$), such that at $z = 0$, the coherence coefficient reaches the maximum value 1, and thus $\mu = 1$. The Gaussian equation used in the curve fitting hence takes a simplified form of:

$$y = g(x) = e^{-\frac{x^2}{2\sigma^2}} \tag{A.2}$$

In this case, y takes the values of coherence coefficients calculated basd on the measurements of stereoscopic PIV, and x the spanwise locations, with $z = 0$ the

location of the mid-span location.

As can be observed in Figure A.1, besides the main peak at the mid-span location where coherence coefficient takes the value of unity, there are secondary peaks. However, Gaussian function should be fitted with the data points that constitute only the main peak. In order to identify the portion of data corresponding to the main peak automatically for the data at each frequency, the first derivatives of the curve at the specified frequencies have been investigated. A Matlab® programme searches for the spanwise locations where the first derivatives change signs. Between the nearest sign-changing locations on both sides of the mid-span (marked with magenta lines on Figure A.1), the portion of data is taken for the curve fitting.

The present Gaussian curve fitting problem can be converted to problem of solv-

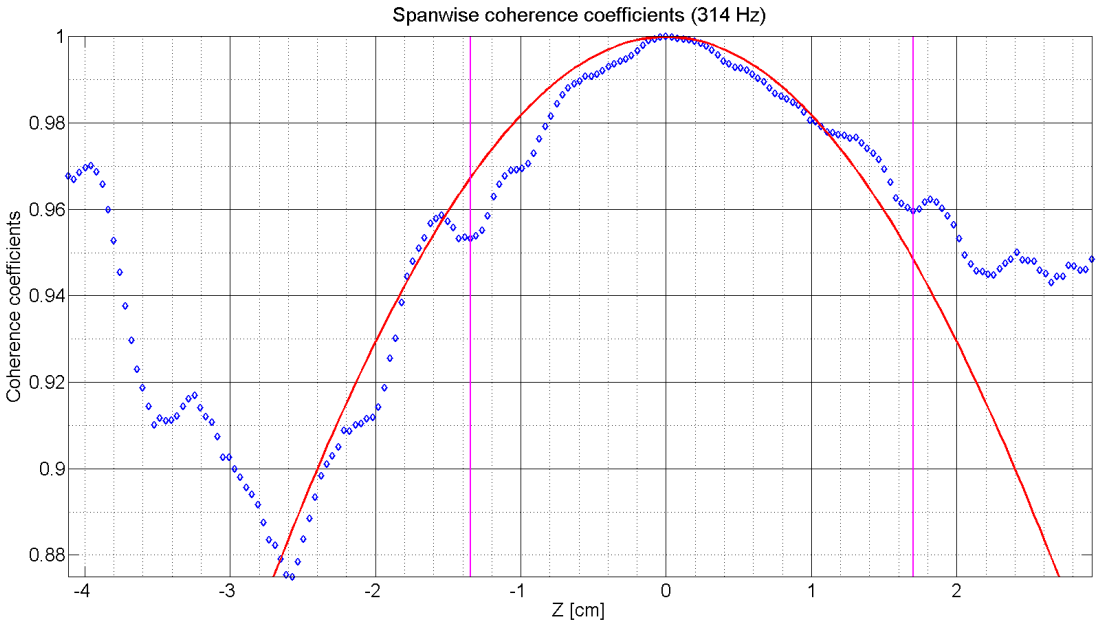

Figure A.1: Gaussian curve fit of the spanwise coherent coefficients

ing a overdetermined system of linear equations, and thus the linear least square approach can be applied to determine the value of standard deviation σ.

Take log of both side, then Equation A.2 becomes:

$$ln(y) = -\frac{x^2}{2\sigma^2} \tag{A.3}$$

then let $Y = ln(y)$, $a = \frac{1}{2\sigma^2}$, $X = x^2$, the system can be rewritten as linear functions:

$$Y_i = aX_i + \varepsilon_i \tag{A.4}$$

Finding the optimized slope a is equivalent in minimizing the objective function:

$$\underset{a}{min} Q(a) \tag{A.5}$$

for $Q(a) = \sum \varepsilon_i^2 = \sum (Y_i - aX_i)^2$. In other word, a is the solution of the following minimization problem. By using the calculus:

$$\frac{\partial S}{\partial a} = 0 \tag{A.6}$$

it can be shown that a that minimize the objective function is:

$$\hat{a} = \frac{\sum Y_i k_i}{\sum X_i^2} \tag{A.7}$$

Correspondingly, the σ that optimizes the curve fitting is $\hat{\sigma} = \sqrt{-1/2\hat{a}}$. The coherence length is then approximated with the distance between the mid-span location ($z = 0$) and location where the Gaussian function reaches the critical value. Different critical values were taken by authors of the references mentioned in subsection 6.4.1 and currently there exists no rule of thumb for the choice of this critical value. In the present study, e^{-2} is chosen as the critical value, such that the Gaussian function reaches the critical value at $x = 2\sigma$. Since the range $[-2\sigma\ 2\sigma]$ contains 95% of the total integral of the Gaussian function, thus 2σ corresponds to the 95% confidence level and expresses a conventional heuristic in the empirical sciences. Whether the value of e^{-2} is the suitable for the flow under investigation is still a topic open for further investigations.

An example of the fitted Gaussian function is plotted in Figure A.2 with the frequency specified at $f = 314Hz$. The blue diamonds show the calculated coherent coefficients at each spanwise location with respect to the mid-span, the red line plots the fitted Gaussian curve within the FOV of the stereoscopic PIV, and the dotted line is the extrapolation of the Gaussian function to the spanwise locations outside the FOV. The extrapolation is only necessary for the frequencies (such as $f = 314Hz$ as shown) at which the value of coherence coefficients does not drop below the specified critical value within the FOV.

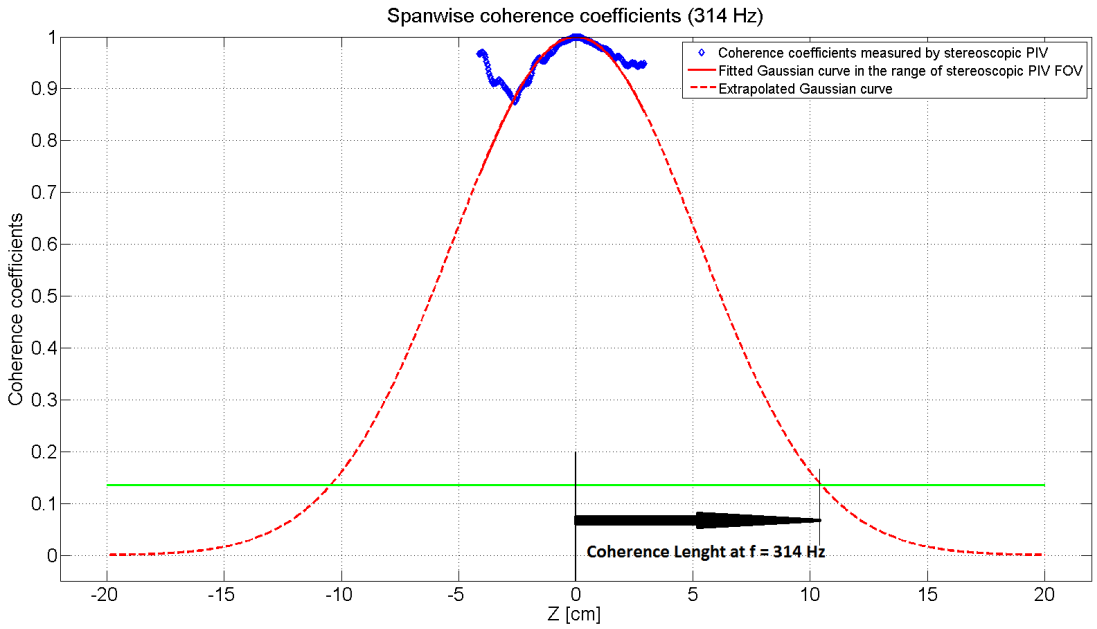

Figure A.2: Extrapolated Gaussian curve and the predicted length of coherence

Appendix B

On the different shedding frequency obtained from the planar and stereoscopic PIV measurements

As has been mentioned in subsection 6.4.1, the velocity fluctuations measured by stereoscopic PIV exhibit a frequency peak, corresponding to the vortex shedding frequency, of $271Hz$ in the power spectra, which deviates from the $314.9Hz$ measured by planar PIV and the far-field microphones. A comparison of the power spectra obtained from the measurements of the two different PIV set-ups is given in Figure B.1. The present appendix offers a qualitative discussion on the mechanism of the observed frequency shift.

As described in chapter 5, two side walls of the test section for simultaneous planar PIV measurements are made of Kevlar, which is permeable for acoustic waves, while the side walls for stereoscopic PIV measurements are all plexiglass in order to facilitate the pass of laser light. The change in material essentially leads to the change in acoustic impedance of the test section walls, which may result in resonance when the following two conditions are satisfied:

- **Frequency condition:** the frequency of excitation coincides with the natural frequency of any acoustic mode of the flow duct.

- **Energy condition:** the energy input to the acoustic mode exceeds the energy dissipation of this mode in the acoustic field.

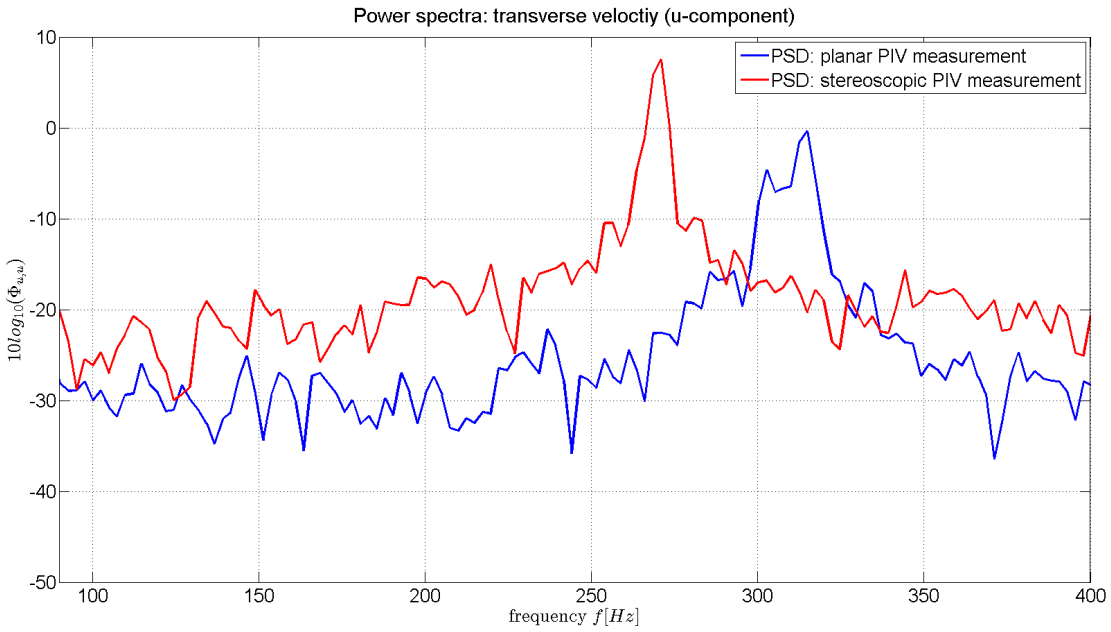

Figure B.1: Comparison of the power spectra ($\Delta f = 2.4Hz$) of the transverse velocity (u-component) measured by planar PIV and stereoscopic PIV (GF6-AOA4-V20).

In the experimental campaign, at the same incoming flow rate and with the same model, the experiments with all-plexiglass test section were audibly noisier than those with plexiglass-Kevlar test section. A possible explanation can be inferred that the shift in vortex shedding frequency is the result of the effect of sound on vortex shedding. Figure B.2 shows the schematic of the feedback mechanism between the flow and acoustic field.

The influence of a transverse sound wave on vortex shedding frequency of a rigid circular cylinder in a duct has been explored by Blevins(1985) [5], the findings of which can be summarized as:

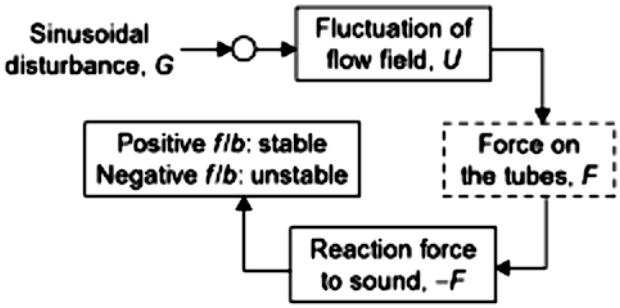

Figure B.2: Feedback mechanism between flow and acoustic field.[49]

1. In absence of the sound, vortex shedding is not a steady harmonic process, but wanders $1-2\%$ around the nominal vortex shedding frequency. Applied sound reduces the bandwidth of vortex shedding and when the strength of the sound reaches a certain threshold, the frequency wander can be completely eliminated (in some literatures, this phenomenon is also referred to as 'locked-in' effect).

2. Sound applied near the vortex shedding frequency shifts the vortex shedding towards the sound frequency. Maximum shifts of 8% in frequency were achieved with the sound of higher frequency than the vortex shedding. Blevins further claimed a tendency for the preferred vortex-shedding frequency to decrease when sound is applied and expected a larger shift by applying sound with frequency lower than the shedding frequency.

3. The entrainment produced by sound is due to the induced velocity of the sound wave rather than by the sound pressure. The greatest influence can be achieved when the cylinder is placed at a node of a sound pressure (an anti-node of the acoustic velocity).

4. Turbulence in the free stream tends to suppress the influence of sound. Sound-induced entrainment can occur only if the acoustic velocity is above the background turbulence velocities.

5. Correlation of vortex shedding along the cylinder span increases substantially when sound is applied at the vortex shedding frequency.

From Figure B.1, it can be observed that the width of the frequency peak measured by stereoscopic PIV is narrower than the one measured by planar PIV. And the increase in amplitude could be the result of energy input from the excitation. In addition, the V-tunnel provides incoming flow with turbulent level below 0.1%, which is very low. However, the cross-section of the test section used in the current study is $40 \times 40cm^2$, correspondingly, the frequency of the first transversal mode is $425Hz$, which is larger than and faraway from the natural shedding frequency $314.9Hz$. And thus, the transversal sound wave is not the reason and there should be other causes.

The investigations on the resonance of heat exchanger have revealed several similar phenomena in longitudinal wave in the flow duct. Chen reported the lock-in effect caused by longitudinal acoustic waves on vortex shedding back in 1979[6]. The location of the antinode of acoustic velocity was also discussed for longitudinal modes by Hayama et al.(1995) [60]. Yet shift in vortex shedding frequency caused by longitudinal wave mode is not found by the author of this thesis in the literatures about vibrations in tube bank heat exchangers. Figure B.3 shows the shapes of the first three longitudinal modes in an open cylindrical tube.

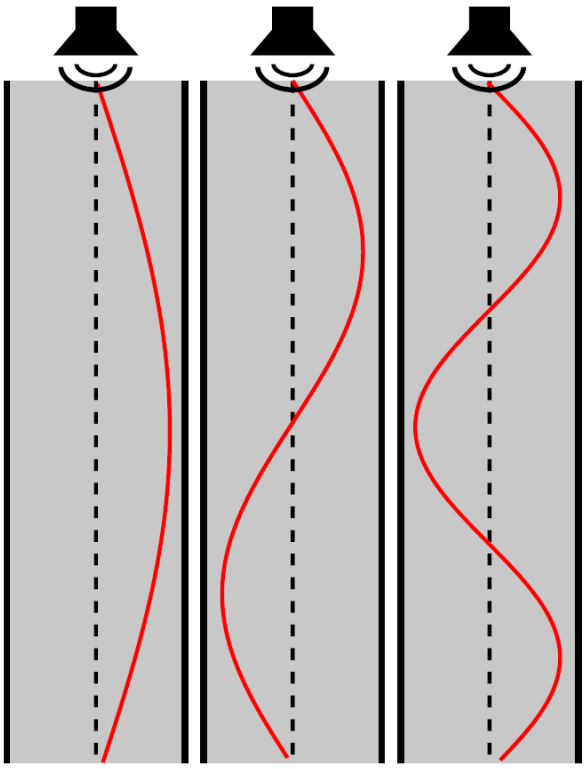

Figure B.3: The first three resonance modes in an open cylindrical tube. The horizontal axis is pressure.[73]

In the current study, the total height (test section and part of the transition duct) of the flow duct with the cross-section of $40 \times 40cm^2$ is around

$0.8m$, which corresponds to the frequency of the first longitudinal mode of $215Hz$. This longitudinal frequency may have contributed to the shift in vortex shedding frequency of the Gurney flap.
A local maxima at $215Hz$ is distinguishable, but not evident on the power spectrum of the background noise of the wind tunnel in operation (Figure B.4). However, the background noise was measured with the installation of the plexiglass-Kevlar test section, while the background noise measurement on all-plexiglass test section is missing. If the longitudinal mode of $215Hz$ is the mode that shifts the vortex shedding in the all-plexiglass case, a more discernible peak is expected on the background noise power spectrum of that case. Another issue that remains to be clarified is what the energy input is, or excitation of the $215Hz$ longitudinal mode.

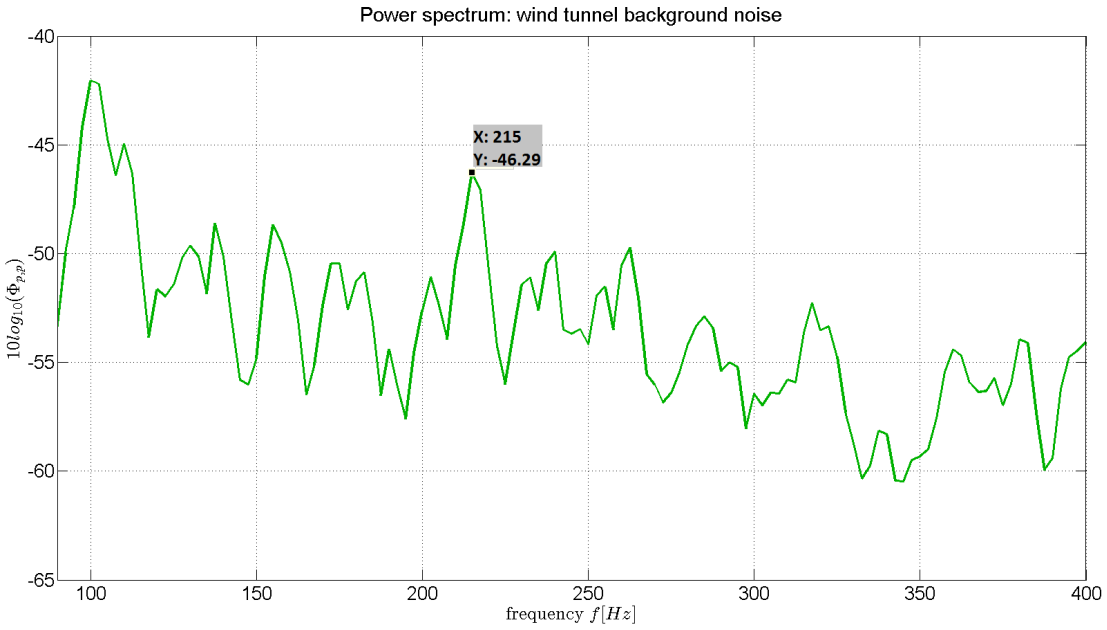

Figure B.4: Power spectra ($\Delta f = 2.4Hz$) of the background noise of V-tunnel with empty plexiglass-Kevlar test section and incoming flow at $20m/s$.

Despite the issues to be clarified in the mechanism of frequency shift in this appendix, a conclusion can still be reached that all-plexiglass test section, although

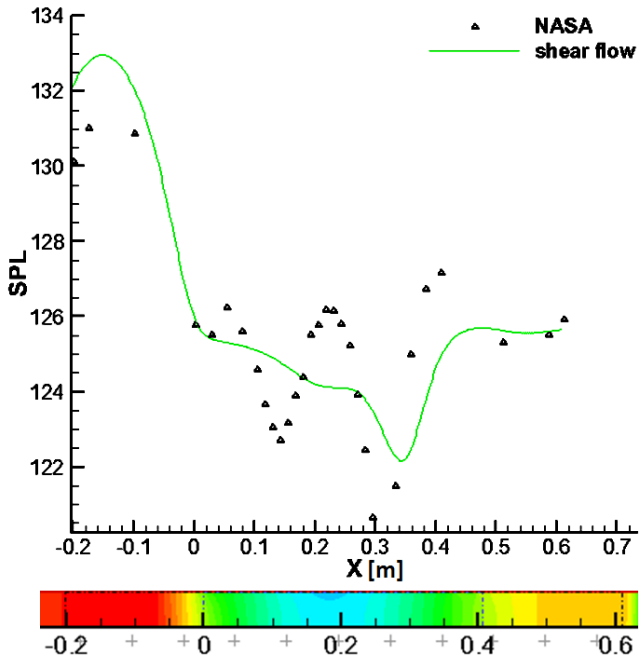

Figure B.5: An example of longitudinal acoustic pressure distribution. $[-0.203, 0] \cup [0.406, 0.609]$: solid wall; $[0, 0.406]$: acoustic liner. $SPL = 130dB$, $Ma = 0.335$,$f = 500Hz$, $Z = 0.33 - 0.98i$[34] [76]

favoured for PIV set-up, is not as preferable in the acoustic measurements or vortex shedding related measurements.

Figure B.5 offers an example of the longitudinal acoustic pressure distribution in a cylindrical tube with different wall conditions at different longitudinal locations. The sound pressure level applied at the inlet of the tube $x = -0.203m$ is $130dB$, with the flow speed at the center of the tube of $Ma = 0.335$. It can be observed that due to the presence of the acoustic liner in the region $[0, 0.406]m$, the sound pressure level exhibits a drop up to $10dB$ (black diamond in Figure B.5), corresponding to a reduction by 2/3 in sound pressure. While for the solid wall region $[-0.203, 0]m$ and $[0.406, 0.609]m$, the sound pressure level almost remains the same.

It can be inferred that the application of liner can be an effective way of avoiding resonance by attenuating the energy input of a certain transverse or longitudinal acoustic mode. It can also be inferred that the acoustic impedance of Kevlar is

larger than that of the plexiglass. Hence, the replacement of Kevlar, at least on one of the four sides of the test section, would be desirable for avoiding the effect of sound on vortex shedding.